CRYSTALLIZATION CONDITIONS FOR A BE- AND Y-RICH GRANITE--THE SHEEPROCK GRANITE OF WEST-CENTRAL UTAH

by

Eric H. Christiansen
Jack R. Rogers
Li Ming Wu

CONTRACT REPORT 91-6 APRIL 1991
UTAH GEOLOGICAL AND MINERAL SURVEY
a division of
UTAH DEPARTMENT OF NATURAL RESOURCES

THE PUBLICATION OF THIS PAPER
IS MADE POSSIBLE WITH MINERAL LEASE FUNDS

INTRODUCTION

The Sheeprock granite of west-central Utah is enriched and locally mineralized with beryllium and yttrium (Cohenour, 1959; Williams, 1954). Previous investigations of the whole-rock geochemistry of the pluton suggested that it crystallized in situ, from its walls inward, concentrating incompatible elements like Be and Y in the core of the pluton (Christiansen et al., 1988). Magmatic concentrations of Y show a five-fold increase from rim to core of the pluton (13 to 63 ppm). Funkhouser-Marolf (1985) identified monazite (REE phosphate), xenotime (Y phosphate), and Nb-Fe-W-Y-Ta oxides as important hosts for Y. A pegmatitic occurrence of samarskite (an Y-Nb-Ta-Ti oxide) has also been reported (Cohenour, 1959). High Be concentrations are found in the pluton as well; concentrations range from 2 to 50 ppm in apparently unmineralized samples (Christiansen et al., 1988). Large beryl rosettes (up to 50 cm in diameter, but usually much smaller) occur within the central part of this small pluton (Williams, 1954; Cohenour, 1959). Narrow greisen-bordered veins represent the most common type of post-magmatic mineralization in the granite. They host weak Sn-W mineralization.

Questions

These earlier investigations raised several important questions regarding the evolution and mineralization of the Sheeprock granite:

1. At what temperature and pressure did the beryl rosettes and greisens crystallize?
2. What were the concentrations or fugacities of the volatile species--H_2O, F, and Cl--in the magma and post-magmatic hydrothermal fluids?
3. Did the magma become water saturated during its final crystallization? Did this play a role

in the enrichment of Be or Y and the development of beryl rosettes or greisens?

4. Is greisenization an important process for enriching Be and Y?

In short, the roles of fluid saturation, crystallization of beryl rosettes, and greisen formation in the concentration of Be and Y were uncertain. In an effort to better understand these processes, we have examined late-magmatic and post-magmatic crystallization products by bulk rock analysis, electron microprobe studies of mineral grains, and fluid inclusion techniques. These studies have enabled us to estimate the crystallization conditions (T, P, and volatile fugacities) that prevailed during beryl mineralization and greisen formation in the Sheeprock granite and to construct geochemical models for their formation.

This report consists of two separate sections that describe our results. The first section describes the nature and origin of beryl mineralization and represents the work of Jack R. Rogers for an M.S. degree. The second section describes the nature and crystallization conditions for the quartz-muscovite greisens that cut the granite and is the M.S. thesis of Li Ming Wu.

SECTION 1

Origin of Beryl in the Miocene Sheeprock Granite, West-Central Utah

ABSTRACT

Beryl occurs as sub-spherical rosettes, as disseminated crystals, and in quartz veins, within a 21 Ma rare-element granite (enriched in Rb, Ta, Nb, Li, F, U, Th, and Be) in the Sheeprock Mountains of west-central Utah. Petrography, bulk rock chemistry, and mineral compositions indicate that there were at least two periods of beryl crystallization: a late-magmatic phase involving evolved residual melts of the granite magma and a post-magmatic phase involving metasomatic fluids.

Beryl rosettes are composed of beryl crystals radiating from a common center to form subspherical pods. Included in beryl are albite, zinnwaldite, ferrimuscovite, Nb-Ta-Fe-Mn-Ti oxides, quartz, and fluorite. Beryl contains low concentrations of Li and alkalies. Coexisting zinnwaldite and ferrimuscovite are F-rich and have average IV(F) of 0.39 (+/-0.08) and 0.33 (+/-0.06) respectively. Whole rock samples of the rosettes are enriched in Sc, Fe, Y, Cs, and REE relative to their granite hosts. Major and trace element patterns in the granite suggest that the granite evolved by crystallizing from the margins inward, producing pods of fluid-saturated residual melt. Fluid saturation may have caused fracturing of the pluton and a conseqeunt pressure quench of the magma. The rosettes crystallized from pegmatitic magma that formed during this rapid final stage of crystallization.

Granite containing disseminated beryl has a mineral assemblage similar to that of the rosettes except that K-feldspar is present. The composition of the disseminated beryl is

indistinguishable from that in the rosettes. Granite with disseminated beryl is also enriched in Sc, Y, and REE, but not to the levels found in the rosettes. Some disseminated beryl is seen as anhedral blebs within K-feldspar and plagioclase indicating that this type of beryl is a result of post-magmatic metasomatism as hydrothermal fluids reated with already solid granite. Likewise, beryl in narrow quartz veins and must have crystallized from hydrothermal fluids flowing through the fractured granite.

INTRODUCTION

Beryllium mineral occurrences of the eastern Great Basin, western USA, consist primarily of beryl, phenakite, and bertrandite. Cohenour (1963) described these occurrences as an "east-west trending beryllium belt" but the inclusion of beryllium localities in southern Utah forms a broader, diffuse distribution in the eastern Great Basin (Figure 1.1). Beryl is the most common mineral and is found in intrusive and extrusive igneous rocks of eastern Nevada and western Utah. In volcanic rocks, beryl occurs as vapor-phase condensates, and in granitic rocks it is an accessory mineral thought to be of magmatic or post-magmatic origin. Red beryl is found in topaz-bearing rhyolites in the Wah Wah Mountains (Shigley and Foord, 1985) and in the Thomas Range (Staatz, 1963). Granitic rocks that contain beryl occur in the Deep Creek Range (Bullock, 1964), near Gold Hill (Griffitts, 1965), at Granite Mountain (Fowkes, 1964) and in the Sheeprock Mountains (Williams 1954, Harris 1958, Cohenour 1959, and 1963). Beryl along with phenacite and bertrandite occurs in quartz veins in the Snake Range in eastern Nevada near Wheeler Peak (Whitebread and Lee, 1961; Lee and Erd, 1963). Bertrandite is found in economic concentrations in the rhyolite tuffs of the Spor Mountain Formation (Staatz, 1963; Lindsey, 1977), in the western part of the Thomas Range (Lindsey, 1977) and in sub-economic concentrations in similar but younger rocks at the Honeycomb Hills (Griffitts, 1965).

In the Basin and Range province, rhyolites and granites containing beryl are commonly topaz bearing and fluorine rich. The granite pluton of the Sheeprock Mountains, west-central Utah, is no exception to this generalization and contains beryl in sub-spherical aggregates, here called rosettes. Beryl rosettes are apparently rare, but Reid (1963) describes similar "balls" from the Sawtooth batholith of central Idaho. Beus (1966, p.79) describes "beryl stars" that also

appear to be similar to the rosettes described here. The beryl in these stars is said to be alkali-free and formed by hydrothermal processes. In addition to beryl rosettes, the Sheeprock granite contains beryl as disseminated crystals and in quartz veins that cut the granite.

In this paper, the petrography and geochemistry of three different types of beryl, their associated minerals, and host rocks are described as the basis for a model explaining the origin of beryl in the granite of the Sheeprock Mountains.

GEOLOGY AND SETTING OF THE SHEEPROCK GRANITE

The granite of the Sheeprock Mountains is anorogenic and Miocene in age, having a Rb-Sr isocron age of 20.9 Ma (Christiansen et al., 1988). The granite is slightly peraluminous and rich in rare elements and fluorine. The Sheeprock pluton intrudes folded and faulted Paleozoic sedimentary and Precambrian metasedimentary rocks (Figure 1.2). The intrusion is small and isolated from other igneous bodies but is part of an east-west belt of Tertiary igneous rocks.

The intrusion consists of biotite monzogranite to biotite-muscovite syenogranite (Christiansen et al., 1988). Accessory minerals include zircon, apatite, monazite, thorite, uraninite, fluorite, and rare topaz, which may be post-magmatic. Major and trace element compositions show that the granite is zoned; three different geochemical groups have been identified. Group 1 samples are representative of late crystallization, are enriched in Sc, incompatible rare elements (Be, Li, Rb, Cs, Nb, Ta, etc.), and fluorine. Group 2 samples represent early crystallization of a more "primitive" melt and are rich in compatible elements (Sr, Ca, REE) as compared to group 1. Group 3 samples are interpreted to be cumulates that formed along walls of a magma chamber and contain low concentrations of incompatible elements and

intermediate (between groups 1 and 2) concentrations of compatible elements. Christiansen et al. (1988) concluded that the Sheeprock granite evolved by fractional crystallization in situ. Strongly fractionated residual magma was concentrated in the center of the intrusion and corresponds to group 1 samples. Beryl of all types is found within the evolved core of the intrusion as defined by the outcrop area of group 1 samples.

Beryl in the Sheeprock Mountains was first reported by Williams (1954); he described beryl disseminated as small crystals in granite, aplite pods, and quartz veinlets, and in more massive form in rosettes and narrow veins. Harris (1958) and Cohenour (1959) also recognized pegmatitic pods containing beryl, feldspar, and quartz. Post-magmatic alteration consists of pervasive Fe staining of the outer part of the intrusion, local conversion of feldspars to clay minerals, and fractures bordered by muscovite-quartz greisens that are slightly mineralized with Sn and W.

ANALYTICAL METHODS

Samples and sample preparation

Samples of the three types of beryl studied were collected from the evolved central part of the Sheeprock granite (Figure 2). All were found in large boulders of float. Rosettes HBC-2R, HBC-3R, HBC-6R, and HBC-7R were separate nodules within a single boulder approximately 1 m across found on the east side of Hard-to-Beat Canyon. Granite with disseminated beryl was also found in the same locality as the boulder containing the rosettes. Only one sample, a small cluster of beryl crystals which macroscopically could not be distinguished as a rosette or as disseminated crystals, was found in Sheeprock Canyon (SRC1).

One other rosette and quartz veins containing beryl were found on the eastern side of Hard-to-Beat Canyon.

Samples were cut sequentially with a diamond saw normal and parallel to the *c* crystallographic axes of the beryl crystals composing the rosettes. Polished thin sections were made and studied using a standard petrographic microscope. Pieces of the rosettes were hand picked from the surrounding granitic host after crushing using a small high carbon steel mortar and pestle. Once separated, each sample was further broken down using the same mortar and pestle; 10-15 g of this material were pulverized using a small agate ball mill. Sample DHBC-1R, because it was a large granite sample, was pulverized in a tungsten carbide shatter box.

Whole-rock chemical analyses were performed by: wavelength dispersive x-ray fluorescence (XRF) spectrometry, instrumental neutron activation analysis (INAA), atomic absorption (AA) spectrometry, and inductively coupled plasma (ICP) spectrometry. Loss on ignition (LOI) was determined by heating 2 grams of rock powder in a ceramic crucible to 1000 °C for 4 hours in an electric furnace. Major oxides (SiO_2, TiO_2, Al_2O_3, Fe_2O_3, MnO, MgO, CaO, Na_2O, K_2O, and P_2O_5) and some trace elements (Sc, V, Cr, Ni, Cu, Zn, Ga, Rb, Sr, Y, Zr, Nb, Ba, La, and Nd) were analyzed by XRF. Samples were prepared by fusing powder mixed with lithium metaborate doped with lanthanum and molding them into glass discs for analysis of major elements (Norrish and Hutton, 1969). Trace elements and Na were analyzed by XRF using pressed powder pellets encased in cellulose. Accuracy and precision, as judged by repeated analysis of international geochemical reference materials for major elements except for Na are within +/- 1% (relative) at two standard deviations. For Na, Rb, Sr, Y, Zr, and Nb the precision is +/- 5%; for other trace elements +/- 10%.

Beryllium and lithium were analyzed by ICP. Solutions were initially prepared by hot perchloric-hydrofluoric acid digestion. However, a blue residue, presumably a beryllium fluoride precipitate, indicated that the beryllium was not totally dissolved. Thus, these samples were fused with a lithium metaborate flux and then digested in acid. Analytical precision of the ICP was +/- 2% (relative).

The samples were also analyzed by Bondar Clegg of Vancouver, BC, Canada, for beryllium (AA), lithium (AA), and fluorine (specific ion electrode). Analytical accuracy for these samples, based on analyses of USGS geochemical standards, is within +/- 1% and were comparable to results of the ICP analyses for Be and Li.

For selected samples, REE and other trace elements (Sc, Cs, Hf, Ta, Th, U, W,) were analyzed by INAA (Nuclear Activation Services Incorporated, Ann Arbor, Michigan). Analytical precision using INAA is on the order of +/- 10% (for Cs, Nd, Sm, Eu, Tb, and Lu) whereas Hf, Ta, Th, U, La, Ce, and Yb are within +/- 5% as judged by repeat analyses of reference materials.

Minerals were analyzed in polished thin sections with a four spectrometer Cameca SX-50 electron microprobe at the University of Utah. Micas (biotite and muscovite), feldspars, and beryl were analyzed by wavelength dispersive spectrometry. Natural mineral standards were used with an accelerating voltage of 15 KV and current, as measured on brass, of 30 nanoamps. The data were reduced on line using a PAP algorithm. Some minerals were identified by energy dispersive (EDS) analysis.

MINERALOGY AND PETROGRAPHY

Beryl rosettes

Beryl rosettes are composed of myriads of beryl crystals whose *c* axes radiate from a common center producing sub-spherical clots; in cross section they are like sun bursts (Figure 1.3). Rosettes range from approximately 3 to 50 cm in diameter. Individual crystals are light blue to clear or milky white giving the rosettes a cloudy light blue tint. Beryl crystals are long, slender, and prismatic, tapering from the outside margin to a point at the center of the rosette where the crystals originate (Figure 1.4a and 1.4b). Crystals are crowded, resulting in subhedral and irregular polygonal, instead of euhedral and hexagonal shapes. Beryl makes up about 63% of the rosettes examined (Table 1). Beryl is poikilitic, containing small laths of albite, anhedral quartz, fluorite, white mica (ferrimuscovite), dark mica (zinnwaldite), and complex Nb-Ta-Mn-Ti-Fe oxides (Figure 1.4c). Albite and quartz inclusions are small (< 1 mm). Fe-oxides, which are larger than the other inclusions, are elongate and tabular and appear to have grown along beryl grain boundaries. Fe-oxides are surrounded by narrow (< 1 mm) iron-stained rims consisting of reddish-brown hematite-limonite powder surrounding a remnant core of fresher material. Small vugs exist along beryl grain boundaries and in association with many of the mineral inclusions. K-feldspar, a major constituent of the granite, is absent within the rosettes.

Albite is abundant within the beryl rosettes. Point counting shows that albite makes up about 27% of the rosettes (Table 1). Albite grains are small and lath-shaped. Some show slight alteration to sericite along their margins and within their cores. A few albite grains in the rosettes have large mica flakes in their centers or around their corners indicating co-crystallization of albite and mica (Figure 1.4c).

Quartz crystals, which constitute about 3 to 7% of the rosettes, are anhedral and variable in size. They have large embayments suggesting that they were partially resorbed before or during crystallization of the beryl. Quartz abundance declines from the outer margins to the cores of the rosettes. Quartz grains near the margins are large and embayed; in thin section HBC-2A (Figure 1.4d and 4e), a "C" shaped quartz grain encompasses a "C" shaped albite and both are enclosed in beryl. Toward the center of the rosettes, quartz crystals are smaller, are less embayed, and are much less abundant (Figure 1.4f). Reaction rims are not associated with quartz or any of the other minerals. Quartz within the granite host surrounding the rosettes is subhedral, lacks embayments, and is variable in size.

Dark and white micas coexist within the beryl rosettes and are commonly intergrown with each other. As shown by electron microprobe analyses, the dark mica is zinnwaldite and the white mica is best described as ferrimuscovite. In plane polarized light, zinnwaldite is light brown and pleochroic and the ferrimuscovite is colorless or light pink and non-pleochroic. Both micas appear to have crystallized simultaneously and there are little or no alteration or reaction rims on the micas; they are well developed euhedral crystals. Muscovite is the more common species of mica, (about 2% muscovite and 1.0% zinnwaldite) within the beryl rosettes. Pleochroic spots within zinnwaldite, due to radiation damage, are a result of monazite, thorite, xenotime, zircon, uranothorite and other radioactive minerals and are typical of the mica in the granite host as well (Funkhouser-Marolf, 1984). Fluorite is relatively abundant at about 1.0% within the rosettes (Figure 1.4g). It appears to have crystallized in equilibrium with the other minerals. Fluorite occurs in the beryl crystals and in a few of the miarolitic cavities. Nb-Ta oxides within the rosettes are elongate and needle-shaped; other elements detected in the Nb-Ta

oxides by EDS include Fe, Mn, and Ti.

The rosettes are usually surrounded by a fine-grained granitic host of quartz, albite, biotite, and muscovite. Large phenocrysts of K-feldspar that are a major constituent of the granite are not found within the rosettes or the fine-grained material that surrounds them. Two sizes of quartz crystals are found in the granitic hosts: large crystals that are measured in millimeters, and smaller more abundant crystals on the order of microns. Except for the quartz phenocrysts the host granite around the rosettes is equigranular. Small fluid inclusions with tubular shapes are present but rare in beryl within the rosettes and appear to be primary. The inclusions contain CO^2. Planes of secondary fluid inclusions are also present.

Disseminated beryl

Small crystals of beryl (about 1 mm across) are locally disseminated (Figure 1.4h) in the core of the intrusion. These anhedral crystals are light blue as in the rosettes. Granite containing disseminated beryl has a hypidiomorphic texture and is usually coarser grained than the matrix surrounding the rosettes. The granite has phenocrysts of K-feldspar and quartz giving it a porphyritic texture. K-feldspar phenocrysts show Carlsbad twinning and are up to 3 cm long, some having perthitic texture (Figure 1.4i). Quartz crystals are not quite as large as the K-feldspar. Most beryl grains are anhedral and occur as blebs within K-feldspar. The texture suggests a reaction relationship between K-feldspar and beryl. Dark micas in these samples are more green than reddish brown; electron microprobe analyses show they are annitic biotites. They contain the same type of radiation damage from radioactive accessory minerals found by Funkhouser-Marlof (1985) and seen in zinnwaldites in the rosettes. Biotite grains are larger and

more abundant than zinnwaldite in the rosettes; however, the quantity of white mica is less than that in the rosettes or rosette hosts. Large crystals of albite are common. Fluorite was not identified within the samples studied, but it is a common accessory mineral in other group 1 samples (Christiansen et al., 1988). Fe-oxides are less abundant than in the rosettes.

Beryl in quartz veins

Narrow quartz veins that contain beryl (Figure 1.4j) cut the central part of the granite. The granite surrounding the vein studied is fine-grained, containing albite, quartz, K-feldspar, dark mica (intermediate between annite and zinnwaldite), small flakes of white mica (probably muscovite), and accessory minerals such as zircon, monazite, and oxides rich in Nb, Ta, Fe, Mn, and Ti. Beryl appears in the center of the 1 cm wide vein flanked on both sides by quartz (Figure 1.4k). Apparently, quartz crystallized first on the wall of an open fracture followed by beryl. Beryl grains are anhedral and are approximately 3 mm across. Quartz crystals within the vein are large compared to those within the host matrix.

Secondary or pseudo-secondary fluid inclusions (type 1, liquid with small vapor bubbles) within quartz are abundant; they are small and lie in planes created by fracturing during or after quartz growth. Isolated, apparently primary fluid inclusions were also observed but in quartz are considerably less abundant than the secondary inclusions. They are randomly oriented and larger than the secondary inclusions. Three types of primary fluid inclusions were noted: type 1; type 2 (liquid with large vapor bubble); and type 3 (liquid with small vapor bubble and daughter minerals probably halite). Minerals along the edges of the vein are not broken or highly fractured; albite along the margins exhibits slight phyllic alteration.

GEOCHEMISTRY

Mineral chemistry

Micas. Dark micas, analyzed from beryl rosettes, (Table 2) are best classified as zinnwaldites; those found in granite containing disseminated beryl or vein beryl form a trend away from zinnwaldite toward annite. Biotite compositions from the group 1 granite cluster closer to annite (Figure 1.5). White micas in the rosettes and in granite with disseminated beryl are strongly enriched in Fe and are best classified as ferrimuscovites (Bailey, 1984) (Figure 1.6) but ignorance of Li and Fe^{+3}/Fe^{+2} make their nomenclature problematic. Geochemically, zinnwaldites can be distinguished from ferrimuscovites (Figure 1.7) on the basis of octahedral Al (much less than 2 for zinnwaldite). There is on the average 0.5 wt% MgO in the zinnwaldites associated with beryl. Biotites, from the Sheeprock pluton lacking beryl, analyzed by E. H. Christiansen (unpublished data), are more enriched in MgO and have lower Fe/(Fe+Mg) ratios (Figure 1.7). Titanium concentrations are lower in the rosette zinnwaldite than biotites in the Sheeprock granite (Figure 1.8) with maximum concentrations no greater than 1.5 wt% TiO^2. However, the amount of titanium analyzed in the muscovites is very low, less than 0.5 wt%. For all micas, analyzed CaO concentrations were at or below detection limits. Rb, although not analyzed in all grains, is estimated to be about 0.56 wt% (zinnwaldite) and 0.43 wt% (ferrimuscovite) from analyses of 3 micas.

Fluorine and Cl analyses of zinnwaldite and ferrimuscovite are of great interest (Figure 1.9). Analyzed zinnwaldite is high in F with concentrations between 3.2 and 4.4 wt% for grains from all three types of beryl occurrences, but is highest in rosettes. Fluorine concentrations are also high in ferrimuscovites compared to the biotites of the granite; but less than that in co-

existing zinnwaldites. In spite of high F concentrations, Fe concentrations are also high. Because of Fe-F avoidance in micas, the enrichment in F is better measured by the F intercept values [(IV)F] of Munoz (1984). Calculated IV(F) are very low (for both ferrimuscovite and zinnwaldite) indicating that fluorine enrichments were high when the rosette micas crystallized (Figure 1.10). There is a possibility that Li in the structure may cause erroneously low (IV)F; however, both white and dark micas have similar (IV)F (Figure 1.11).

Chlorine concentrations are low in both micas with values never exceeding 0.05 weight percent. Chlorine is slightly enriched in the zinnwaldites compared to the ferrimuscovites (Table 2). Also, Cl concentrations are higher and IV(Cl) lower in the dark micas surrounding vein beryl than in rosettes.

As noted earlier, both micas appear to have crystallized simultaneously in the rosettes. This is evidenced by mutual intergrowths of zinnwaldite and ferrimuscovite. Moreover, both micas have the same IV(F); the range of the IV(F) values is also rather narrow in Figure 1.11.

The IV(F) of the micas from the Sheeprock rosettes are as low as those from Henderson (Mo porphyry deposit) whereas biotites from the Santa Rita porphyry Cu deposit and unaltered biotites from Bishop tuff, Sierran granites, Pikes Peak, and Peruvian rhyolites plot to the right in Figure 1.11 indicating lower levels of F-enrichment (Munoz, 1984).

Fluorine intercepts calculated for ferrimuscovite and zinnwaldite from the rosettes indicate that the micas approached equilibrium. Ferrimuscovite in one of the samples with disseminated beryl (DHBC3) has a significantly lower (IV)F than that of coexisting zinnwaldite. This is consistent with a secondary non-magmatic origin for this muscovite and the absence of complete mineralogical equilibrium in the samples with disseminated beryl.

Mica compositions from granites containing disseminated beryl (S and D on the diagrams) are systematically different from those in rosettes. Mg and Fe concentrations are higher in the greener biotites in the samples containing disseminated beryl. Fluorine and Cl contents and intercept values of these dark micas are intermediate between most group 1 granites and those in the rosettes. Moreover, titanium is significantly lower in sample SC-2, which contains disseminated beryl, than in zinnwaldite from beryl rosettes.

Mica was not found in the beryl-quartz vein, therefore, only dark micas in the surrounding granite were analyzed (Table 2). They are similar in many ways to those of the rosettes; however, they have higher Cl and Ti (Figures 8 and 9) and lower F (Figure 1.10), implying that they crystallized from a hotter less evolved magma and that they may not be contemporaneous with the beryl crystallization.

Feldspars. Feldspars from samples containing all three types of beryl occurrences were analyzed (Table 3; Figure 1.12). Based on declining An content in plagioclase, samples of granite containing disseminated beryl are the least evolved, those from the granitic host of the vein type are intermediate, and those from the rosettes are the most evolved (see Figure 1.12). Small laths of albite from the beryl rosettes have an average composition of Ab_{98} An_1 Or_1. Large plagioclase crystals within the rosettes, very sparse compared to the smaller albite laths, are not zoned and are compositionally identical to the small albite laths. Plagioclase, from samples of granite containing disseminated beryl, is only slightly more calcic and has an average composition of $Ab_{97.0}$ $An_{1.8}$ $Or_{1.2}$. A large crystal of plagioclase, within a sample containing disseminated beryl, is slightly zoned and contains the highest concentrations of Ca ($Ab_{92.1}$ $An_{5.9}$ $Or_{2.0}$). From rim to core, a small increase of calcium (0.4 wt%) is observed. Plagioclase

analyzed from the granite host of the quartz veined beryl has the same composition as the plagioclase containing disseminated beryl.

K-feldspar was not found in the beryl rosettes. K-feldspars in samples with disseminated beryl and vein beryl (DHBC-3 and HBC-1V) are similar with an average composition of $Or_{93.6}$ $Ab_{6.4}$. Their perthitic character and high Or content suggests that they continued to equilibrate during subsolidus cooling of the pluton (Elkins and Grove, 1990).

Beryl. Beryl was analyzed by electron microprobe for Si, Al, Cs, Rb, Fe, Mn, K, and Na (Table 4). Analyses of these elements produced totals of 85 wt% (+/- 2.0 wt%). The amount of BeO estimated from stoichiometry should be about 13 wt%, a value consistent with the average modal abundance of beryl (63%) and the measured BeO concentration (average 8.3%) in the rosettes. Li analyzed by atomic absorption and ICP, in whole rock samples of beryl rosettes, disseminated beryl, mica separates, and surrounding granitic matrices, implies that the beryl contains at most, only small concentrations of Li_2O. Li concentration in bulk rosette samples only reached several hundred parts per million (Table 5) and much of that must be in the mica. According to Aurisicchio et. al. (1988) the alkali ions that reside in the structural channels ($R^+ = Cs^+ + Rb^+ + K^+ + Na^+$) equals the sum of divalent cations, plus tetrahedral aluminum minus titanium, minus silicon and aluminum associated with the tetrahedral site of beryllium, plus any lithium that may be present

$$R^+ = R^{++} + Al^{iv}\text{-}Ti\text{-}(Al^T + Si^T) + Li.$$

According to their study, lithium substitutes for Be in the tetrahedral site. This creates a charge deficiency which can be corrected either by other substitutions for framework ions or by incorporating alkali ions in the channels of the mineral. Li in beryl can then be estimated by

graphical means (Figure 1.13). The Li-free analyses do not deviate from the trend established by Aurisicchio et al. (1985) suggesting that the Li content of the beryl is very low (Figure 1.13). Moreover, these beryls are not rich in alkali elements. R_f^+, the total of all the alkali channel constituents, does not exceed 0.5 wt%. Thus, according to the classification of Beus (1966) that is based on the concentration of R_f^+, beryl of the Sheeprock intrusion is considered alkali free.

The amount of iron that substitutes for aluminum in beryl from the Sheeprock Mountains is small with FeO concentrations of 0.5 to 1.2 wt%. As suggested by Aurisicchio et al. (1988), color is probably controlled by differences in the amount of Fe, colorless beryl containing less Fe whereas blue aquamarine beryl has more Fe. Other Me^{2+} that were analyzed (Mg and Mn) have concentrations near detection limits (approximately 0.01 wt%).

Beryl disseminated in granite is nearly identical to that in rosettes. The compositions of the vein-type beryl overlap with those of rosette beryl but extend almost to the ideal formula of beryl $Be_3Al_2(SiO_3)_6$. They show very little alkali or Me^{2+} substitution.

WHOLE ROCK GEOCHEMISTRY

The average major element composition of six rosettes has 69.0 (+/- 1.3) wt% SiO_2 (Table 5). The amount of silica and other oxides varies according to the proportions of albite, quartz, mica, and beryl. Compared to the most evolved beryl-free granite (average group 1 composition) of the Sheeprock granite, the rosettes are deficient in Si, Mn, Na, K, and P, and are enriched in Ti, Al, and Fe (Figure 1.14a). From electron microprobe analyses, beryl and mica contribute less than about 0.2 wt% Na^2O to the whole rock analyses; therefore, albite is the only significant sodium-bearing mineral within the rosettes. Thus, the percent of albite

within the rosette can be approximated from the amount of Na_2O in the whole rock analyses. This results in about 28.0 percent albite, which is similar to the results obtained from point counting (26%). Reflecting the absence of potassium feldspars and paucity of micas, K_2O is present in concentrations of only about 0.5% corresponding to mica concentrations of about 4%. These elemental analyses show that rosettes do not simply represent crystallization of a residual melt from group 1 granite. Sc for example is very enriched in the rosettes (about 150 ppm), and Rb is low (about 175 ppm) compared to the 2.5 ppm of Sc and 900 ppm Rb in average group 1 granite (Christiansen et al., 1988). Sc enrichment seen in the rosettes is due to beryl's affinity for it (Beus, 1966). Sc substitutes for Fe^{3+} in the octahedral site. All of the samples that contain beryl show elevated Sc. Other trace elements enriched in the rosettes compared to highly evolved core are Y, Cs, and the LREE's. The latter enrichment may be caused by monazite inclusions. Thorium and U are depleted in the rosettes compared to group 1 samples (Figure 1.14a).

Granitic rock immediately surrounding the rosettes is enriched in Ti, Fe, Na, and Be and depleted in Al, Mg, Ca, and K compared to the average granite from the core of the intrusion (Figure 1.14b). Potassium concentrations within the host granite, are low because of the low abundance of K-feldspar. Sodium concentrations are elevated compared to the rosettes. Moreover, Na_2O/K_2O ratios are greater than 1; the granite analyses of Christiansen et al. (1988) show Na_2O/K_2O less than one. In the granite host, SiO_2, MnO, and P_2O_5 concentrations are comparable to those of group 1 granite. Trace element concentrations in the host surrounding the rosettes are different from those of the group 1 granite or the rosettes as well. Nb and Ta, generally incompatible elements (Figure 1.14b and 14c), are enriched in the granitic hosts. U

and Th are also depleted compared to the average granite from the evolved core of the intrusion. These trends are continuations of magmatic trends.

Compositions of granites with disseminated beryl are much the same as those of the granites that host the beryl rosettes (Table 2). Ti, Fe, Mn, Mg, Ca, Na, P, Zr, and Be are enriched compared to the evolved group 1 granite while Al and K are depleted. Be and Sc concentrations suggest that there is about 3-4% beryl in these rocks.

The REE patterns of the rosettes, granitic hosts, and granite with disseminated beryl (Figure 1.15) show negative Eu anomalies with those of the granitic host having the deepest Eu anomalies. The maximum LREE contents are in the rosettes, whereas the minimum contents are in the granitic hosts of rosettes. Rosette (upper pattern) samples are also enriched in Eu, Tb, Yb, and Lu as compared to the granitic host surrounding the rosettes and granite containing disseminated beryl. Samples with disseminated beryl (lower pattern) have intermediate REE patterns, forming a band between the rosettes and host granite samples.

DISCUSSION

Beryl in the granite of the Sheeprock Mountains may be late magmatic (crystallized from melt and/or coexisting fluids) or post magmatic (due to metasomatic processes). Petrography, mineralogy, and geochemistry of the various types of beryl are used below to interpret their origins. Phase relations in F-and Be-rich rocks are also used to constrain the mode of beryl crystallization.

Beryl Rosettes

Petrography. Petrographically the rosettes appear to be of magmatic origin. The large crystals in the rosettes appear to have grown freely from a fluid or melt. The poikilitic textures of the beryl imply that either beryl crystallized last enclosing these other minerals or that beryl crystallized simultaneously but grew faster engulfing the small grains. This is evidenced by small tabular euhedral albite grains found within the rosettes. Textural relationships between the minerals in the rosettes indicate that there may have been mineral interactions with coexisting melt. Quartz crystals described above typically are anhedral and have large embayments; the abundance of quartz diminishes from the outer margin to the central core of the rosettes. These observations suggest that quartz was not stable during formation of the rosettes and was being resorbed by the melt. Albite appears to have been stable during beryl crystallization but crystal sizes are small compared with albite grains in the granite. The beryl, albite, or micas do not exhibit zoning or distinctive reaction rims which would suggest metasomatic reactions between a fluid and pre-existing solid. This is also true of albite and mica found in the surrounding granite.

Lofgren (1974), who experimentally studied the crystal morphology of plagioclase in relation to different cooling conditions, determined that plagioclase with a composition between An_0 and An_5 and with a ΔT of about 44 °C crystallized with a tabular morphology. Under a much larger ΔT of 140 °C and with the same compositions the morphology was that of spherical nodules of acicular crystals. In a study of nucleation and growth of alkali feldspars from hydrous silicate melts Fenn (1977) demonstrated that alkali feldspars under similar partial quench conditions as plagioclase crystallize with similar spherical and tabular morphologies. He used

a composition of Or_{10} with 2.7 percent H_2O and a ΔT of 205°C; crystallization products were spherical nodules of acicular crystals. The spherical morphology of the rosettes, with acicular beryl crystals and tabular albite grains, can be interpreted as resulting from rapid crystallization from a melt due to a large degree of undercooling (ΔT).

If the tabular morphology and abundant nucleation sites of the albite in and around the rosettes can be compared to the albite crystallized by Lofgren (1974), then it can be concluded that there could have been several 10's of degrees of undercooling of the melt with respect to Ab during the final stages of crystallization of the Sheeprock granite. Beryl could have grown simultaneously under conditions of greater undercooling as evidenced by spherulitic morphologies (assuming spherulitic growth is indicative of rapid growth). Rapid beryl growth may have been aided by the rapid diffusion of Be because of its small ionic radius. Hence, beryl could perhaps grow more rapidly than albite and engulf it. Under these conditions it is plausible that the rosettes could have formed by crystallization from an undercooled melt.

However, it is difficult to envision a sharp drop of temperature (large ΔT) in a plutonic setting, perhaps eliminating thermal undercooling as a mechanism for rosette growth. On the other hand, if the pluton became fluid-saturated and then suddenly fractured, undercooling could result from a pressure drop and fluid loss. Fluid saturation is indicated by miarolitic cavities and the experiments of Webster et al. (1987) with a similar melt composition and phase assemblage. Thus, quench growth of beryl and plagioclase could be an important mechanism in the formation of the rosettes.

A sharp drop in pressure may also help explain the resorbed quartz and absence of K-feldspar in and near rosettes. Figure 1.16 is a generalized phase diagram for the granitic system

SiO_2-$NaAlSi_3O_8$-$KAlSi_3O_8$-$CaAl_2Si_2O_8$-H_2O. Cotectics are shown for arbitrary high and low pressures. At high pressure the albite stability field is small and a relatively sodic water-saturated melt is in equilibrium with quartz, albite, and K-feldspar at the eutectic. If the pluton fractured, causing the pressure to suddenly fall, the albite stability field enlarges at the expense of quartz and K-feldspar. The melt would then crystallize only albite; beryl would co-crystallize if the melt were appropriately enriched in Be. Quartz and K-feldspar would become resorbed; apparently quartz dissolved more slowly than did K-feldspar (e.g. Weidner and Martin, 1987).

Geochemistry. By comparing the mica compositions of the rosettes with those of the granite, a distinct evolutionary pattern relating the granite to the rosettes is evident. Figure 1.7 shows the compositional range for micas from samples with different types of beryl and from beryl-free granite. Biotites rich in Mg but depleted in Al formed during the first stages of crystallization of the granite (groups 2 and 3; Christiansen et al. 1988). As the granitic magma evolved by crystal fractionation, biotites became enriched in Fe, Li, Al, and F. In this slightly peraluminous intrusion, the activity of Al became progressively higher until near the final consolidation of the granite, two coexisting micas crystallized, zinnwaldite and ferrimuscovite. These trends are consistent with magmatic crystallization.

Titanium-iron contents of the micas show the same evolutionary relationship between granite and rosettes (Figure 1.8). Biotites containing the most Ti and Fe and highest Ti/Fe ratios are found within the less evolved granite. Zinnwaldite R within the rosettes show the lowest amounts of Ti and Fe indicative of low crystallization temperature (e.g. Speer, 1984; Luhr et al., 1984). An evolutionary trend relating rosette micas to igneous micas is also evident from the F and Cl intercept values (Figure 1.9). Biotites formed during early crystallization of the

granite are chlorine rich, relative to micas analyzed from the rosettes and group 1 granite, but have normal amounts of Cl as compared to other mica analyses (e.g., Munoz, 1984; Speer, 1984). Chlorine intercepts for the granite cluster around -3.5 as compared to chlorine intercepts of zinnwaldites from the beryl rosettes which cluster around -3.1. This increase, the result of declining HCl fugacities, may be consistent with the fluid saturation model described above. Chlorine partitions preferentially into hydrous fluids coexisting with magmas (Burnham, 1979) and HCl fugacity in the magma could drop if these fluids escaped. Fluorine intercepts of the micas decrease with evolution of the granite, monitored by increasing Fe/(Fe+Mg) ratios and incompatible element concentrations, from IV(F)=1.16 (biotites with a Fe/(Fe+Mg) ratio of approximately 0.55) to IV(F)=0.75 which correspond to Fe-rich biotites (Fe/(Fe+Mg) ratios between 0.8 and 0.9). The Fe/(Fe+Mg) ratios of zinnwaldites associated with the beryl are even higher ranging up to 0.97 (zinnwaldites from beryl rosettes). Zinnwaldites within the beryl rosettes have IV(F)=0.39 (average of 22 samples with a S.D. of +/-0.08; Figure 1.11), while the ferrimuscovites have fluorine intercept values of 0.33 (average of 25 samples with a S.D. of +/-0.06). These low values, indicative of high HF fugacities, are lower than those typical of F-rich magmatic and hydrothermal biotites related to porphyry Mo and Sn-W-Be deposits compiled by Munoz (1984) (Fig. 11). Progressively lower F intercept values for the Fe-rich biotites from the granite, biotite from the granite with disseminated beryl, and the two micas (zinnwaldite, and ferrimuscovite) from the beryl rosettes, show that the granite became increasingly F-enriched as it crystallized. This, too, is consistent with magmatic evolution through crystal fractionation processes relating granites to rosettes. If comparisons with hydrothermal and igneous micas in porphyry Mo deposits are meaningful, micas that have

crystallized as a result of metasomatism should be richer in Mg and Cl than unaltered igneous biotites (Munoz 1984). Munoz (1984) states that lithium may have a strong effect on the partitioning of F in biotite. Analysis of a hand-picked mica (intergrown zinnwaldite and ferrimuscovite micas) sample shows that Li concentration (0.8% Li_2O) too low to be solely responsible for the large amount of fluorine present in the micas. A correction factor (Munoz, (1984) can be applied which would indicate that the IV(F) calculated here for the zinnwaldites may be 0.4 units too low. Using the calculated fluorine and chlorine intercept values, values of fH_2O/HF and fH_2O/HCl can be calculated (Munoz 1984) if the temperature is known. Temperatures were estimated (average 580°C, S.D. +/-4.5) using the Ti and Fe concentrations in the dark micas in the rosettes and the empirical thermometer of I.S.E. Carmichael presented in Luhr et al., 1984). This temperature is reasonable in light of the low crystallization temperatures (approximately 600 to 700°C) estimated for other F-rich igneous systems from western Utah (Christiansen et al., 1984; Turley and Nash, 1980; Congdon and Nash, 1988). Moreover, experimental work with the chemically similar Spor Mountain rhyolite reveals that its solidus under water-saturated conditions is only about 500°C (Webster et al., 1987). Using the 580°C temperatures, fugacity ratios calculated from rosette analyses are log fH_2O/fHF 2.8 (+/-0.073) and $fH_2O/fHCl$ 3.0 (+/-0.071). These low ratios are consistent with the fluorine rich character of the Sheeprock granite.

Like micas, feldspar analyses show similar evolutionary trends relating the granite to the beryl rosettes. Plagioclase compositions are more calcic in the less evolved granite but become more sodic reaching almost pure albite in granite with beryl and in the (Figure 12) rosettes.

Trace element compositions of the rosettes, their hosts, and samples with disseminated

beryl also show distinct trends that may be related by magmatic evolution. Using elements which are not sensitive to the apparent absence of K-feldspar and presence of beryl, it is apparent that the magma from which the rosettes crystallized was related to the granite, but even more highly evolved. For example Rb plotted against Nb (Figure 17) shows the host for the rosettes enriched in both elements. Granitic host samples, in the majority of the samples analyzed, cluster around the most evolved group 1 granite samples. However, Rb is lower in some host granite samples, probably because of low concentrations of K-feldspar in these samples. Nb and Ta variation defines a similar but less scattered trend caused by the enrichments of both of these elements during evolution of the Sheeprock granite (Figure 1.18). Hosts for the rosettes are more enriched in Nb and Ta than are the group 1 granites. Samples with disseminated beryl are similar to group 1 samples. The continuity in incompatible element trends is consistent with the mineralogical evidence that the rosettes represent the end stages of magmatic crystallization.

Crystallization conditions. Burt (1978) proposed phase relationships for Be-minerals based on natural occurrences. These were refined later to include F-bearing phases including topaz, fluorite, and mica (Burt, 1981). Barton (1986) conducted new experiments and refined the results of Burt and others in the system $BeO\text{-}SiO_2\text{-}Al_2O_3\text{-}H_2O$, to calculate phase diagrams for minerals in terms of P, T, and the activities of Al_2O_3 and SiO_2. These studies show that under low alkalinity and water-saturated conditions beryl has a wide thermal stability range. Pure beryl (and aluminum silicate or muscovite) is replaced by chrysoberyl and quartz at a temperature of greater than about 700°C with little pressure dependence. At low P (⟨1 Kb), euclase replaces beryl below 300 to 400°C (depending on $aSiO_2$). Taking the temperature of formation as estimated from Fe and Ti concentrations in biotites of the rosettes, the activity of

silica (as log mH_4SiO_4) constrained by the presence of quartz is limited to be about -1.3; resorbed quartz in the rosettes suggests a value somewhat less than this. The aAl_2O_3 was above the K-feldspar-muscovite reaction boundary but below corundum stability (about -0.2 log units). The activity of HF was high as indicated by mica compositions and the presence of fluorite, but not high enough to stabilize the assemblage phenacite-topaz which forms by the breakdown of beryl in aluminous rocks (Burt, 1975). These broad constraints are consistent with magmatic crystallization of beryl rosettes at a temperature of about 600°C as suggested above.

Summary Model. Formation of the beryl rosettes occurred during the last stages of crystallization of the Sheeprock intrusion. The granite magma crystallized by a fractionation process which increased Be, F, and H_2O concentrations in the melt (Christiansen et al., 1988). Eventually the magma became fluid saturated. Fracturing, perhaps as a result of fluid saturation and consequent increase in internal P, may have lowered the pressure causing the residual magmas to fractionate further. Pockets of residual beryllium-rich melts formed, scattered throughout the core of the granite (Figure 1.19). As a consequence of high Be and lower pressure, beryl became stable and quartz and K-feldspar became unstable. Masses of albite, two-mica granite and spherical rosettes of beryl crystallized rapidly.

Although beryl commonly forms by metasomatic processes we do not think the Sheeprock rosettes formed in this way. Beus (1966) believed that pneumatolytic or hydrothermal alteration was responsible for the formation of radiating growths of beryl crystals. Although pneumatolytic conditions in the granite were possible, the textural evidence strongly suggests that beryl is of magmatic origin. Haapala (1988) concluded that beryl in the Eurajoki stock of Finland, which is geochemically and mineralogically very similar to the granitic pluton of the Sheeprock

Mountains, crystallized as a result of albitization as indicated by exsolution and replacement textures. Feldspars within the Sheeprock rosettes do not have these types of textures but have sharp, clean grain boundaries without perthitic bleb, or graphic intergrowths.

Disseminated Beryl

Petrographic Evidence. Disseminated beryl is found intergrown with plagioclase and K-feldspar producing a micrographic texture. This texture suggests that much of this beryl is secondary, replacing the feldspars due to a metasomatic introduction of Be.

Geochemistry. Micas from granite containing disseminated beryl are different in composition from those of the rosettes. Micas from sample DHBC3 (D in Figures 7 and 8) are zinnwaldite except for two white mica analyses (d) which have low Fe/(Fe+Mg) and high Al and plot to the right of the trend for other micas; these micas also have low Ti/Fe ratios suggesting that they crystallized at low temperature and are secondary in origin. These ferrimuscovites also have low interlayer site occupancy and are similar in this regard to a clearly secondary muscovite (Table 2 sample HBC3M x) formed during alteration of feldspar in sample DHBC3. Coupled with their lower Ti and higher Mg contents these trends are consistent with those found by Monier et al. (1984) for post-magmatic muscovite and contrast with what are magmatic ferrimuscovites in the rosettes. Zinnwaldites from sample SRC1, of granite containing disseminated beryl, lie in the same area of Figure 1.7 as those analyzed from the rosettes; however, as a group they are depleted in Ti and F and enriched in Cl relative to those found in rosettes (Figure 1.8).

Zinnwaldites from the granite containing disseminated beryl have Fe/Ti temperatures of

about 560°C (+/- 17°) s and 610°C (+/- 6°) D. These temperatures are slightly lower and higher,respectively, than those calculated for the beryl rosettes. Fluorine and Cl intercept values for the zinnwaldites coexisting with disseminated beryl are respectively: 0.56 (+/- 0.06) and -3.14 (+/- 0.10) for the s-type zinnwaldites, and 1.02 (+/- 0.07) and -3.89 (+/-0.071) for the d type zinnwaldites (Figure 1.9). The s type zinnwaldites crystallized under conditions similar to the rosettes but at higher fHF/fH_2O, as shown by the smaller IV(F) values, than those of the d-types.

Phase relations. Quartz was apparently stable in the granite containing disseminated beryl. Using Barton's (1986) phase diagram and a temperature of 600°C log mH_4SiO_4 can be constrained using the quartz stability curve to -1.3 (at a pressure of 1 kb). However, petrography shows K-feldspar was unstable or being consumed at the time of beryl crystallization while ferrimuscovite was stable. From this information it can be inferred that the activity of Al_2O_3 increased but was not as high as it appears to have been in the rosettes. Barton's (1986) log activity aluminum-temperature diagram limits the log aAl_2O_3 to be below -0.2 (for a temperature of 600°C and a pressure of 1 kb). According to Barton (1982) the log fHF/fH_2O, calculated from the zinnwaldite in the granite, at the assumed temperature is to low for K-feldspar to be stable, instead muscovite is stable.

Summary model. A reaction between beryllium and K-feldspar after the granite crystallized is indicated by petrography of sample DHBC3, granitic host containing disseminated beryl. since the granite is enriched in fluorine, this can be represented by the equation:

$$2KAlSi_3O_8 + 3BeO + F_2O_{-1} = Be_3Al_2(SiO_3)_6 + 2KF \quad (1)$$

where F_2O_{-1} is an exchange operator (e.g., Burt 1981). Fluorine may be an important

constituent in the mobilization of beryllium, silica, and aluminum. Barton (1982) concluded that fluorination reactions for calcium-bearing feldspars produce fluorite plus an aluminous phase +/- quartz by the following reaction:

$CaAl_2Si_2O_8 + KAlSi_3O_8 + 2HF =$

$KAl_2[AlSi_3O_{10}](OH)_2 + CaF_2 + 2SiO_2.$ (2)

If equations (1) and (2) are added, the result is:

$3KAlSi_3O_8 + CaAl_2Si_2O_8 + 3BeO + 2HF + F_2O_{-1} = Be_3Al_2(SiO_3)_6 +$

$KAl_2(AlSi_3O_{10})(OH)_2 + CaF_2 + 2SiO_2 + 2KF$ (3)

This reaction closely reproduces the phase assemblage seen in the Sheeprock granite and could liberate K to a fluid where it would then be available for greisenization. It thus, appears that some of the beryl disseminated throughout the granite is post magmatic and is a result of metasomatic processes.

Beryl in quartz veins

Petrography. The paragenetic sequence in the veins is quartz then beryl; beryl is in the center of the vein. Quartz and beryl are the only minerals present within the vein; K-feldspar, zinnwaldite, albite, and quartz were identified within the granitic host. Zircon, monazite, and Nb-Ta-Fe-Mn-Ti oxides were identified in zinnwaldites of the granite wall rock.

Geochemistry. Petrographic evidence shows the vein is clearly post magmatic. Zinnwaldite was the only mica found within the granite containing the quartz-beryl vein, except for a few scattered sericite patches along the margins of feldspars. On Figures 6 and 7 the of zinnwaldites in the host of the vein form a group between those of the rosettes and of the granite

containing disseminated beryl. The Fe-Ti ratios indicate that equilibration temperature of this rock was 600°C (+/- 9°C) as compared to 610-560°C for the disseminated beryl listed above. IV(F) values (0.486 +/- 0.054) for the vein type zinnwaldite show F was more enriched than in the disseminated samples but less enriched than in the rosettes. IV(Cl) values from the zinnwaldite of -3.29 (+/- 0.1) are also intermediate between those more enriched in Cl in rosettes and those from the granite with disseminated beryl.

Summary model. The origin or the beryl in the quartz veins is straightforward. The quartz vein with beryl is secondary and crystallized from fluids circulating through fractures within the pluton shortly after solidification. A nonmagmatic origin is consistent with the compositional differences seen between rosette micas and those around the veins.

CONCLUSIONS

The Sheeprock granite is a high fluorine, rare-element rich, Miocene pluton that crystallized from the margins to the center. In situ crystallization caused the residual liquid to evolve geochemically; the most evolved Be-rich magma occupied the center of the pluton. Three different types of beryl crystallized in the highly evolved granite: rosettes of elongated prismatic beryl that form sub-spherical nodules, disseminated beryl found as accessory minerals, and beryl in quartz veins. The beryl rosettes appear to be a result of protracted fractional crystallization that formed a Be-rich residual melt that became fluid-saturated. Apparently, fracturing of the magma chamber caused a drop in pressure causing rapid undercooling and further enrichment of Be and incompatible elements in residual liquids. Eventually, scattered beryl nuclei formed and grew rapidly. A magmatic rather than metasomatic origin for the beryl rosettes is indicated

by the lack of replacement textures, low IV(F) and high IV(Cl) in micas, and trace element and mineral composition trends that are continuations of those seen in the granite. Disseminated beryl found within some samples of granite formed by metasomatic processes after the granite crystallized. Vein beryl crystallized from hydrothermal fluids in fractures. The veins and the fluids that flowed through them may be a result of the fluid saturation and fracturing of the pluton. Micas affected by metasomatism are enriched in Cl and Mg than those in the rosettes.

SECTION 2

Greisenization of the Sheeprock Granite, west-Central Utah: A fluid Inclusion and Geochemical Study

ABSTRACT

Weakly mineralized greisen occurs as envelopes around vertical fractures in the Sheeprock granite of west-central Utah. Greisen consists of intergrowths of quartz, Fe- and F-rich muscovite, fluorite, hematite, magnetite, and rare topaz. Proportions of quartz, iron oxides, and muscovite control major and most trace element concentrations. K_2O in the greisens correlates strongly with Al_2O3, MnO, Rb, Cs, and Ga, all elements accommodated in muscovite. The correlation of Sn with this group of elements suggests that a significant proportion of Sn is in muscovite. Concentrations of Si, K, Hf, and LREE in greisen show relatively little change (+/- 10%) from parental granite. Fe, Mn, and all alkali elements (Group IA) except Na are enriched in the greisens. Na, Group IIA elements (Mg, Ca, Sr and Ba), Zr, and Th are generally depleted compared to unaltered granite. Nb, Ta, and Be are generally depleted, but are enriched in a few samples of greisen. Most other elements (V, Co, Ga, Sb, Y, Sn, and U) are variably enriched. Rare earth element patterns have deep Eu anomalies and relatively low La/Yb ratios. A consistent pattern of Y and HREE enrichment (as much as 3 times) in greisens relative to unaltered granite is apparent. Enrichment of Y and HREE was controlled by the stability of xenotime (a HREE-Y-rich phosphate) in the greisens that appears to have repaced magmatic monazite (a LREE-rich phosphate). Due to the destruction of zircon during metasomatism, the fluids mobilized Zr and Th, generally thought to be immobile and controlled by magma

fractionation. Within the greisenized veins, fluid inclusions in quartz homogenize between 150 and 500 °C. The fluid apparently boiled at temperatures above 360 °C, making pressure corrections uneccesary. Fluid inclusion salinities range between 0 and 25 eq. wt.% NaCl; a few inclusions have halite daughter minerals and salinities of those reached 40-50 eq. wt.% NaCl. CO_2 is present in many of the inclusions. The post-magmatic fluids responsible for the formation of greisens in the Sheeprock granite were acidic and chlorine-, fluorine-, and carbon dioxide-bearing. The Sheeprock greisens commonly have magnetite and hematite as the principal Fe-minerals, suggesting that the f_{O2} of the hydrothermal fluids was too high (-27.5 log units) to carry enough Sn for economic mineralization.

INTRODUCTION

The rare-element granite of the Sheeprock Mountains in western Utah, U.S.A. is chemically and temporally equivalent to late Cenozoic topaz-bearing rhyolites of the eastern Great Basin--a part of the northern Basin and Range province. Weakly mineralized quartz-muscovite greisens developed along fractures and on the margins of some aplite dikes in the Sheeprock granite.

Greisen is hydrothermally altered granitic rock, consisting mainly of quartz, F-rich mica, and topaz. Fluorite and tourmaline are common accessory minerals. Lithophile ore metals (Sn, W, Ta, Nb, Be, Li, Mo) are typically enriched and greisenization accompanies the formation of many Sn and W deposits (Scherba, 1970). Geological studies of greisens can reveal hydrothermal fluid compositions, their formation temperatures and pressures, and help to further our understanding of post-magmatic processes in rare-element granites. This is particularly important in light of the controversy regarding the magmatic or metasomatic origin of the enrichments of incompatible elements characteristic of rare-element granites (e.g., Mackenzie et al., 1988; Higgins, 1990).

In this study of the Sheeprock granite, whole-rock chemical compositions were obtained for 13 samples (11 greisen samples and 2 unaltered granite samples) and about 600 fluid inclusions in quartz were studied from 13 greisen samples.

GEOLOGY

During the late Cenozoic (<21 Ma), lithospheric extension in the Basin and Range province was accompanied by the eruption of aluminous, A-type, topaz-bearing rhyolites

enriched in Be, U, Rb, Ta, F and other rare elements (Christiansen et al., 1986). These rhyolites are part of a bimodal mafic lava-rhyolite suite and are believed to be the volcanic equivalents of rare-element granites. The Sheeprock granite is a small pluton of the same chemical composition as these rhyolites. The granite is also the same age (20.9 Ma; Christiansen et al., 1988) as the topaz-bearing and Be-mineralized Spor Mountain rhyolite located 30 km to the southwest. Therefore, it may provide clues to the processes that lead to Be mineralization in igneous rocks of this type.

The pluton in the Sheeprock Mountains is only one of a number of Tertiary igneous complexes exposed along the east-trending Deep Creek-Tintic mineral belt (Shawe and Stewart, 1976; Stewart et al., 1977). The outcrop of the granite covers about 26 km^2, and is located along the southwest flank of the Sheeprock Mountains horst, about 90 km southwest of Salt Lake City, Utah (Figure 2.1). The pluton intrudes folded and faulted late Proterozoic quartzites, slates, phyllites, and diamictites, as well as Paleozoic carbonate rocks (Figure 2.1). Portions of the pluton's southern margins are covered by Cenozoic alluvium (Christie-Blick, 1982; Cohenour, 1959). Based on field evidence, the depth of emplacement is estimated to have been less than 1 km (Christiansen et al., 1988).

The magmatic minerals of the Sheeprock granite include K-feldspar, quartz, plagioclase, biotite, fluorite, ilmenite, and magnetite. Accessory minerals are zircon, apatite, Th-rich monazite, Nb-Ta-Y oxides, thorite, xenotime, and rare uraninite. In the differentiated core, late magmatic beryl rosettes developed and co-crystallized with albite, zinnwaldite, and ferrimuscovite. Samples of the Sheeprock granite have high SiO_2 contents (ranging from 75 to 77.5%), high Fe/Mg and K/Na ratios, high total alkali contents, and low Ti, Mg, Ca, and P

compared to the average low calcium granite of Nockolds (1954). Fluorine concentrations are much higher than in typical granite (0.06%), ranging up to 0.39%. In all of these characteristics, the Sheeprock granite is similar to topaz rhyolites from the eastern Great Basin and to aluminous A-type or anorogenic granites from other parts of the world (Collins et al., 1982; Whalen et al., 1987).

According to Christiansen et al. (1988), the Sheeprock pluton is geochemically zoned due to in situ fractional crystallization. The pluton's core (Figure 2.1) is texturally varied and relatively enriched in Li, Na, Rb, F, Sc, Be, Y, and HREE (heavy rare earth elements), and depleted in Th, Sr, Zr, LREE (light rare earth elements), Ti, Fe, Mg, Ca, K, and P. Coarse-grained granite and massive aplite around the core area are less chemically differentiated. The final crystallization of the granite probably took place at a temperature below 600 °C (Rogers, 1990). Such a low temperature is reasonable based on experiments with the chemically similar Spor Mountain rhyolite that has a water-saturated solidus of about 500 °C (Webster et al., 1987).

Numerous fractures with margins of quartz-muscovite greisen cut across the pluton. Most greisens are found outside the core area, and like those examined here cut the less differentiated margins of the Sheeprock granite. Cassiterite and tungsten minerals, principally wolframite, are associated with some of the greisens (Cohenour, 1959).

SAMPLES

Samples of vein quartz and their greisenized envelopes were collected along two nearly vertical WNW-striking fractures in granite and aplite in an apophysis of less differentiated granite in Joes Canyon on the eastern side of the main pluton (Figure 2.2). Greisenization was more

intense near the fractures and grades outward to relatively unaltered rock. Fracture A cuts through a one meter wide aplite dike. The hydrothermally precipitated materials filling fracture A are dark brown and strongly iron stained. Massive fine-grained greisen occurs along fracture A. Fine-grained greisen is dark green and varies from 2 to 15 cm in thickness. Fracture B cuts through medium-grained granite. Fracture B is filled with about 1 to 2 cm of polygranular quartz, some of which is vuggy. Massive coarse-grained greisen with a total thickness between 10 and 30 cm occurs along both sides of the quartz vein. Greisenization was more intense near the quartz vein of fracture B.

Greisen from both fractures has large (>1 mm) rounded quartz grains set in a finer matrix of quartz, opaque minerals, and randomly oriented sheaves of radiating muscovite crystals. Limonite spots after Fe oxide or sulfide minerals are disseminated through both A and B greisens. The greisen minerals include F- and Fe-rich muscovite, quartz, altered feldspar, fluorite, magnetite, hematite, and rare topaz. Scanning electron microscope studies showed monazite and xenotime. Xenotime rims monazite in an apparent metasomatic replacement of magmatic monazite.

Six samples of fine-grained (<0.5 mm) greisen and one sample of aplite were collected along fracture A. Three samples of quartz and two samples of coarse-grained (>2 mm) greisen were collected along fracture B (Figure 2.2). Greisen samples GR 1, 2, and 3 were collected from other outcrops in Joes Canyon for comparison. GR 2 was from a 50 cm-long greisen pod. In an attempt to compare the greisen-forming fluids with potentially magmatic fluids, one sample of milky quartz (GR 5) from a miarolitic cavity that lacks a greisen envelope was collected from medium-grained granite for fluid inclusion study.

WHOLE-ROCK GEOCHEMISTRY

For greisen samples, major elements (Si, Ti, Al, Fe, Mn, Mg, Ca, K, P) were analyzed using fused glass disks and a Phillips X-ray fluorescence (XRF) spectrometer interfaced with an IBM computer. The method of Norrish and Hutton (1969) was used for matrix correction. Sodium and trace elements (Rb, Sr, Y, Zr, Nb, Sc, V, Cr, Ni, Cu, Zn, Ga, Ba, La, Ce, Nd) were also analyzed by XRF using pressed powder pellets. Analytical accuracy based on replicate analyses of international reference materials is typically +/- 1% for major elements (except Na & P), +/- 5% for Na, P, Rb, Sr, Y, Zr, Nb, and +/- 10% for Sc, V, Cr, Ni, Cu, Zn, Ga, La, Ce, and Nd. Li and Be were analyzed by atomic absorption (AA) spectrometry. Sample powders were digested with concentrated reagent grade perchloric acid, allowed to evaporate, then dissolved in distilled water. Sn was analyzed by inductively coupled plasma (ICP) spectrometry. Solutions were prepared by fusing the samples in lithium metaborate and digestion in a weak acid. Analytical precision for AA and ICP was +/- 2% relative error. Accuracy is estimated to be +/- 10% based on comparisons with rocks also analyzed by the U.S. Geological Survey (Denver). Selected samples were also analyzed by INA (instrumental neutron activation) by Nuclear Activation Services Incorporated, Ann Arbor, Michigan. Based on repeat analyses of international reference materials, the accuracy of the technique is about +/- 10% for W, Cs, Nd, Sm, Eu, Tb, and Lu and within +/- 5% for Hf, Ta, Th, U, La, Ce, and Yb.

Table 1 shows compositions of greisen and two granite samples collected from Joes Canyon. In comparison to fresh granite, there are regular enrichment and depletion patterns (Figure 2.3) for the greisens as a whole. K, Hf, and LREE show relatively little change (+/- 10%). Sodium, alkaline earths (Be, Mg, Ca, Sr, and Ba), Zr, and Th are generally depleted.

Li, Al, Sc, Zn, Ga, P, Sn, Y, and HREE are enriched in most greisens, but not strongly (0.8 to 3.0 times). Mn, Fe, Sb, Rb, and Cs are strongly enriched (3 to 20 times). Other elements (Si, V, Ti, Nb, Ta, and U) are variably enriched or depleted. Tungsten in greisens (15 to 140 ppm) is almost certainly enriched over unaltered granite, but the granites were not analyzed for this element.

The chemical compositions of the greisens are mostly controlled by the relative proportions of 3 minerals--quartz, muscovite, and Fe oxides. This is seen in SiO_2 vs K_2O variations in the greisens (Figure 2.4). Deviation away from a simple mixing line between muscovite and quartz can be explained by introduction of Fe oxides. The hydrothermal alteration of the granite can be viewed as the introduction of quartz and/or the conversion of K-feldspar-plagioclase-biotite to muscovite plus quartz. The two samples with SiO_2 higher than 76% were dominated by addition of quartz and those with less SiO_2 and correspondingly higher K_2O were dominated by muscovite formation. As a result, K_2O correlates strongly with Al_2O_3, MnO, Rb, Cs, and Ga, all elements accommodated in muscovite. The correlation of Sn with this group of elements (Figure 2.5) suggests that a significant proportion of Sn is in muscovite.

Greisen along fractures A and B (Figure 2.2) formed from country rocks with different textures. Greisen along fracture A occurs in fine-grained aplite. Thicker greisen along fracture B formed next to a quartz vein directly in contact with medium-grained granite. Moreover, fracture A has a dark filling of what once may have been oxide and sulfide minerals and lacks the coarse, vuggy quartz of fracture B. Careful comparison of A and B greisens show some chemical differences (Figure 2.3). B greisens show stronger Be depletion; their Cu, Zn, Hf, Nb, and Ta contents are lower and similar to those in unaltered rocks, whereas concentrations in A

greisens are higher. TiO_2 shows little change in B greisen, but is depleted in most A greisens. W content of A greisens is as much as 6 times higher than that of B greisens.

Rare earth element patterns in greisen samples (Figure 2.6) are generally similar to those in the unaltered granite in that they have deep Eu anomalies and relatively low La/Yb ratios. In detail, however, a consistent pattern of HREE and Y enrichment in greisens emerges. LREE are slightly depleted; Eu and HREE and Y are enriched by as much as three fold. Even sample B5.2, which has the lowest total REE content, shows this same elevation of HREE/LREE ratio (Figure 2.5); however, in this latter sample only Yb, Lu, and Y are enriched in an absolute sense compared to unaltered granite.

Several geologists have studied element redistribution, including REE, between greisens and their parental granites. Chatterjee et al. (1984) and Higgins (1985) both showed similar LREE depletion and HREE enrichments in greisens as compared to unaltered granite. The data from the Sheeprock pluton showing the depletion of Zr and Th during greisenization is significant because Chatterjee (1984) suggested a magmatic control of Zr and Th and their immobility in the hydrothermal greisen-forming fluids. These data show that post-magmatic fluids can mobilize so-called "magmatically controlled" elements during greisenization, including Zr, Th, Ti, Ta, and Nb.

FLUID INCLUSION MICROTHERMOMETRY

All samples for heating and freezing experiments were doubly polished to 0.5 mm thick. These samples were studied under a petrographic microscope before the sections were broken into small chips for studies of fluid inclusions in quartz on a heating and freezing microscope

stage. Generally 10 to 25 fluid inclusions were measured during a single heating run and 2 to 3 chips per sample were studied. All cooling data were collected prior to heating runs and each chip was heated only once to minimize leakage and decrepitation of fluid inclusions.

Fluid inclusion studies were conducted on a Fluid Inc. gas-flow heating and freezing stage mounted on a Zeiss microscope. The stage was calibrated using the known melting points of liquid CO_2 (-56.6 °C), distilled water (0 °C), tin metal (231.97 °C), lead metal (327.43 °C) and cadmium iodide (385 °C). Based on this calibration, temperature corrections in the range -56.6 to 0 °C were -0.6 to -0.2 °C; in the range 0 to 500 °C corrections ranged from -0.2 to -3 °C. Repeat freezing runs usually indicated a reproducibility of +/-0.1 °C for the melting point of ice. Repeat tests of vapor-liquid homogenization show reproducibility of about 1 °C. Heating rates were approximately 1-2 °C/min near the temperatures of homogenization.

Four major types of fluid inclusions were identified based on phase relations at room temperature and homogenization behavior.

Type 1 inclusions are liquid-rich with vapor bubbles commonly occupying between 5 and 40 volume percent; they homogenize to liquid.

Type 2 inclusions are vapor-rich with a vapor bubble occupying greater than 70 volume percent; they homogenize to vapor. Inclusions with vapor content between 40 to 70 volume percent were grouped into either type 1 or type 2 depending on their homogenization behavior.

Type 3 inclusions are high-salinity inclusions that contain daughter minerals of halite. This type of inclusion can be further subdivided into two types based on homogenization behavior: type 3a are fluid inclusions in which halite dissolves at temperatures less than or equal

to the temperature of liquid-vapor homogenization. Type 3b are fluid inclusions in which halite dissolves at temperatures higher than that of liquid-vapor homogenization.

Type 4 inclusions are mixed H_2O-CO_2 fluids and CO_2 vapor; they homogenize to liquid or vapor. Included here are also inclusions in which CO_2 solid melted at -56.6 °C, but lacked evidence of CO_2 at higher temperature.

About 600 freezing points were measured for primary type 1, 2, 3, and 4 fluid inclusions in quartz from 12 samples of greisen (A2.5, A9.6, A10.5, A11.1, and A11.9; B1.0, B2.8, B6.5, and B12.0; and GR1, 2) and 1 sample of milky quartz (GR 5). The approximate salinities of these inclusions were calculated using the equation of Potter et al. (1978) for type 1 and 2 inclusions, the equation of Potter et al. (1977) for type 3 inclusions, and the equation of Bozzo et al. (1975) for type 4 inclusions.

Homogenization temperatures and fluid salinities

Type 1 inclusions are the most abundant inclusions (Figs. 7 and 8). Histograms show two modes for homogenization temperatures of type 1 inclusions (Figure 2.7); this bimodal pattern appears in all the samples from fractures A and B, GR1, 2, and 3, and the quartz pod. The high temperature mode ranges from 260 to about 400 °C with a few samples above 400 °C. These high temperature fluids were apparently trapped as the greisens formed, and they may be cooled magmatic fluids released from subjacent magma. Greisens in many other granites formed in this same temperature interval (Roedder, 1984; Haapala et al., 1979; Jackson et al., 1985b). The low temperature mode ranges from 130 to 250 °C. Type 1 fluid inclusions of this sort are commonly low in salinity (Figure 2.8). These inclusions may be of fluid formed by mixing

magmatic fluid with cool, dilute meteoric fluid in open fractures. The salinities of type 1 inclusions represent a continuum from low salinity inclusions with just over 0 NaCl eq. wt.% to moderate salinity inclusions with 5 to 27 NaCl eq. wt.% (Figure 2.8). The low salinity fluids are most abundant.

Vapor-rich or type 2 inclusions homogenize at rather high temperatures, from about 360 °C to 490 °C (Figure 2.7) (one type 2 inclusion decrepitated at 331 °C). This temperature range overlaps with the upper range of type 1 inclusions, and suggests that boiling of the hydrothermal fluid occurred at temperatures above about 360 °C. The overlap of homogenization temperature ranges of type 1 and 2 inclusions is reasonable evidence for boiling. Boiling is commonly reported for other greisens (e.g. Roedder, 1984). Boiling may have occurred over a wider temperature range, but experiments to determine homogenization temperature for many of this type of inclusion were inconclusive because vapor-rich inclusions are difficult to work with as noted by others (Roedder, 1984). Accordingly, Type 2 inclusions comprise a higher proportion of the population than indicated in Figures 7 and 8. The salinity of type 2 inclusions ranges from about 5-15 eq. wt.% NaCl. Low and high salinity inclusions are lacking (Figure 2.8).

If the fluid which formed the greisens was boiling, an estimate of trapping pressure can be made because the fluid must have been on the boiling curve in T-P space. It is suggested that 10 eq. wt.% NaCl is representative of the fluid responsible for greisenization of the Sheeprock granite; pressure estimates are not strongly influenced by the choice of NaCl concentration. Using this salinity (10 equiv. wt% NaCl) and the range of temperature overlap for type 1 and type 2 fluid inclusions (360-490 °C), the trapping pressure could have varied from 160 to 500 bars (Roedder and Bodnar, 1980). The latter investigators suggest the low pressure value may

place a meaningful upper limit for quartz crystallization. Transient higher pressures may have been caused by periodic closing of the veins during quartz crystallization (Roedder, 1984). Assuming lithostatic conditions, the pressure range of 160 to 500 bars corresponds to a depth range of 600 to 1500 m, in reasonable agreement with the field evidence for shallow emplacement of the Sheeprock granite.

The proportion of type 3 inclusions is not high, amounting to little over 1% of total studied. Thermometric data were obtained for only 7 inclusions, but they yield important information about the range of fluids present and processes that accompanied greisenization. Most salt crystals dissolved between 340 and 430 °C, indicating fluid salinities of 41 to 49 NaCl eq. wt.%. Liquid-vapor homogenization temperatures for type 3 inclusions overlap with those of type 1 and 2 in range from 330 to 400 °C (Figure 2.7 and 9). Five out of seven type 3 inclusions are type 3b. Their halite crystals dissolved at temperatures between 400 to 430 °C, higher than their liquid-vapor homogenization temperatures. The coincident homogenization temperatures of high salinity, vapor-rich, and vapor-poor inclusions are further evidence for boiling during greisen formation.

Many type 4 inclusions contain aqueous liquid, CO_2 liquid and CO_2 gas at room temperature. Type 4 inclusions had solid CO_2 when cooled below -56.6 °C. The presence of CO_2 causes the formation of a clathrate (CO_2 5.3/4 H_2O) that is a sensitive indicator of CO_2 in inclusion fluids. These CO_2-bearing inclusions constitute about 20% of those studied. Apparently a significant amount of CO_2 was present in the greisenizing fluids. Moreover, heterogeneous (CO_2-poor and CO_2-rich) fluids existed and passed through the same fracture system. The homogenization temperatures of this type of inclusion generally lie at the high

temperature end of the range for types 1, 2, and 3. Most type 3 inclusions them homogenized between 290 and 400 °C; a few homogenized below 200 °C (Figure 2.7). These CO_2-rich inclusions appear to have been trapped during boiling, since their homogenization temperatures overlap the type 2 and 3 inclusions. Moreover, many homogenize to the vapor state. The source of CO_2 may be magmatic or alternatively, may be the result of reduction of $CO_3^=$ ($2H^+ + CO_3^= => CO_2 + H_2O$) derived from Paleozoic carbonate rocks that border parts of the intrusion (Figure 2.1).

The salinities of type 4 inclusions are consistently higher than type 2 inclusions. They range between 10 to 20 eq. wt.% NaCl and lack very low and very high salinity types (Figure 2.8). There are several type 4 inclusions which contain phases that melted at -83.7 °C and -68.3 °C. This might be caused by the presence of methane (CH_4) or some other unidentified component. One CO_2-rich inclusion with clathrate melted at 10.2 °C, higher than the 10 °C, melting point of CO_2 clathrate in pure H_2O. If not the result of a calibration error, this may also indicate the presence of other components in this inclusion in addition to CO_2 (Collins, 1979).

Type 1, 2, 3, and 4 fluid inclusions exist in all the samples examined including the milky quartz (GR 5). There are no obvious differences in homogenization temperature or fluid salinity between the different fractures or of samples along a given fracture. However, the proportion of CO_2-rich inclusions in milky quartz from a miarolitic cavity in the granite (GR 5) is much less than that of samples from fractures A and B. In this sample, only one inclusion was found with detectable CO_2.

Twenty-one secondary or pseudo-secondary fluid inclusions were studied, making about 3% of total examined. Most are type 1 inclusions; one is a type 4 inclusion. Their

homogenization temperatures are rather low, most fall around 160 °C; only three inclusions homogenize over 300 °C. Their salinities are low; only two reach 8 NaCl eq. wt.%.

GREISENIZATION MODEL

In many granitic rocks, post-magmatic hydrothermal fluids play an important role in element migration and mineralization. After at least partial solidification of the Sheeprock granite, acidic fluorine-, chlorine-, and carbon dioxide-bearing hydrothermal fluids formed, perhaps by fluid saturation of the differentiating magma and/or by introduction of meteoric water convecting around the pluton. Fluid inclusion melting temperatures show that the hydrothermal fluid salinity was low to moderate, from a little over 0 to 27 eq. wt.% NaCl; only rare type 3 inclusions contain more saline fluids, exceeding 40 eq. wt.% NaCl. The most abundant inclusions have low salinities (<10 eq. wt.% NaCl). Moreover, boiling of the hydrothermal fluid during greisenization is indicated, at least in the high temperature range (350 to 500 °C). Boiling may have been in response to one or more fracture-induced drops in pressure. For fluids with homogenization temperatures below 350 °C, boiling is not indicated; perhaps greisenization had already sealed the veins and pressure had risen accordingly. The evidence for boiling makes pressure corrections unnecessary for the highest homogenization temperatures; these homogenization temperatures must represent trapping temperatures. The data do not indicate clearly whether the fluids were dominantly meteoric or magmatic. Nonetheless, as these fluids flowed through fractures they reacted with granitic wall rocks to produce what appears to be an equilibrium assemblage of quartz, muscovite (Fe and F-rich, E. H. Christiansen, unpublished analyses), fluorite, magnetite, hematite, and rarely topaz in the greisens.

The mineral assemblage can be used to infer more about the chemical character of the hydrothermal fluid and some of the conditions of greisenization, but these inferences must be tempered by the fact that muscovite is not a pure end-member phase--it contains substantial Fe and F. To estimate the activities of various components in the hydrothermal fluid, the activity diagrams for 350 °C and 500 bars constructed by Jackson and Helgeson (1985b) were used. Such conditions are close to those inferred for greisenization of the Sheeprock granite from microthermometry. The apparent co-existence of hematite and magnetite constitutes an oxygen buffering assemblage and, under the conditions noted above, fixes log f_{O2} at about -27.5. Log a_{K+}/a_{H+} is loosely constrained to lie between 2 and 3.8 by the presence of quartz and muscovite and absence of K-feldspar and pyrophyllite. The absence of topaz in most greisens from the Sheeprock Mountains places an upper limit of -9.7 to -10.2 for log a_{H+}/a_{F-}. Likewise, the absence of albite in the altered rocks places an upper limit of 3.2 to 4.3 for log (a_{Na+}/a_{H+}). These conditions are similar to those deduced by Jackson and Helgeson (1985b) for Sn-mineralized greisens in southeast Asia, but there are several significant differences. For example, Jackson and Helgeson (1985b) concluded that K-feldspar and topaz coexisted with quartz and muscovite yielding higher a_{K+}/a_{H+} and a_{H+}/a_{F-}. Moreover, inferred oxygen fugacities were roughly 3.5 orders of magnitude lower in the southeast Asian greisens than in those examined here.

In short, it is concluded that at a temperature of less than about 500 °C the hydrothermal fluid described above reacted with granite forming quartz-muscovite greisen along fluid flow paths. As a result of phase changes and chemical exchange with the fluid, the concentrations of most major and trace elements in the granite were affected. As noted above, all alkaline earths

(Be, Mg, Ca, Sr and Ba), Zr, and Th were depleted in the greisens relative to unaltered granite. Most alkalies (Li, K, Rb and Cs), and first row transition elements (Sc, V, Mn, Fe, Cu, Zn) were enriched along with Ga, Sn, and W. REE patterns rotated and greisens became enriched in Y and HREE. Moreover, some so-called "magmatically controlled" elements (e.g., Zr, Hf, Th, Nb, Ta) were mobilized.

Most of the compositional changes can be explained by the mineralogical changes that occurred when granite was converted to greisen. The following reactions account for the most important mineralogical changes during greisenization:

$$\underset{\text{K-feldspar}}{3KAlSi_3O_8} + 2F_2O_{-1} \Rightarrow \underset{\text{muscovite}}{KAl_3Si_3O_{10}(F)_2} + \underset{\text{quartz}}{6SiO_2} + \underset{\text{aqueous}}{2KF} \quad (1)$$

$$\underset{\text{plagioclase}}{3CaAl_2Si_2O_8} + 4F_2O_{-1} + \underset{\text{aqueous}}{2KF} \Rightarrow \underset{\text{muscovite}}{2KAl_3Si_3O_{10}(F)_2} + \underset{\text{fluorite}}{3CaF_2} \quad (2)$$

$$\underset{\text{plagioclase}}{3NaAlSi_3O_8} + 2F_2O_{-1} + \underset{\text{aqueous}}{KF} \Rightarrow \underset{\text{muscovite}}{KAl_3Si_3O_{10}(F)_2} + \underset{\text{quartz}}{6SiO_2} + \underset{\text{aqueous}}{3NaF} \quad (3)$$

$$\underset{\text{siderophyllite}}{12KFe_{2.5}Al_2Si_{2.5}O_{10}FOH} + \underset{\text{aqueous}}{7.5O_2} + 4F_2O_{-1} \Rightarrow$$

$$\underset{\text{muscovite}}{8KAl_3Si_3O_{10}F_2} + \underset{\text{hematite}}{15Fe_2O_3} + \underset{\text{quartz}}{6SiO_2} + \underset{\text{aqueous}}{4KF} + 6H_2O \quad (4)$$

Trace and minor constituents ignored in these simplified reactions were also affected. For example, the destruction of K-feldspar and plagioclase led to strong depletions of Na and Ca, as well as Sr, and to a lesser extent, Ba (partially accommodated in muscovite). The reaction of Fe-rich biotite to form muscovite, quartz, and an Fe-oxide left the greisen depleted in Ti and Mg. In addition, even resistant minerals, like zircon and perhaps thorite were destroyed resulting in depletions in Th and U. The metasomatic production of muscovite produced mineralogical sites for Li, Rb, Cs, Mn, Fe, Ga, and perhaps Sn, creating the enrichments and co-variations

of these elements in the greisens. Enrichments (or at least lack of depletions) of other elements were controlled by the growth of secondary oxides (Fe, Mn, Nb, Ta, W, Sn), minor sulfides (Sb, Cu, Zn), and xenotime (Y, HREE, P) that partially replaced monazite. Apparently immobile elements, like K, Al, Ti and some REE, were accommodated in roughly equal proportions in the magmatic rock and the metasomatic mineral assemblage that replaced it.

The growth of hydrothermal xenotime may have been fueled by the transport of HREE and Y in the relatively F-rich hydrothermal fluids that produced the greisens. Balashov et al. (1975) suggested that F- and CO_2-rich fluids control the migration of HREE in hydrothermal fluids. This latter idea is supported by the HREE enrichment seen in the Sheeprock greisens and in several other studies of greisenized rocks (Bilal et al., 1979; Muecke et al., 1981; Chatterjee et al., 1984; Higgins, 1985). Flynn and Burnham (1978) suggested from experimental evidence that Cl-rich fluids are most effective in transporting LREE. Depletions of light REE in the metasomatic rocks compared to granite were limited because of the introduction of additional xenotime and only partial replacement of monazite.

The greisens of the Sheeprock granite are not strongly mineralized, even though the unaltered Sheeprock granite is strongly enriched in rare elements compared to other granites that produced ore deposits. Sn, W, Li, and Ta are only enriched in the greisen by several times that found in the original granite. Fluid inclusion homogenization temperatures and salinities in the Sheeprock greisens fall in the typical range for greisens containing significant Sn and W deposits (e.g. Roedder, 1984). Therefore, it is unlikely that temperature or chloride ion concentrations are the principal causes of the lack of mineralization. The fluorine-rich micas, fluorite, and rare topaz also show that fluorine activities were comparable to other greisens, thus eliminating low

fluoride ion concentrations as a limiting factor. Possible causes for the slight mineralization include:

1. The pluton may not have been large enough to supply the requisite quantity of Sn or W. Keith et al. (1990) have pointed out that in economic ore deposits, metals are probably extracted from large bodies of magma and/or solid granite.

2. Erosion may have stripped mineralized greisens from an area above the most differentiated granite (Figure 2.1), leaving only sparsely mineralized veins on the flanks of the intrusion. Mineralized greisens commonly form in or above the most evolved granite in an intrusion (Scherba, 1970). In the Sheeprock granite, greisens are less abundant in the evolved core, but the roof over this part of the intrusion has been eroded away.

3. The oxygen fugacity of the hydrothermal fluid may have been too high for significant transport of Sn. The Sheeprock greisens have magnetite and hematite as the principal Fe-minerals, demonstrating that the oxygen fugacity of the hydrothermal fluids was high at the time of greisenization. As noted above, at 350 °C and 500 bars, the oxygen fugacity of hydrothermal fluid responsible was about -27.5 log units. Many economic deposits of Sn contain pyrrhotite, magnetite, and pyrite as Fe-minerals (see review in Jackson and Helgeson, 1985b), indicating substantially lower oxygen fugacities--near log f_{O2} of -31 at 350 °C and 500 bars (Jackson and Helgeson, 1985b). The solubility of cassiterite in pure water and in the presence of hematite and magnetite is very low (Figure 2.10). The high oxygen fugacity and low cassiterite solubility may explain the lack of Sn mineralization in the Sheeprock granite.

ACKNOWLEDGEMENTS

We thank B. J. Kowallis, A. L. Mayo, and M.G. Best for their helpful critiques of the manuscript, W. P. Nash for assistance with electron microprobe analyses, D. Tingey for help with XRF analyses, W. Brimhall for assistance with ICP and AA analyses, and T. Blatter for help with computer drafting. Funds to support this project were provided by the Utah Geological and Mineral Survey (Contract 89-0071) and a grant from the BYU Department of Geology.

REFERENCES CITED

Aurisicchio, C., Fioravanti, G., Grubessi, O., and Zanazzi, P.F., 1988, Reappraisal of the crystal chemistry of beryl: American Mineralogist, v. 73, p. 826-837.

Balashov, Y. A., and Kligman, L. D., 1975, The effects of alkalinity and volatiles on rare-earth separations in magmatic systems: Geokhimiya, v. 12, p. 1885-1890.

Barton, M. D., 1982, The thermodynamic properties of topaz solid solutions and some petrologic applications: American Mineralogist, v. 67, p. 956-974.

Barton, M. D., 1986, Phase equilibria and thermodynamic properties of minerals in the BeO-Al_2O_3-SiO_2-H_2O (BASH) system, with petrologic applications: American Mineralogist, v. 71, p. 277-300.

Bilal, B. A., and Becker, P., 1979, Complex formation of trace elements in geochemical systems, II. Stability of rare earth fluoro complexes in fluorite-bearing model systems of various ionic strengths: Journal of Inorganic and Nuclear Chemistry, v. 41, p. 1607-1608.

Beus, A. A., 1966, Geochemistry of beryllium and genetic types of beryllium deposits: W.H. Freeman and Company, San Francisco, 401 p.

Bozzo, A. T., Chen, H.-S., Kass, J. R., and Barduhn, A. J., 1975, The properties of the hydrates of chlorine and carbon dioxide: Desalination, v. 16, p. 303-320.

Bullock, K. C., 1964, Minerals of Utah: Utah Geological and Mineral Survey Bulletin 76, 237 p.

Bullock, K. C., 1981, Minerals and mineral localities of Utah. Utah Geological and Mineral Survey Bulletin, 117, 177 p.

Burnham, C. W., 1979, Magmas and hydrothermal fluids, in Barnes, H.L. (ed.), Geochemistry of hydrothermal ore deposits: Wiley-Interscience, 2nd ed., 71-136.

Burt, D. M., 1975, Beryllium mineral stabilities in the model system CaO-BeO-SiO_2-P_2O_5-F_2O_{-1} and the breakdown of beryl: Economic Geology, v. 70, p. 1279-1292.

Burt, D. M., 1978, Multisystem analysis of beryllium mineral stabilities: The system BeO-Al_2O_3-SiO_2-H_2O: American Mineralogist, v. 63, p. 664-676.

Burt, D. M., 1981, Acidity-salinity diagrams-Applications to greisen and porphyry deposits: Economic Geology, v. 76, p. 822-843.

Carmichael, I. S. E., Turner, F. J., and Verhoogen, J., 1974, Igneous petrology: McGraw-Hill, New York, 739 p.

Černý, P., and Burt, D. M., 1984, Paragenesis, crystallochemical characteristics, and geochemical evolution of micas in granite pegmatites: Mineralogical Society of America Reviews in Mineralogy, v. 13, p. 257-297.

Chatterjee, A. K., and Strong, D. F., 1984, Rare-earth and other element variations in greisens and granites associated with East Kemptville tin deposit, Nova Scotia, Canada: Transaction of the Institution of Mining and Metallurgy, section B, Applied Earth Science, v. 93, p. B59-B70.

Christiansen, E. H., Bikun, J. V., Sheridan, M. F., and Burt, D. M., 1984, Geochemical evolution of topaz rhyolites from the Thomas Range and Spor Mountain, Utah: American Mineralogist, v. 69, p. 223-236.

Christiansen, E. H., Sheridan, M. F., and Burt, D. M., 1986, The geology and geochemistry of Cenozoic topaz rhyolites from the western United States: Geological Society of America Special Paper 205, 82 p.

Christiansen, E. H., Stuckless, J. S., Funkhouser-Marolf, M. J., and Howell, K. H., 1988, Petrogenesis of rare-metal granites from depleted crustal sources: An example from the Cenozoic of western Utah, U.S.A.: Recent advances in the geology and geochemistry of granite-related mineral deposits, CIM Special Publication 39, p. 307-321.

Christie-Blick, N., 1982, Upper Proterozoic and lower Cambrian rocks of the Sheeprock Mountains, Utah: Regional correlation and significance: Geological Society of American Bulletin, v. 93, p. 735-750.

Cohenour, R. E., 1959, Sheeprock Mountains, Tooele and Juab Counties: Precambrian and Paleozoic stratigraphy, igneous rocks, structure, geomorphology and economic geology: Utah Geological and Mineral Survey Bulletin, 63, 201 p.

Cohenour, R. E., 1963a, The beryllium belt of western Utah. Guide Book to the Geology of Utah: Beryllium and uranium mineralization in western Juab County, Utah, v. 17, p. 4-7.

Cohenour, R. E., 1963b, Beryllium and associated mineralization in the Sheeprock Mountains: Guide Book to the Geology of Utah, v. 17, p. 8-13.

Collins, P. L. F., 1979, Gas hydrates in CO_2-bearing fluid inclusions and use of freezing data for estimation of salinity: Economic Geology, v. 74, p. 1435-1444.

Collins, W. J., Beams, S. D., White, A. J. R., and Chappell, B. W., 1982, Nature and origin of A-type granites with particular reference to south-eastern Australia: Contributions to Mineralogy and Petrology, v. 80, p. 189-200.

Congdon, R. D., and Nash, W. P., 1988, High-fluorine rhyolite: An eruptive pegmatite magma at the Honeycomb Hills, Utah: Geology, v. 16, p. 1018-1021.

Elkins, L. T., and Groves, T. L., 1990, Ternary feldsparexperiments and thermodynamic models. American Mineralogist, v. 75, p. 544-559.

Fenn, P. M., 1977, The nucleation and growth of alkali feldspars from hydrous melts: Canadian Mineralogist, v. 15, p. 135-161.

Flynn, R. T., and Burnham, C. W., 1978, An experimental determination of rare-earth partition coefficients between a chloride containing vapor phase and a silicate melt: in Drake, M. J., and Holloway, J. R., eds., Experimental trace element geochemistry: Oxford, Pergamon Press, p. 685-701.

Foster, M. P., 1960, Interpretation of the composition of lithium micas: U.S. Geological Survey Professional Paper 354-E, 115-146.

Fowkes, E. J., 1964, Pegmatites of Granite Peak Mountain, Tooele County, Utah. Brigham Young University Geology Studies, v. 13, p. 97-127.

Funkhouser-Marolf, M. J., 1985, The mineralogy and distribution of uranium and thorium in the Sheeprock granite, Utah: M.S. thesis, University of Iowa, Iowa City, 60 p.

Griffitts, W. R., 1965, Recently discovered Be deposits near Gold Hill, Utah: Economic Geology, v. 60, p. 1298-1305.

Griffitts, W. R., Larrabee, D. M., and Norton J. J., 1962, Beryllium in the United States: U.S.G.S. Mineral Investigations Resource Map, MR-35.

Guidotti, C. V., 1984, Micas in metamorphic rocks: Mineralogical Society of America Reviews in Mineralogy, v. 13, p. 357-467.

Harris, D. K., 1958, The geology of Dutch Peak area, Sheeprock Range, Tooele County, Utah. Brigham Young University Research Studies, Geology Series, v. 5, p. 1-82.

Haapala, I. J., and Kinnunen, K., 1979, Fluid inclusions in cassiterite and beryl in greisen veins in the Eurajoki stock, southwestern Finland: Economic Geology, v. 74, p. 1231-1238.

Haapala, I. J., 1988, Metallogeny of the Proterozoic rapakivi granites of Finland: Recent advances in the geology and geochemistry of granite-related ore deposits: CIM Special Volume 39, p. 124-132.

Higgins, N. C., 1985, Wolframite deposition in a hydrothermal vein system: the Grey River Tungsten Prospect, Newfoundland, Canada: Economic Geology, v. 80, p. 1297-1327.

Higgins, N. C., 1990, Comment on "Origin of alkali-feldspar granites: An example from the Poimena Granite, northeastern Tasmania, Australia II: Geochimica et Cosmochimica Acta, v. 54, p. 2305-2311.

Jackson, K. J., and Helgeson, H. C., 1985a, Chemical and thermodynamic constraints on the hydrothermal transport and deposition of tin: I. Calculation of the solubility of cassiterite at high pressures and temperatures: Geochimica et Cosmochimica Acta, v. 49, p. 1-22.

Jackson, K. J., and Helgeson, H. C., 1985b, Chemical and thermodynamic constraints on the hydrothermal transport and deposition of tin: II. Interpretation of phase relations in the southeast Asian tin belt: Economic Geology, v. 80, p. 1365-1378.

Keith, J. D., van Middelaar, W., Clark, A. H., and Hodgson, C. J., 1990, Granitoid textures, compositions, and volatile fugacities associated with the formation of tungsten-dominated skarn deposits: Ore Deposition Associated with Magmas, Reviews in Economic Geology, v. 4, p. 235-248.

Kwak, T. A. P., and Askins, P. W., 1981, Geology and genesis or the F-Sn-W (Be-Zn) skarn (wrigglite) at Moine, Tasmania: Economic Geology, v. 76, p. 439-467.

Lee, D. E., and Erd, R. C., 1963, Phenakite from Mount Wheeler area, Snake Range, White Pine County, Nevada: American Mineralogist, v. 48, p. 189-193.

Lofgren, G., 1974, An experimental study of plagioclase crystal morphology: isothermal crystallization: American Journal of Science, v. 274, p. 243-273.

Luhr, J. F., Carmichel, I. S. E., and Varecamp, J. C., 1984, The 1982 Eruption of El Chichon Volcano, Chiapas, Mexico: Mineralogy and Petrology of the anhydrite-bearing pumices: Journal of Volcanology and Geothermal Research, v. 23, p. 69-108.

Mackenzie, D. E., Black, L. P., and Sun, S.-S., 1988, Origin of alkali-feldspar granites: An example from the Poimena Granite, northeastern Tasmania, Australia: Geochimica et Cosmochimica Acta, v. 52, p. 2507-2524.

Monier G., Mergoil-Daniel, J., and Labernardiére, H., 1984, Generations successives de muscovites et feldspaths potassiques dans les leucogranite du Massif de Millevaches (Massif Central Francais): Bulletin de Mineralogie, v. 197, p. 55-68.

Muecke, G. K., and Clarke, D. B., 1981, Geochemical evolution of South Mountain Batholith of Nova Scotia: Rare earth element evidence: Canadian Mineralogist, v. 19, p. 133-145.

Munoz, J. L., 1984, F-OH and Cl-OH exchange in micas with applications to hydrothermal ore deposits: Mineralogical Society of America Reviews in Mineralogy, v. 13, p. 469-493.

Nockolds, S. R., 1954, Average chemical compositions of some igneous rocks: Geological Society of America Bulletin, v. 65, p. 1007-1032.

Norrish, K., and Hutton, J. T., 1969, An accurate X-ray spectrographic method for the analysis of a wide range of geological samples: Geochimica et Cosmochimica Acta, v. 33, p. 431-453.

Potter, R. W., Babcock, R. S., and Brown, D. L., 1977, A new method for determining the solubility of salts in aqueous solutions at elevated temperatures: U.S. Geological Survey Journal of Research, v. 5, p. 389-395.

Potter, R. W., Clynne, M. A., and Brown, D. L., 1978, Freezing point depression of aqueous sodium chloride solutions: Economic Geology, v. 73, p. 284-285.

Reid, R. R., 1963, Reconnaissance geology of the Sawtooth Range. Idaho Bureau of Mines and Geology, Pamphlet 129, 37 p.

Roedder, E., and Bodnar, R. J., 1980, Geological pressure determinations from fluid inclusion studies: Annual Reviews of Earth and Planetary Science, v. 8, p. 263-301.

Roedder, E., 1984, Fluid Inclusions: Mineralogical Society of America Reviews in Mineralogy, v. 12, 456 p.

Rogers, J. R., 1990, Origin of beryl in the Miocene Sheeprock granite, west-central Utah: M. S. thesis, Brigham Young University, 48 p.

Scherba, G. N., 1970, Greisens: International Geology Review, v. 12, p. 114.

Shawe, D. R., 1966, Arizona-New Mexico and Nevada-Utah beryllium belts: U.S. Geological Survey Professional Paper, 550-C, p. C206-C213.

Shawe, D.R. and Stewart, J.H., 1976, Ore deposits as related to tectonics and magmatism, Nevada and Utah: Transaction of American Institute of Mining and Engineering, v. 260, p. 225-232.

Shigley, J. E., and Foord, E. E., 1985, Gem-quality red beryl from the Wah Wah Mountains, Utah: Gem and Gemology, v. 4, p. 208-221.

Speer, J. A., 1984, Micas in igneous rocks: Mineralogical Society of America Reviews in Mineralogy, v. 13, p. 299-356.

Staatz, M. H., 1963, Geology of the beryllium deposits in the Thomas Range Juab County, Utah: U. S. Geological Survey Bulletin 1142-M, 36 p.

Stewart, J. H., Moore, W. J., and Zeitz, I., 1977, East-west patterns of Cenozoic igneous rocks, aeromagnetic anomalies, and mineral deposits, Nevada and Utah: Geological Society of America Bulletin, v. 88, p. 67-77.

Turley, C. H., and Nash, W. P., 1980, Volcanism in western Juab and Millard counties, Utah: Utah Geological and Mineral Survey Special Studies 52, pt. 1, p. 1-33.

Webster, J. D., Holloway, J. R., and Hervig, R. L., 1987, Phase Equilibria of a Be, U, and F-enriched vitrophyre from Spor Mountain, Utah, Minerology, geology, and chemistry of granites and pegmatites: Geochimica et Cosmochimica Acta, v. 51, p. 389-402.

Weidner, J. R., and Martin, R. F., 1987, Phase equilibria of a fluorine-rich leucogranite from the St. Austell pluton, Cornwall: Geochimica et Cosmochimica Acta, v. 51, p. 1561-1597.

Whalen, J. B., Currie, K. L., and Chappell, B. W., 1987, A-type granites: geochemical characteristics, discrimination and petrogenesis: Contributions to Mineralogy and Petrology, v. 95, p. 407-419.

Whitebread, D. H., and Lee, D. E., 1961, Geology of the Mount Wheeler Mine area, White Pine County, Nevada: U.S. Geological Survey Professional Paper, 424-C, p. 120-122.

Williams, N. C., 1954, Nonpegmatite beryl occurrence, Sheeprock Mountains, Utah: Geological Society of America Abstracts with Program, 65, 1388.

FIGURE CAPTIONS

SECTION 1

Figure 1.1 Beryllium mineral occurrences in the northeastern Basin and Range province. Open circles represent beryl in granite and pegmatite, half-filled circles represent beryl in rhyolite, and filled circles represent beryl in veins. After Griffitts et al. (1962).

Figure 1.2 Generalized geologic map of the Sheeprock Mountains (Cohenour, 1959). Hachured line delineates the evolved central part of the pluton (group 1 samples, see text). Locations of rosettes collected are shown by numbers (1-HBC1; 2-HBCV1; 3-HBC2, 3, 6, 7; 4- HBC3M and HBC5; and 5-SRC1). GB = Great Basin; SLC = Salt Lake City; SM = Sheeprock Mountains; CP = Colorado Plateau; H = Hard-to-Beat Canyon, and S = Sheeprock Canyon.

Figure 1.3 Schematic cross section of a typical beryl rosette. Rosettes contain inclusions of albite, quartz, micas, and Ta-Nb-Fe-Mn-Ti oxides. The granite is fine-grained and composed of quartz, K-feldspar, plagioclase, and micas.

Figure 1.4 Photographs and photomicrographs of beryl in the Sheeprock granite.

(a) Slabbed beryl rosette (HBC2) showing long slender prismatic crystals, field of view is 6 cm.

(b) Beryl rosette as found in Sheeprock granite. Note the subspherical shape and crystal morphology. Rosette is 15 across.

(c) Photomicrograph of rosette showing poikilitic beryl (B, at extinction) with oikocrysts of albite (A), and a large crystal of albite (A) with intergrown micas (zinnwaldite and ferrimuscovite). Field of view is 1 mm.

(d) Large quartz (Q) grain with a "C" shape next to albite (A), both of which are surrounded by beryl (B, at extinction). Field of view 1 mm.

(e) Outer margins of beryl rosette; quartz is abundant but the grains have embayments indicating that they were not stable. Field of view is 3 mm.

(f) Photomicrograph of the central region of a rosette; quartz is not as abundant as at rim, the grains are smaller and are more deeply embayed than those of the margin. Field of view is 3 mm.

(g) Fluorite (extinct) within beryl rosette. Field of view is 2 mm.

(h) Disseminated beryl within the group 1 granitic host. Field of view is 6 cm.

(i) K-feldspar with anhedral blebs of beryl indicating a metasomatic origin. Field of view is 4 mm.

(j) Quartz vein (V) with beryl in the group 1 granitic host. Field of view is 6 cm.

(k) Photomicrograph of beryl (B) within quartz (Q) vein. Field of view is 2 mm.

Figure 1.5 Compositions of dark micas from beryl rosettes (filled squares) and granites (open squares) in the Sheeprock granite shown in the K-Li-Fe-Al-Si mica composition plane (Cerny and Burt, 1984). Li was calculated from electron microprobe analyses by assuming all dark micas are trioctahedral with not octahedral vacancies. End members are labelled: Znw = zinnwaldite; Pr = protolithionite; Tri = trilithionite; and Pol = polylithionite. The dark mica compositions in rosettes seem to be controlled by the Li_2SiFe_{-3} exchange vector. Lines of equal Fe, Al, Si and Li are shown.

Figure 1.6 Compositions of white micas (*) from the Sheeprock granite in the K-Fe-Al-Si mica composition plane for Li-free micas (Cerny and Burt, 1984). End member names are

given. Leucophyllite is the name applied by Bailey (1984) to the "Fe-Al celadonite" used by Cerny and Burt (1984). Lines of equal Fe, Al, Si and calculated octahedral vacancies are shown.

Figure 1.7 Micas in the Sheeprock granite acquired higher Fe/Mg ratios as the granite evolved. Large letters represent dark micas, small letters are white mica compositions.

Figure 1.8 Concentrations of Fe and Ti are lower in micas from more evolved samples of the Sheeprock granite and presumably reflect lower temperatures of equilibration.

Figure 1.9 Micas in the Sheeprock granite show F enrichment and Cl depletion in more evolved samples. Intercept values (IV) were calculated according to Munoz (1984).

Figure 1.10 Dark micas (biotite in granite and zinnwaldite in beryl bearing rocks) in the Sheeprock granite have simultaneously higher Fe/Mg and intercept values for F indicating progressively higher HF fugacities as the granite fractionated.

Figure 1.11 Histogram of F intercept values (IV (F)) for white mica (ferrimuscovite) and dark mica (zinnwaldite) in beryl rosettes from the Sheeprock granite. The overlap suggests that both micas crystallized simultaneously. Relative F enrichment increases to the left. The ranges for various mica types shown are taken from Munoz (1984); the square represents the mode of each range. Henderson Mo = stockwork molybdenite deposit; Sn-W-Be = granites and altered rocks associated with these metals; Cu = porphyry copper deposits; Igneous = unaltered igneous rocks.

Figure 1.12 Plagioclase compositions from the Sheeprock granite. Inset show compositions of two feldspars in rocks with disseminated and vein beryl. Symbols as in Table 2.

Figure 1.13 Correlation of alkali elements comprising the channel structures and the sum of the divalent cations in beryl from the Sheeprock granite compared beryl from many localities analyzed by Aurisicchio et al. (1988).

Figure 1.14 Enrichment diagrams showing elements enriched or depleted in (top) rosettes, (middle) granitic host, and (bottom) granite containing disseminated beryl as compared to an average differentiated granite (group 1) from the core of the Sheeprock granite.

Figure 1.15 REE patterns for beryl rosettes, their granitic hosts, and granite with disseminated beryl.

Figure 1.16 Ternary phase diagram for the quartz-albite-orthoclase-anorthite-water system projected onto Q-Ab-Or (after Carmichael et al., 1974). Dotted lines represent cotectics in the system under some arbitrary high pressure and solid lines represent the system at a lower pressure. Square = the differentiated Sheeprock granite melt in equilibrium with quartz, sodic plagioclase, and K-feldspar. A drop in pressure would cause crystallization of only albite, in the simplified system, until the position of the new low pressure minimum was achieved.

Figure 1.17 Rb and Nb became enriched as the granite differentiated. Numbers represent the different compositional groups identified in the granite with group 1 samples being the most differentiated and group 3 the least differentiated.

Figure 1.18 Ta and Nb variations show the progressive differentiation of the Sheeprock granite. The granitic hosts of the beryl rosettes are among the most evolved samples yet identified in the intrusion. (Symbols are the same as those in Figure 1.17.)

Figure 1.19 Schematic cross section of the Sheeprock granite magma chamber illustrating the inward crystallization (arrows) of the granite and the concentration of Be and H_2O in the core of the intrusion. Fluid saturation may have caused fracturing and consequent quenching of residual magma in the core of the chamber. Beryl rosettes apparently formed from scattered pockets of Be-rich melt created during this rapid phase of crystallization.

SECTION 2

Figure 2.1. Schematic geologic map of the granite of the Sheeprock Mountains (after Cohenour, 1959). The differentiated core of the intrusion contains beryl and high concentrations of incompatible elements. Greisen-bordered veins are most common outside of the differentiated core. Paleozoic sedimentary rocks (Ps) are mostly marine carbonates. Locations on the map include JC = Joes Canyon; SLC = Salt Lake City; GB = Great Basin; CP = Colorado Plateau.

Figure 2.2. Schematic geologic map of greisen sampling area in Joes Canyon (112°28′09″; 39°56′01″--enlarged part of Figure 1, width is exaggerated).

Figure 2.3. Trace element enrichment and depletion factors for greisenized rocks from the Sheeprock granite. Element or oxide concentrations in each greisen sample divided by concentrations in average unaltered granite from Joes Canyon (SR16 and SR17 in Table 1).

A) Samples of greisen along fracture A.

B) Samples of greisen along fracture B, as well as samples GR1, GR2, and GR3.

Figure 2.4. K_2O vs. SiO_2 for greisens and granites from Joes Canyon, Sheeprock granite. Compositions of quartz and muscovite are also indicated. Fe2O3 concentrations are listed beside each point.

Figure 2.5. Rb vs. Sn in greisens and granite from the Sheeprock granite. The good correlation suggests Sn is hosted in muscovite, the principal Rb-bearing phase in the greisens. Sn is also correlated with Al, Mn, Cs, and Ga, but poorly correlated with Fe.

Figure 2.6. Rare earth element patterns for greisens and average granite (Christiansen et al., 1988) found in the Joes Canyon portion of the Sheeprock granite.

Figure 2.7. Histogram of fluid inclusion homogenization (vapor-liquid) temperatures in greisens from Sheeprock granite.

Figure 2.8. Histogram of fluid inclusion salinities in greisens from Sheeprock granite.

Figure 2.9. Vapor-liquid homogenization temperature vs. fluid inclusion salinity for greisens from the Sheeprock granite. Numbers represent inclusion types (see text).

Figure 2.10. Solubility of cassiterite expressed as total molality of dissolved tin (mt, Sn) and ppm Sn as a function of oxygen fugacity and temperature (at pressures corresponding to the liquid-vapor equilibrium curve for H_2O = P SAT). Oxygen fugacities correspond to the fayalite-magnetite-quartz (FMQ), nickel-nickel oxide (Ni-NiO), and magnetite-hematite (Mt-Hm) buffers (after Jackson and Helgeson, 1985a). Greisens in the Sheeprock granite contain magnetite and hematite, suggesting that Sn solubility was very low as a result of high oxygen fugacities.

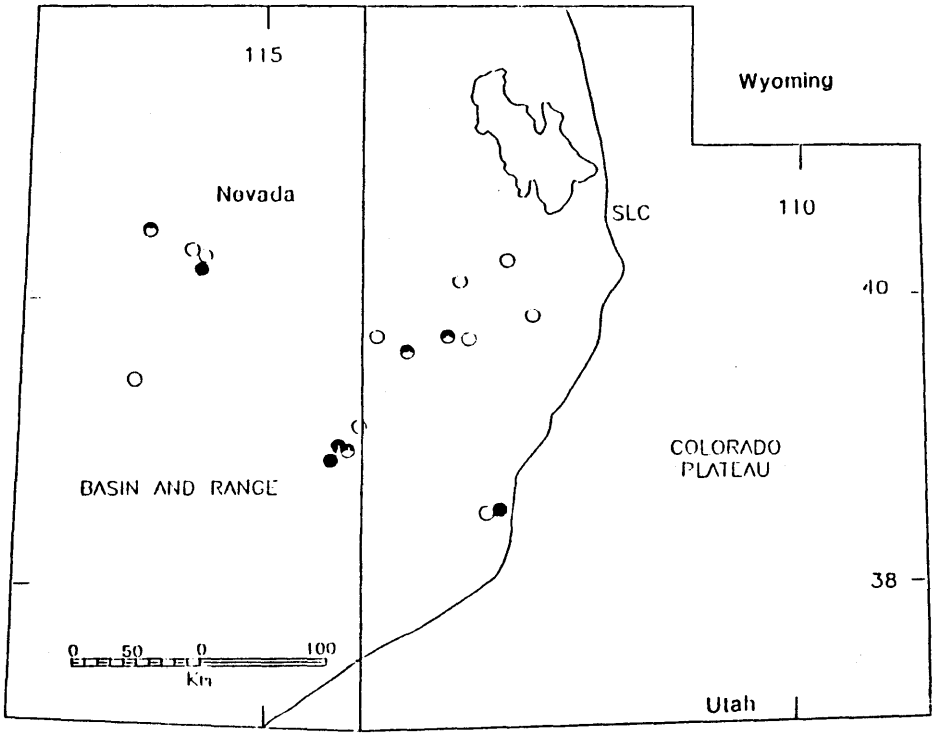
115
Wyoming
Nevada
SLC
110
40
COLORADO
PLATEAU
BASIN AND RANGE
38
0 50 0 100
Km
Utah

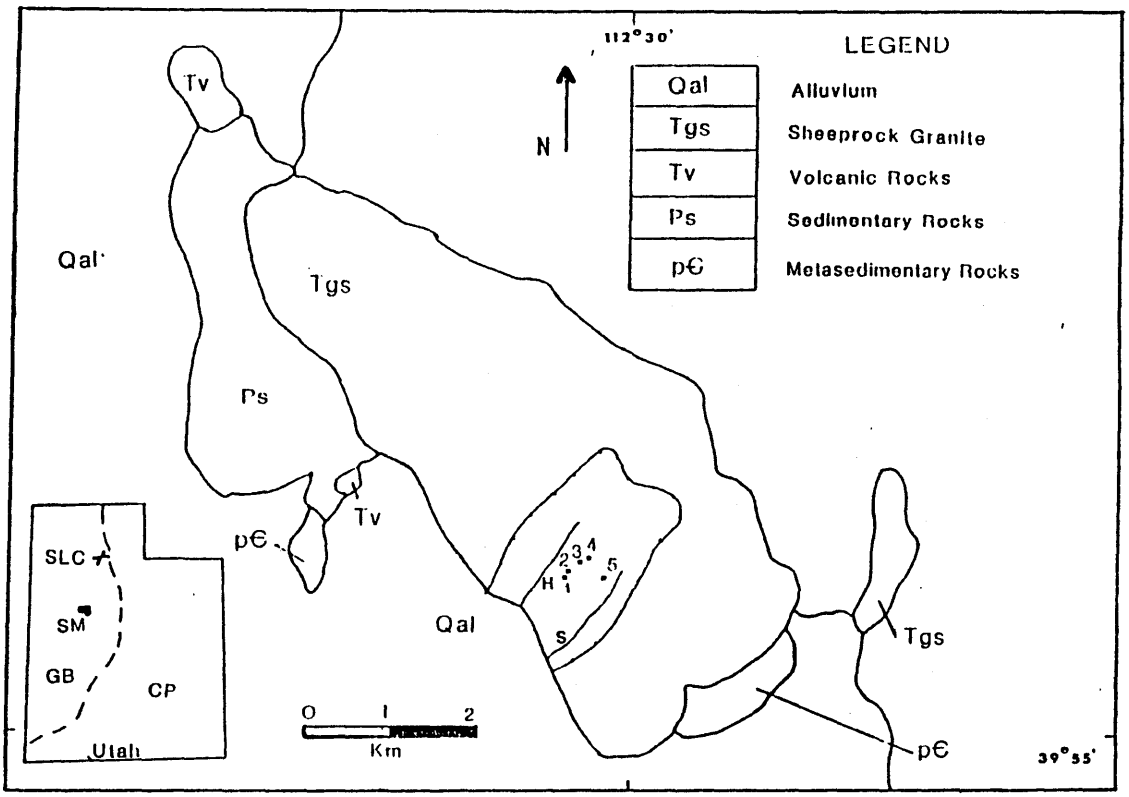
112°30'
LEGEND
Qal
Alluvium
Tgs
Sheeprock Granite
Tv
Volcanic Rocks
Ps
Sedimentary Rocks
pЄ
Metasedimentary Rocks
N
Tv
Qal
Tgs
Ps
Tv
pЄ
Qal
Tgs
pЄ
1
2
3
4
5
H
S
SLC
SM
GB
CP
Utah
0
1
2
Km
39°55'

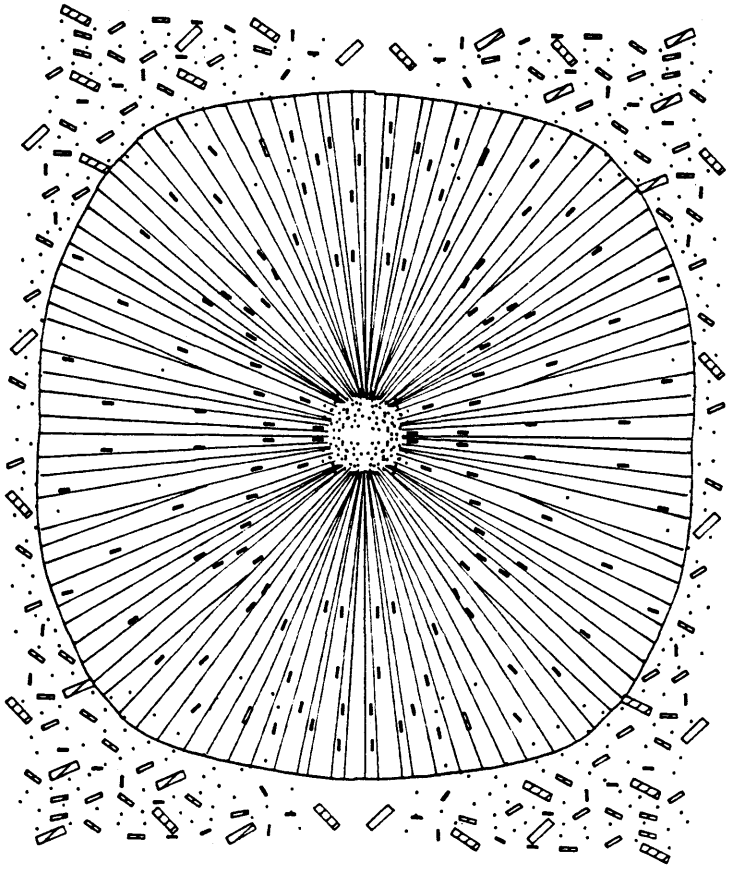

a
b
DNAG
CM
IN
mm

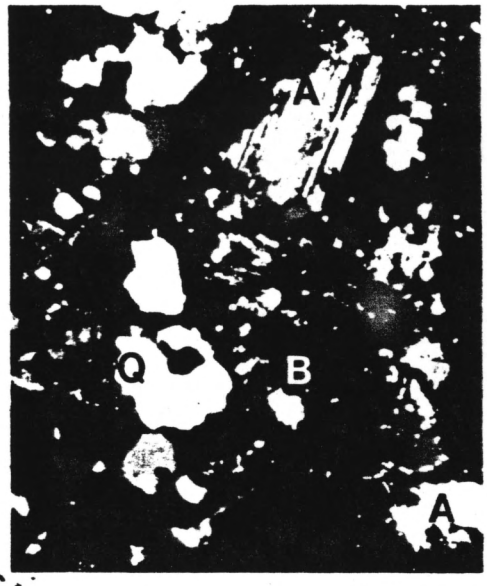

c

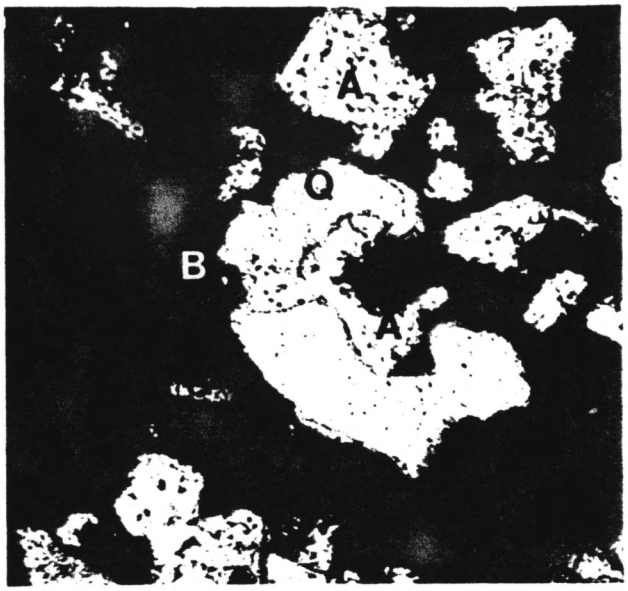

d

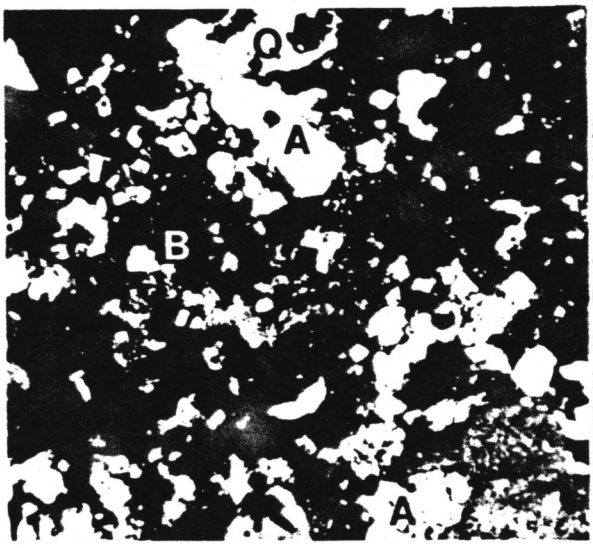

e

f

g

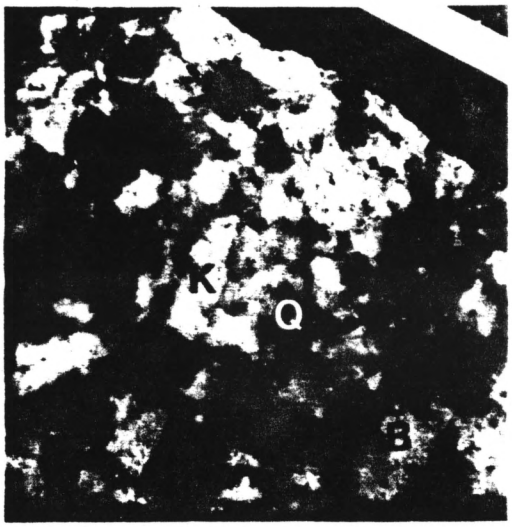

h

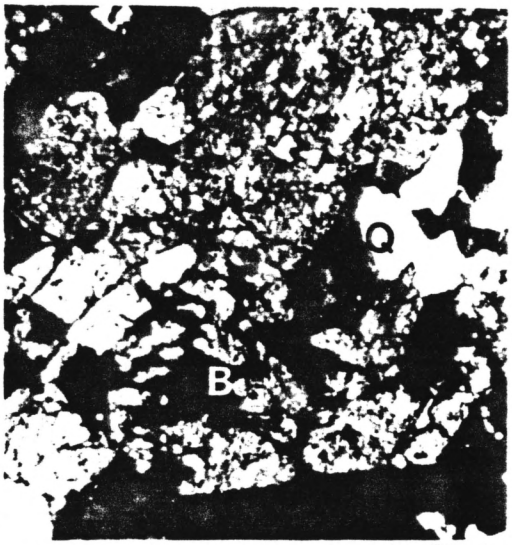

i

j

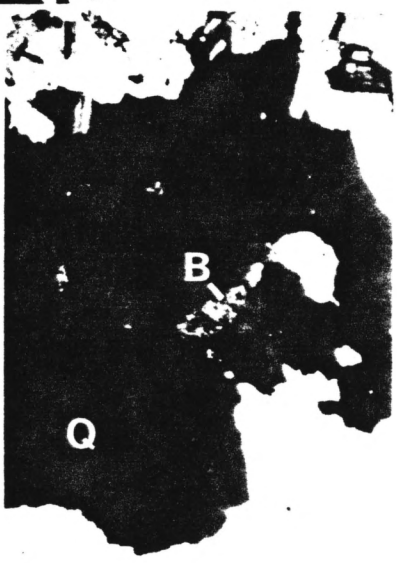

k

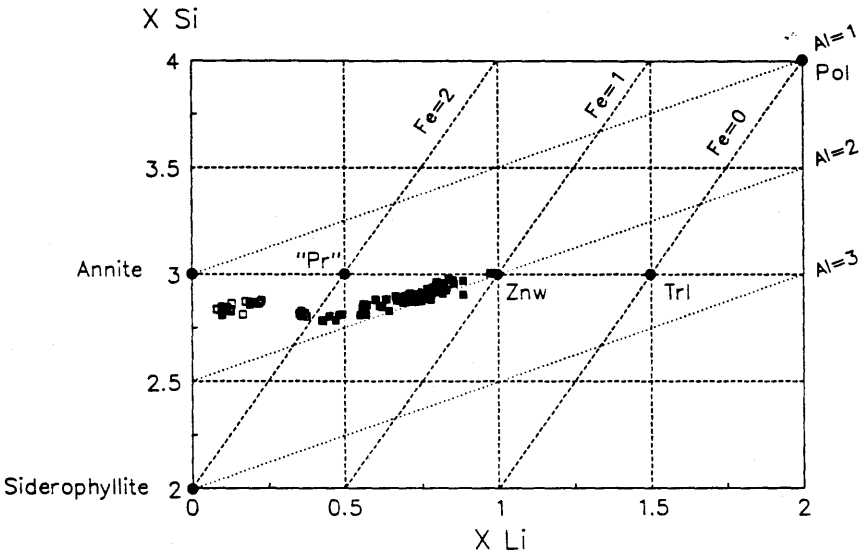
X Si
4
3.5
3
2.5
2
Annite
Siderophyllite
0
0.5
1
1.5
2
X Li
Al=1
Pol
Al=2
Al=3
Fe=2
Fe=1
Fe=0
"Pr"
Znw
Trl

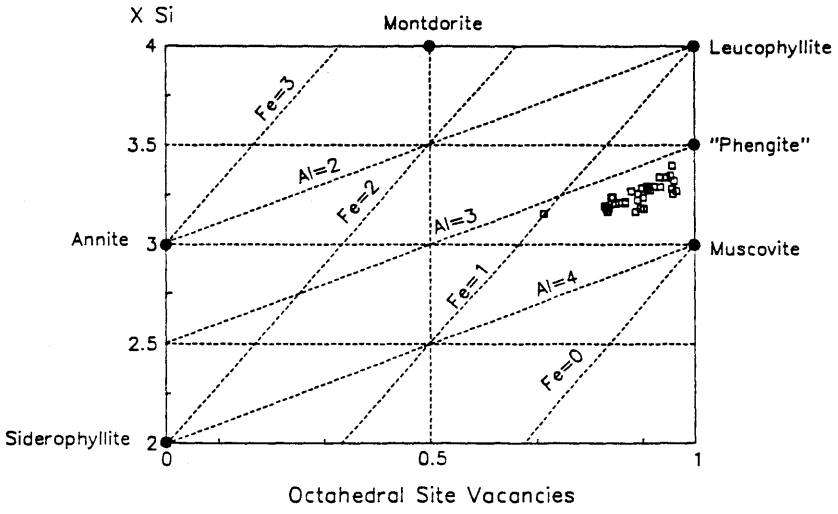
X Si
Montdorite
Leucophyllite
"Phengite"
Muscovite
Annite
Siderophyllite
4
3.5
3
2.5
2
0
0.5
1
Fe=3
Al=2
Fe=2
Al=3
Fe=1
Al=4
Fe=0
Octahedral Site Vacancies

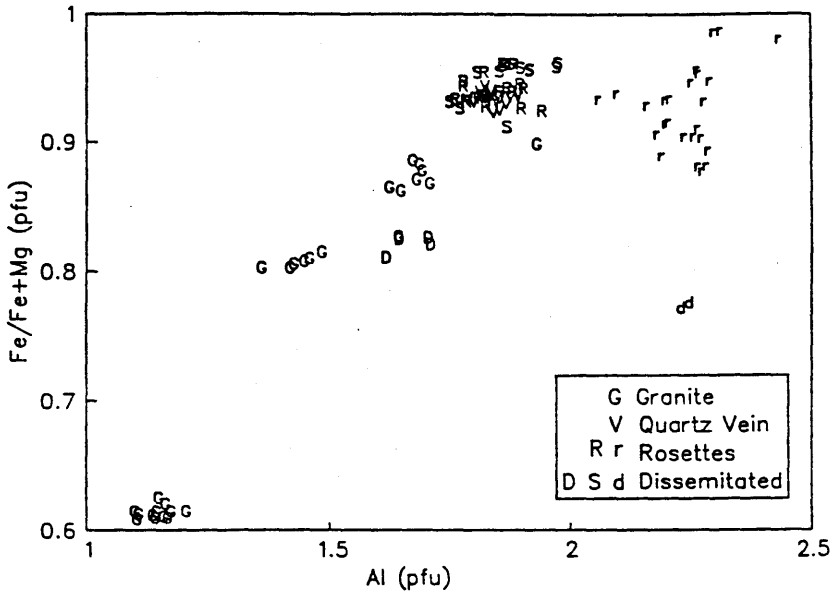
1
0.9
0.8
0.7
0.6
Fe/Fe+Mg (pfu)
1
1.5
2
2.5
Al (pfu)
G Granite
V Quartz Vein
R r Rosettes
D S d Dissemitated

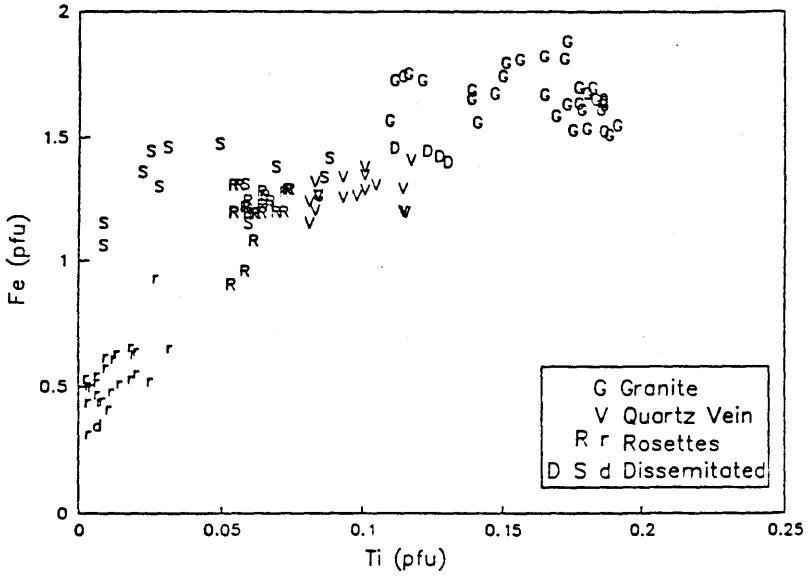
Fe (pfu)
Ti (pfu)
0
0.5
1
1.5
2
0.05
0.1
0.15
0.2
0.25
G Granite
V Quartz Vein
R r Rosettes
D S d Dissemitated

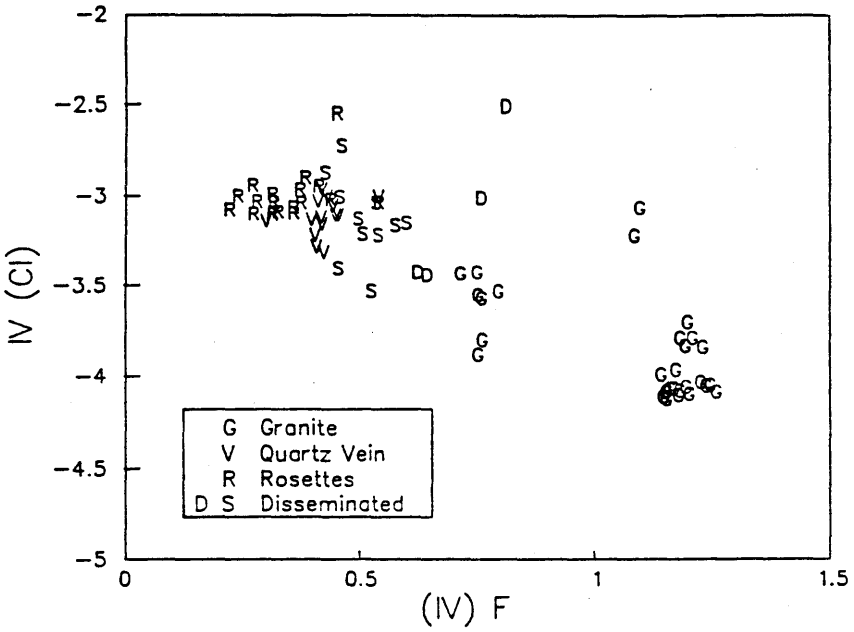
−2
−2.5
−3
−3.5
−4
−4.5
−5
0
0.5
1
1.5
(IV) F
IV (Cl)
G Granite
V Quartz Vein
R Rosettes
D S Disseminated

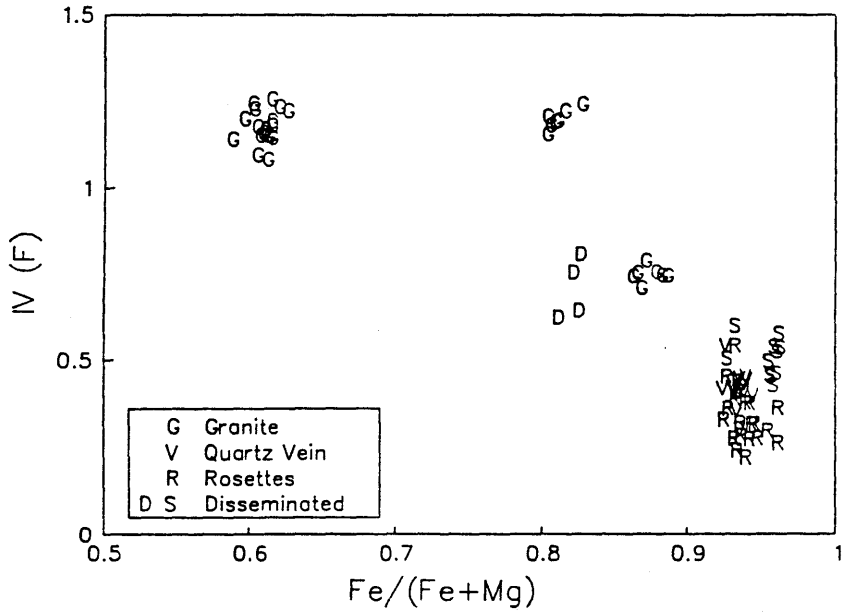
1.5
1
0.5
0
IV (F)
0.5
0.6
0.7
0.8
0.9
1
Fe/(Fe+Mg)
G Granite
V Quartz Vein
R Rosettes
D S Disseminated

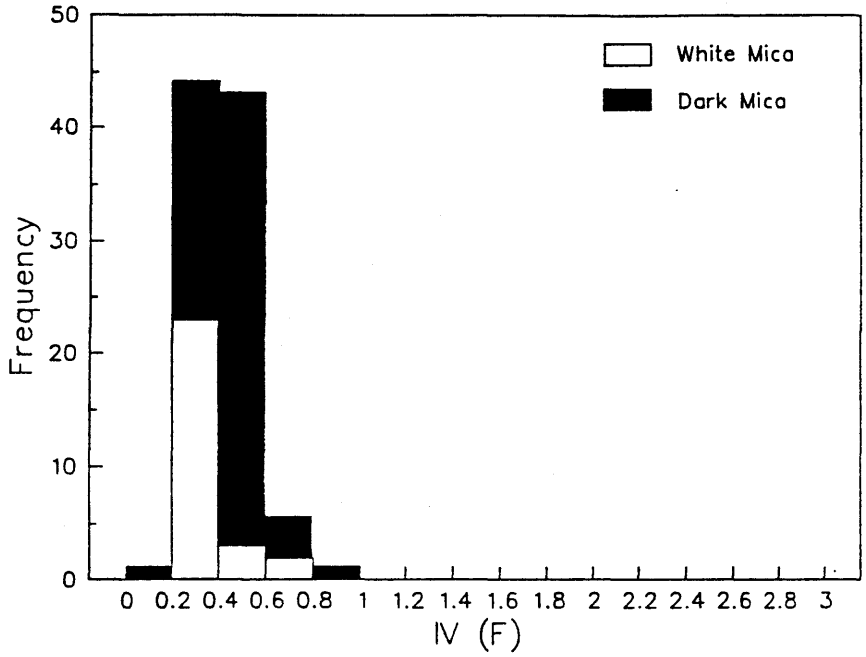
50
40
30
20
10
0
Frequency
White Mica
Dark Mica
0 0.2 0.4 0.6 0.8 1 1.2 1.4 1.6 1.8 2 2.2 2.4 2.6 2.8 3
IV (F)

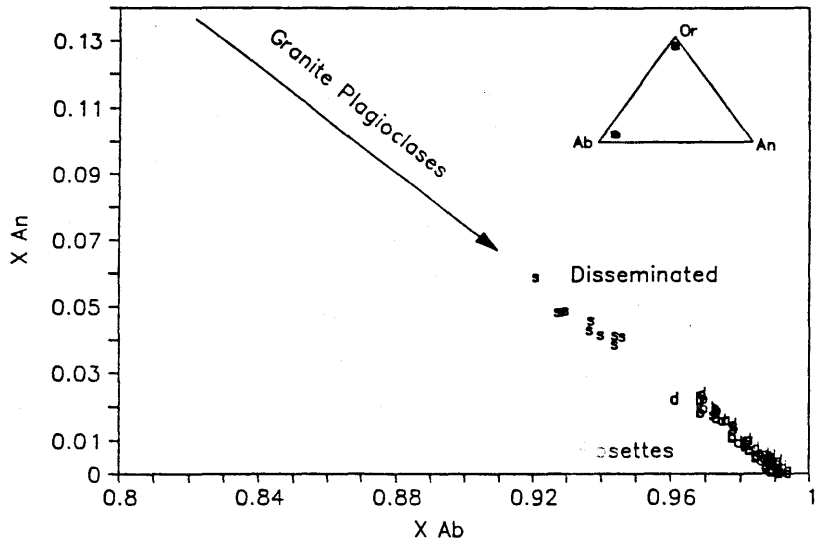
Granite Plagioclases
Or
Ab
An
Disseminated
X An
X Ab
0.13
0.11
0.09
0.07
0.05
0.03
0.01
0
0.8
0.84
0.88
0.92
0.96
1

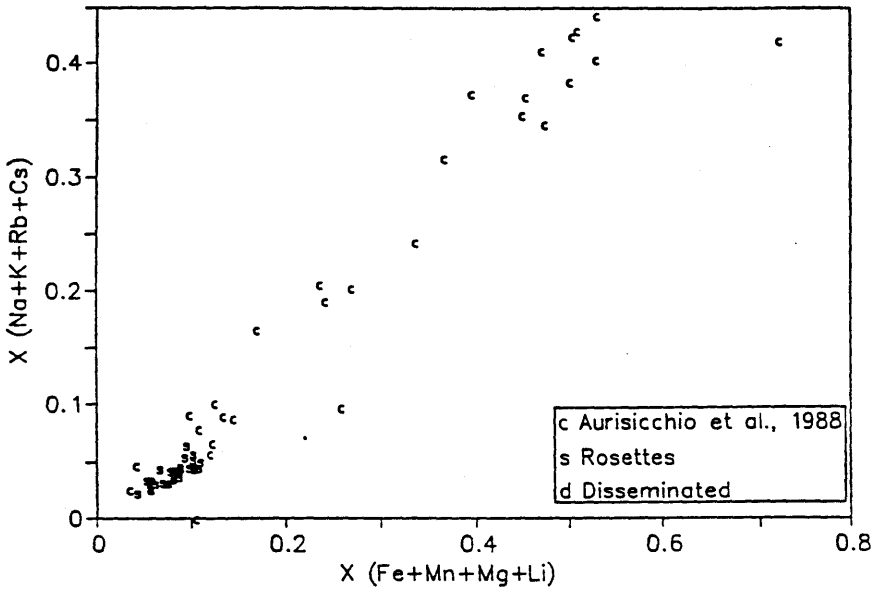
0.4
0.3
0.2
0.1
0
X (Na+K+Rb+Cs)
0
0.2
0.4
0.6
0.8
X (Fe+Mn+Mg+Li)
c Aurisicchio et al., 1988
s Rosettes
d Disseminated

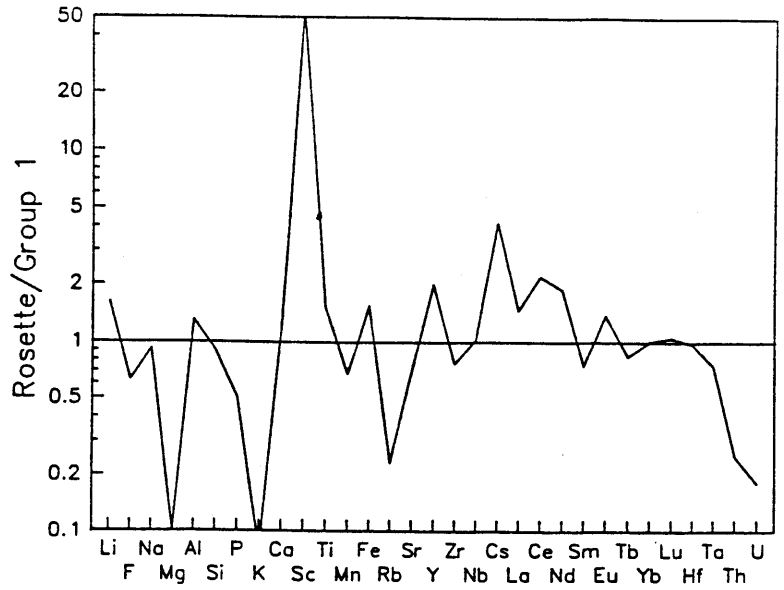
Rosette/Group 1
50
20
10
5
2
1
0.5
0.2
0.1
Li Na Al P Ca Ti Fe Sr Zr Cs Ce Sm Tb Lu Ta U
F Mg Si K Sc Mn Rb Y Nb La Nd Eu Yb Hf Th

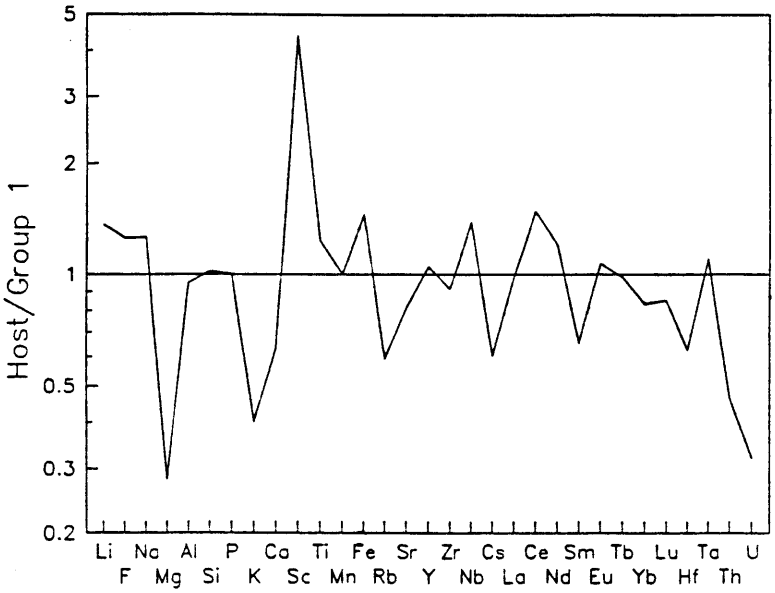
Host/Group 1
5
3
2
1
0.5
0.3
0.2
Li Na Al P Ca Ti Fe Sr Zr Cs Ce Sm Tb Lu Ta U
F Mg Si K Sc Mn Rb Y Nb La Nd Eu Yb Hf Th

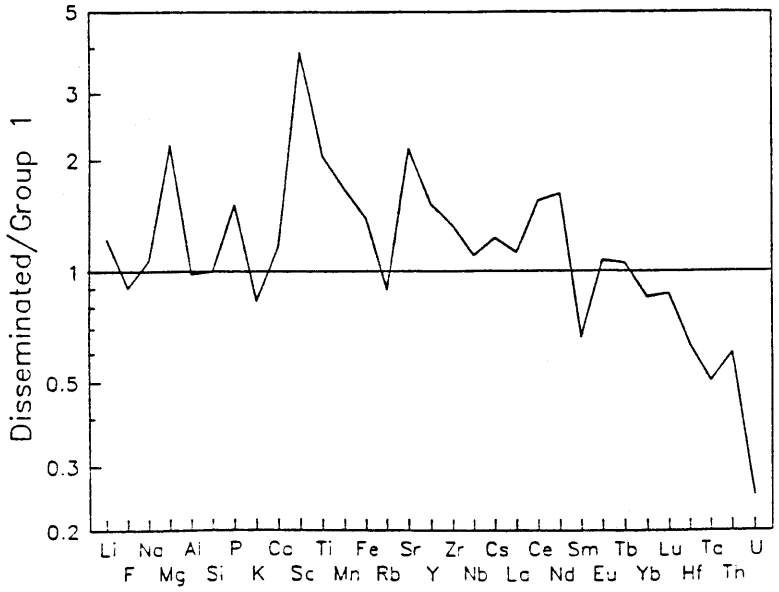
Disseminated/Group 1
5
3
2
1
0.5
0.3
0.2
Li Na Al P Ca Ti Fe Sr Zr Cs Ce Sm Tb Lu Tc U
F Mg Si K Sc Mn Rb Y Nb La Nd Eu Yb Hf Th

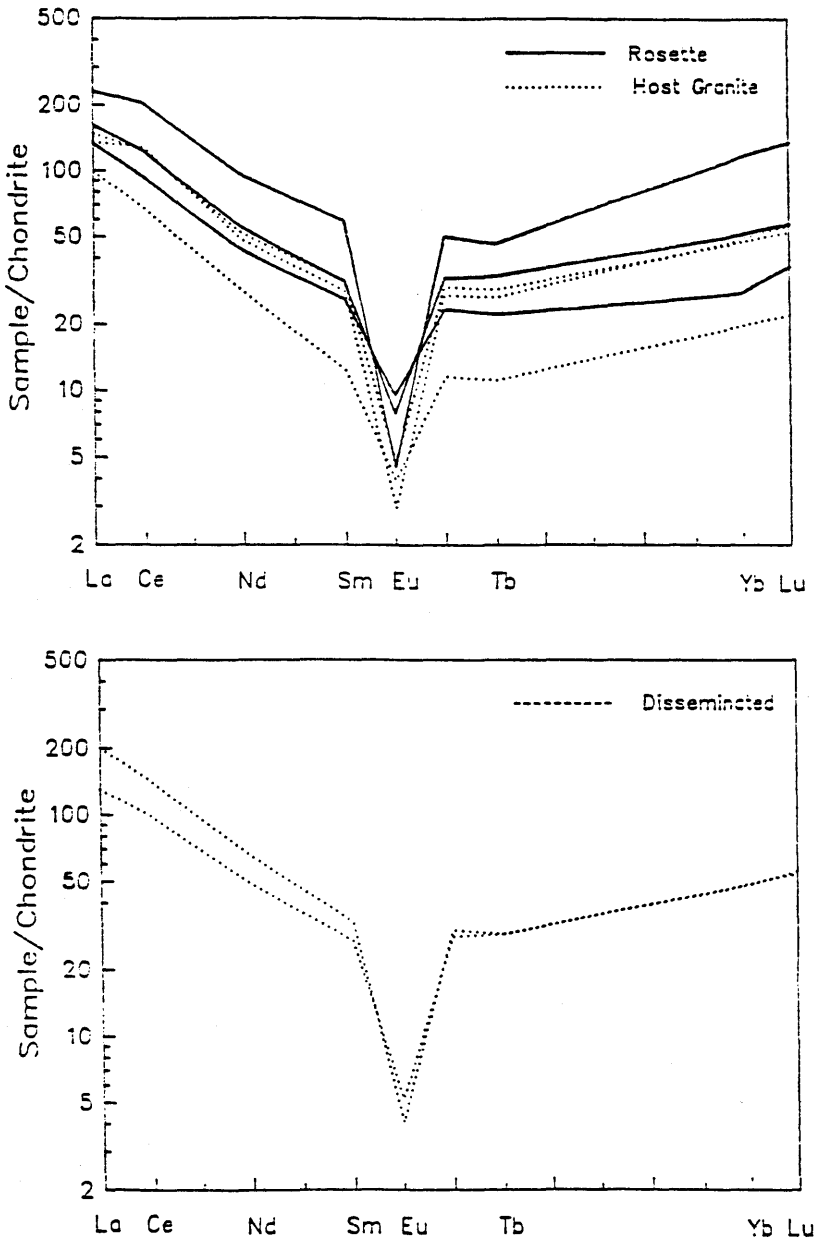
Rosette
Host Granite
Disseminated
Sample/Chondrite
500
200
100
50
20
10
5
2
La
Ce
Nd
Sm
Eu
Tb
Yb
Lu

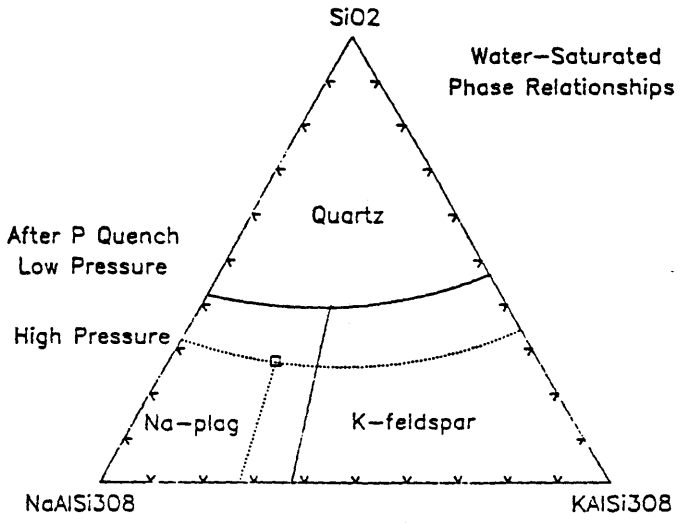
SiO2
Water–Saturated
Phase Relationships
Quartz
After P Quench
Low Pressure
High Pressure
Na–plag
K–feldspar
NaAlSi3O8
KAlSi3O8

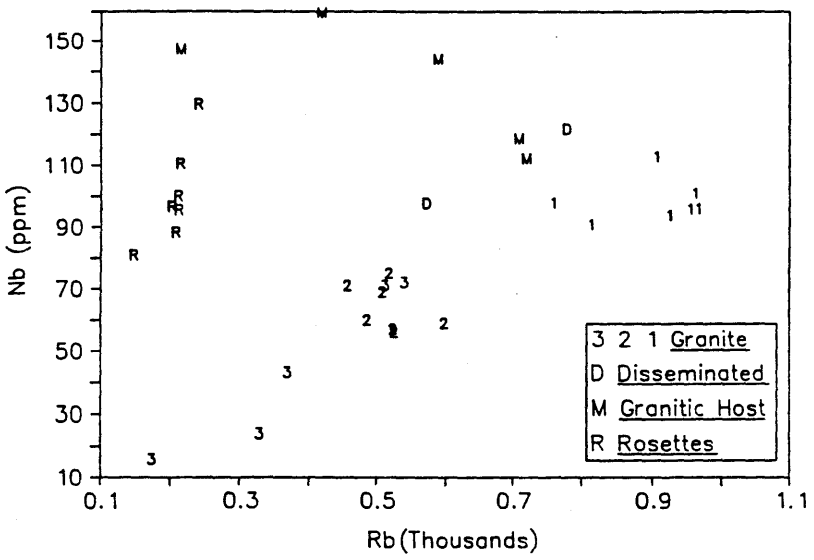
Nb (ppm)
150
130
110
90
70
50
30
10
0.1
0.3
0.5
0.7
0.9
1.1
Rb (Thousands)
3 2 1 Granite
D Disseminated
M Granitic Host
R Rosettes

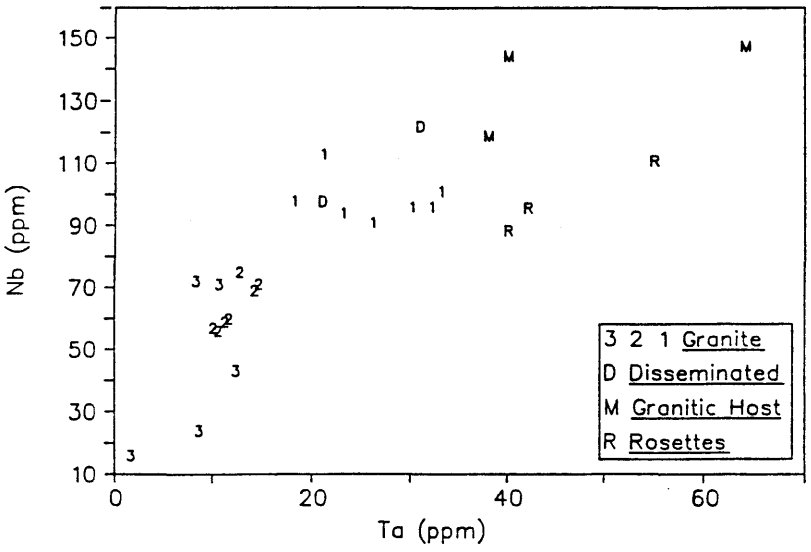
Nb (ppm)
Ta (ppm)
150
130
110
90
70
50
30
10
0
20
40
60
3 2 1 Granite
D Disseminated
M Granitic Host
R Rosettes

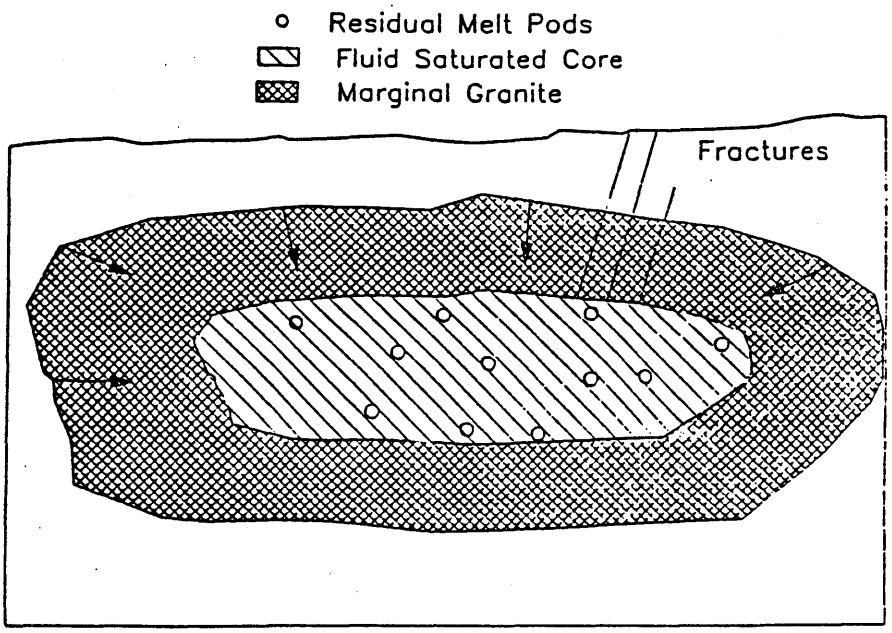
Residual Melt Pods
Fluid Saturated Core
Marginal Granite
Fractures

Table 1. Modal compositions of rocks from the Sheeprock granite.

Minerals	Rosettes	Matrix	Dissem
Quartz	6	45	40
Albite	27	30	17
K feldspar	0	17	30
Muscovite	1.5	1	0.5
Dark Mica	0.5	3	7
Fluorite	1.5	0.8	0.1
Beryl	63	2	4
Oxides	0.5	1	1

Table 2. Representative mica analyses from the granite of Sheeprock Mountains.

	r	r	r	r	r	r	r	r	r	r	r	r	r	x	x	R	R	R	R	R	R	R	R
Sample No.	M2C2R	M2C2R	M2C2R	M2C2R	M2C2R	M2C2R	M2C2R	M2C2R	M2C2R	M2C2R	M2C2R	M2C2R	M2C2R	DMBC3M	DMBC3M	M2C2R	M2C2R	M2C2R	M2C2R	M2C2R	M2C2R	M2C2R	M2C2R
SiO2	43.84	45.50	43.39	46.68	45.78	46.55	45.24	46.21	47.31	44.16	44.87	44.79	47.73	48.44	38.99	39.08	38.82	39.01	39.45	39.36	39.11	39.28
TiO2	0.32	0.17	0.58	0.19	0.10	0.06	0.38	0.26	0.14	0.15	0.23	0.34	0.02	0.12	1.14	1.03	1.13	1.15	1.08	1.05	1.03	1.28
Al2O3	26.33	25.77	25.42	26.67	26.01	27.35	27.07	27.17	27.70	26.47	25.97	27.02	27.27	27.38	21.09	20.45	19.89	19.96	20.67	20.98	21.39	21.32
FeO(t)	10.84	9.63	10.63	6.92	9.09	7.43	9.31	8.71	7.60	10.21	10.48	8.87	6.09	6.04	19.56	18.86	20.17	19.98	18.96	19.94	19.50	19.21
MnO	0.35	0.41	0.43	0.24	0.45	0.40	0.39	0.28	0.27	0.46	0.41	0.36	0.15	0.17	1.00	0.90	0.84	0.79	0.81	0.79	0.81	0.77
MgO	0.34	0.55	0.55	0.41	0.36	0.30	0.70	0.51	0.45	0.26	0.42	0.66	0.99	1.00	0.45	0.50	0.64	0.68	0.84	0.82	0.71	0.66
Li2O	-	-	-	-	-	-	-	-	-	-	-	-	-	-	2.70	2.80	2.60	2.65	2.70	2.60	2.65	2.70
Na2O	0.10	0.12	0.14	0.13	0.12	0.16	0.16	0.13	0.13	0.19	0.17	0.18	0.11	0.13	0.12	0.12	0.20	0.19	0.18	0.20	0.18	0.17
K2O	10.61	10.74	10.25	10.87	10.77	10.72	10.43	10.63	10.65	10.36	10.15	10.46	10.50	10.63	9.87	9.96	9.67	9.73	9.55	9.44	9.63	9.63
Rb2O	0.43	0.43	0.43	0.43	0.43	0.43	0.43	0.43	0.43	0.43	0.43	0.43	0.43	0.43	0.55	0.55	0.55	0.55	0.55	0.55	0.55	0.55
F	3.14	3.19	3.17	2.70	3.42	2.90	3.05	3.00	2.96	3.28	2.77	3.22	1.56	1.78	4.21	4.05	4.17	4.01	3.85	3.73	3.72	3.73
Cl	0.05	-	0.02	0.01	0.01	-	0.03	-	-	0.02	0.06	0.02	-	-	0.08	0.07	0.08	0.07	0.08	0.08	0.07	0.08
Sum	95.02	95.16	93.67	94.11	95.10	95.10	95.90	96.08	96.40	94.62	94.79	94.99	94.20	95.37	97.97	96.66	96.99	97.07	97.08	97.96	97.76	97.81
H2O*	2.63	2.66	2.56	2.93	2.55	2.87	2.77	2.83	2.90	2.57	2.83	2.65	3.55	3.49	1.99	2.02	1.95	2.04	2.15	2.23	2.23	2.24
Total	97.65	97.82	96.23	97.04	97.65	97.97	98.67	98.91	99.31	97.19	97.61	97.64	97.75	98.86	99.96	98.69	98.94	99.11	99.23	100.19	100.00	100.04
Normalized to 11 Oxygens																						
Si	3.181	3.268	3.193	3.321	3.283	3.288	3.210	3.254	3.291	3.204	3.236	3.208	3.337	3.347	2.920	2.956	2.949	2.953	2.957	2.934	2.917	2.923
Al(vi)	0.819	0.732	0.807	0.679	0.717	0.712	0.790	0.746	0.709	0.796	0.764	0.792	0.663	0.653	1.080	1.044	1.051	1.047	1.043	1.066	1.083	1.077
Al(vi)	1.433	1.450	1.398	1.558	1.482	1.566	1.475	1.510	1.563	1.468	1.444	1.490	1.584	1.577	0.782	0.780	0.730	0.734	0.784	0.777	0.798	0.793
Ti	0.018	0.009	0.032	0.010	0.006	0.003	0.020	0.014	0.007	0.009	0.013	0.018	0.001	0.006	0.064	0.059	0.064	0.065	0.061	0.059	0.058	0.072
Fe(t)	0.658	0.578	0.654	0.412	0.545	0.439	0.553	0.513	0.442	0.619	0.632	0.531	0.356	0.349	1.225	1.193	1.281	1.264	1.189	1.243	1.216	1.196
Mn	0.022	0.025	0.027	0.015	0.028	0.024	0.023	0.017	0.016	0.028	0.025	0.022	0.009	0.010	0.063	0.058	0.054	0.051	0.051	0.050	0.052	0.048
Mg	0.037	0.059	0.060	0.043	0.039	0.032	0.074	0.054	0.047	0.028	0.045	0.071	0.103	0.103	0.050	0.057	0.072	0.077	0.094	0.091	0.079	0.073
Li	-	-	-	-	-	-	-	-	-	-	-	-	-	-	0.814	0.852	0.794	0.807	0.814	0.779	0.795	0.809
Na	0.014	0.016	0.019	0.017	0.016	0.022	0.022	0.018	0.018	0.027	0.024	0.026	0.014	0.017	0.018	0.017	0.030	0.027	0.025	0.029	0.026	0.025
K	0.982	0.984	0.962	0.987	0.986	0.966	0.944	0.955	0.946	0.959	0.934	0.956	0.937	0.938	0.943	0.961	0.937	0.940	0.914	0.898	0.916	0.915
Rb	0.020	0.020	0.020	0.020	0.020	0.020	0.020	0.019	0.019	0.020	0.020	0.020	0.019	0.019	0.026	0.026	0.026	0.026	0.026	0.026	0.026	0.026
F	0.721	0.724	0.739	0.608	0.777	0.647	0.684	0.668	0.652	0.752	0.632	0.730	0.344	0.389	0.997	0.969	1.002	0.961	0.914	0.879	0.878	0.879
Cl	0.007	-	-	-	-	-	-	-	-	-	0.007	-	-	-	0.010	0.009	0.011	0.009	0.010	0.010	0.009	0.010
OH*	1.272	1.276	1.259	1.391	1.222	1.353	1.313	1.332	1.348	1.246	1.361	1.268	1.656	1.611	0.993	1.022	0.987	1.030	1.076	1.111	1.113	1.111
Log F/Cl	2.01	-	2.57	2.78	2.89	-	2.36	-	-	2.58	1.96	2.56	-	-	2.00	2.03	1.96	2.03	1.96	1.94	1.99	1.94
Log F/OH	-0.25	-0.25	-0.23	-0.36	-0.20	-0.32	-0.28	-0.30	-0.32	-0.22	-0.33	-0.24	-0.68	-0.62	0.00	-0.02	0.01	-0.03	-0.07	-0.10	-0.10	-0.10
IV(F)	0.34	0.33	0.34	0.40	0.26	0.36	0.38	0.37	0.36	0.29	0.42	0.33	0.75	0.68	0.26	0.29	0.27	0.31	0.36	0.38	0.37	0.37
IV(Cl)	-	-	-	-	-	-	-	-	-	-	-	-	-	-	-3.05	-2.99	-3.10	-3.00	-3.04	-3.02	-2.97	-3.01
IV(F/Cl)	-	-	-	-	-	-	-	-	-	-	-	-	-	-	3.31	3.29	3.38	3.32	3.40	3.41	3.34	3.38

r=ferrimuscovites analyzed from rosettes.
d=ferrimuscovites analyzed from granite containing disseminated beryl from DHBC.
R=zinnwaldites analyzed from rosettes.
D&S=zinnwaldites analyzed from granite containing disseminated beryl (D=DHBC, S=SRC).
H2O*, and OH* were calculated on basis of 4(OH+F+Cl) per formula unit.
-=concentrations were to low to be detected.
Li2O was not analyzed but calculated to dark micas based on the assumption of full (vi) site occupancy.

	R	R	D	D	D	S	S	S	V	V	V	V	V	V	V	V
Sample No.	HBC2R	HBC2R	DHBC3M	DHBC3M	DHBC3M	SDC2D	SDC2D	SDC2D	HBCV1	HBCV1	HBCV1	HBCV1	HBCV1	HBCV1	HBCV1	HBCV1
SiO2	38.00	38.16	36.72	36.81	37.11	38.84	37.32	38.21	37.61	38.08	38.07	38.07	38.67	37.95	38.69	38.05
TiO2	0.95	0.99	2.27	1.91	2.21	0.49	0.85	1.02	1.62	1.78	1.77	1.48	1.79	2.02	1.43	1.42
Al2O3	21.23	21.45	18.97	17.98	17.85	21.75	20.68	20.69	20.99	20.08	20.39	20.73	20.34	20.41	21.33	20.96
FeO(t)	20.63	20.78	21.92	22.47	22.17	20.84	23.08	20.62	19.66	21.84	21.39	19.97	20.50	20.37	18.30	19.50
MnO	0.83	0.87	0.94	0.80	1.01	1.13	1.27	1.08	0.78	1.08	0.99	0.93	0.91	0.85	0.85	0.92
MgO	0.67	0.71	2.67	2.68	2.89	0.54	0.55	0.55	0.73	0.88	0.77	0.80	0.86	0.68	0.71	0.76
Li2O	2.40	2.40	1.85	1.80	1.85	2.40	2.00	2.41	2.40	2.20	2.30	2.45	2.45	2.45	2.70	2.50
Na2O	0.16	0.17	0.16	0.23	0.19	0.12	0.11	0.22	0.19	0.16	0.13	0.15	0.17	0.15	0.13	0.19
K2O	9.63	9.59	9.58	9.17	9.67	9.70	9.38	9.39	9.13	9.36	9.63	9.53	9.41	9.53	9.73	9.47
Rb2O	0.55	0.55	0.55	0.55	0.55	0.55	0.55	0.55	0.55	0.55	0.55	0.55	0.55	0.55	0.55	0.55
F	3.93	4.16	2.41	2.89	3.05	3.29	2.90	3.26	3.36	3.40	3.33	3.54	3.62	3.57	4.05	3.33
Cl	0.09	0.08	0.18	0.15	0.19	0.09	0.15	0.06	0.10	0.15	0.13	0.09	0.10	0.10	0.07	0.09
Sum	97.41	98.13	97.16	96.21	97.43	98.34	97.59	96.68	95.69	98.11	98.02	96.78	97.82	97.10	96.83	96.32
H2O*	2.08	1.99	2.72	2.45	2.40	2.43	2.51	2.38	2.30	2.31	2.35	2.25	2.24	2.23	2.04	2.34
Total	99.48	100.12	99.88	98.66	99.83	100.77	100.10	99.06	97.99	100.42	100.37	99.03	100.07	99.34	98.87	98.66
Si	2.878	2.871	2.811	2.859	2.853	2.899	2.851	2.904	2.877	2.881	2.875	2.891	2.908	2.880	2.913	2.891
Al(vi)	1.122	1.129	1.189	1.141	1.147	1.101	1.149	1.096	1.123	1.119	1.125	1.109	1.092	1.120	1.087	1.109
Al(vi)	0.774	0.774	0.523	0.505	0.472	0.813	0.714	0.758	0.770	0.672	0.691	0.747	0.711	0.706	0.806	0.768
Ti	0.054	0.056	0.131	0.112	0.128	0.028	0.049	0.058	0.093	0.101	0.101	0.084	0.101	0.115	0.081	0.081
Fe(t)	1.307	1.307	1.403	1.459	1.425	1.301	1.475	1.311	1.258	1.382	1.351	1.268	1.289	1.293	1.152	1.239
Mn	0.053	0.055	0.061	0.052	0.066	0.071	0.082	0.070	0.051	0.069	0.064	0.060	0.058	0.055	0.054	0.059
Mg	0.076	0.080	0.305	0.310	0.332	0.060	0.062	0.062	0.083	0.099	0.087	0.090	0.096	0.077	0.080	0.086
Li	0.731	0.726	0.570	0.562	0.572	0.720	0.614	0.737	0.738	0.669	0.699	0.748	0.741	0.748	0.818	0.764
Na	0.025	0.024	0.024	0.035	0.029	0.017	0.016	0.032	0.028	0.024	0.019	0.022	0.024	0.022	0.019	0.028
K	0.931	0.921	0.936	0.909	0.948	0.924	0.914	0.911	0.891	0.904	0.928	0.924	0.903	0.923	0.935	0.918
Rb	0.026	0.026	0.027	0.027	0.027	0.026	0.027	0.026								
F	0.940	0.990	0.585	0.710	0.743	0.778	0.700	0.784	0.813	0.814	0.796	0.850	0.861	0.857	0.965	0.800
Cl	0.011	0.011	0.023	0.020	0.025	0.011	0.019	0.008	0.013	0.019	0.017	0.011	0.013	0.013	0.009	0.011
OH*	1.049	0.999	1.392	1.270	1.232	1.211	1.281	1.208	1.174	1.167	1.187	1.139	1.126	1.130	1.026	1.189
Log F/Cl	1.93	1.95	1.41	1.55	1.47	1.85	1.57	1.99	1.80	1.63	1.67	1.89	1.82	1.82	2.03	1.86
Log F/OH	-0.05	-0.00	-0.38	-0.25	-0.22	-0.19	-0.26	-0.19	-0.16	-0.16	-0.17	-0.13	-0.12	-0.12	-0.03	-0.17
IV(F)	0.31	0.27	0.76	0.64	0.62	0.45	0.52	0.46	0.43	0.44	0.45	0.40	0.40	0.39	0.30	0.45
IV(Cl)	-3.08	-3.10	-3.43	-3.41	-3.53	-3.01	-3.22	-2.87	-3.11	-3.29	-3.22	-3.05	-3.13	-3.12	-3.01	-3.03
IV(F/Cl)	3.39	3.38	4.18	4.05	4.16	3.46	3.75	3.33	3.54	3.73	3.68	3.46	3.54	3.52	3.30	3.48

Table 3. Typical microprobe analyses of feldspars from the Sheeprock granite

	v	v	v	r	r	r	r	r	r	r	r	r	r	D	D	D	D	D	D	D
Sample No.	HBCV	HBCV	HBCV	HBC2B	HBC2B	HBC2B	HBC2B	HBC2B	HBC2B	HBC2B	HBC2B	HBC2B	HBC2A	DHBC3M	DHBC3M	DHBC3M	DHBC3M	DHBC3M	DHBC3M	DHBC3M
SiO2	67.61	68.47	68.31	69.14	68.01	67.88	69.18	68.56	68.99	68.30	68.86	69.19	68.69	68.69	69.04	69.08	68.81	65.22	65.45	65.31
Al2O3	20.10	19.78	19.97	19.51	19.46	19.00	18.87	19.82	19.46	19.78	19.48	19.29	19.60	19.54	19.34	19.49	19.58	18.16	18.30	18.21
Fe2O3	0.01	-	-	0.07	-	0.03	-	-	-	0.01	-	0.03	0.03	0.03	0.01	0.01	0.02	0.06	0.07	0.01
CaO	0.39	0.16	0.25	0.12	0.04	0.24	0.11	0.48	0.02	0.39	0.09	0.01	0.35	0.34	0.06	0.18	0.29	-	-	-
Na2O	11.24	11.45	11.41	11.52	11.58	11.38	11.62	11.32	11.62	11.27	11.50	11.44	11.37	11.17	11.52	11.31	11.40	1.00	0.63	0.51
K2O	0.23	0.18	0.19	0.18	0.14	0.20	0.12	0.14	0.12	0.15	0.12	0.11	0.14	0.16	0.14	0.18	0.15	15.51	15.91	16.19
Total	99.57	100.04	100.14	100.54	99.23	98.73	99.90	100.32	100.21	99.90	100.05	100.07	100.18	99.93	100.11	100.25	100.25	99.95	100.36	100.23
Cations of Basis of 8 oxygens																				
Si	2.968	2.988	2.980	3.002	2.993	3.003	3.021	2.985	3.004	2.985	3.002	3.013	2.994	2.999	3.008	3.005	2.996	3.008	3.007	3.009
Al	1.040	1.018	1.027	0.999	1.010	0.991	0.972	1.017	0.999	1.019	1.001	0.990	1.007	1.006	0.993	1.000	1.005	0.987	0.991	0.989
Fe	-	-	-	0.002	-	0.001	-	-	-	-	-	0.001	0.001	0.001	-	-	0.001	0.002	0.002	-
Ca	0.018	0.007	0.012	0.006	0.002	0.011	0.005	0.022	0.001	0.018	0.004	-	0.016	0.016	0.003	0.008	0.014	-	-	-
Na	0.956	0.969	0.965	0.970	0.988	0.976	0.984	0.956	0.981	0.955	0.972	0.966	0.961	0.945	0.973	0.954	0.962	0.089	0.056	0.046
K	0.013	0.010	0.011	0.010	0.008	0.011	0.007	0.008	0.007	0.008	0.007	0.006	0.008	0.009	0.008	0.010	0.008	0.912	0.933	0.951
Ab	0.9685	0.9822	0.9773	0.9842	0.9902	0.9773	0.9881	0.9694	0.9923	0.9729	0.9889	0.9932	0.9755	0.9744	0.9892	0.9811	0.9778	0.0892	0.0568	0.0457
An	0.0187	0.0075	0.0118	0.0057	0.0019	0.0114	0.0052	0.0227	0.0009	0.0186	0.0043	0.0005	0.0166	0.0164	0.0028	0.0086	0.0137	-	-	-
Or	0.0128	0.0102	0.0109	0.0101	0.0079	0.0113	0.0067	0.0079	0.0067	0.0085	0.0068	0.0063	0.0079	0.0092	0.0079	0.0103	0.0085	0.9108	0.9432	0.9543

Table 4 Microprobe Analyses Of Beryl Crystals from the Sheeprock Mountains

	r	r	r	r	r	r	r	r	r	r	r	r	r	r	r	d	d	d	d	d	v	v	v
	HBC2R	HBC2R	HBC2R	HBC2R	HBC2R	HBC2R	HBC2R	HBC2R	HBC2R	HBC2R	HBC2R	HBC2R	HBC2R	HBC2R	HBC2R	DHBC3	DHBC3	DHBC3	DHBC3	DHBC3	HBCV1	HBCV1	HBCV1
SiO2	65.45	66.24	65.98	66.49	66.01	65.98	65.44	65.09	66.07	66.03	65.64	65.37	65.93	66.11	65.3	66.4	65.93	64.88	65.31	65.62	65	65.13	65.13
Al2O3	17.88	18.2	17.82	18.06	18.17	17.96	17.82	17.94	18.21	18.04	17.76	18.12	17.75	18.02	17.82	18.36	18.31	17.6	17.48	17.87	17.84	17.82	18.1
FeO	0.96	0.751	1.24	0.881	0.9	1.01	1.27	0.93	0.62	1.05	1.32	0.87	1.39	1.08	0.85	0.64	0.55	1.18	1.1	1.01	0.95	1.03	0.69
MnO	0.03	-	-	0.01	0.04	-	0.02	0.02	0.03	-	0.02	-	-	-	-	-	0.02	0.01	-	0.01	0.03	0.01	0.01
MgO	0.02	0.02	0.05	0.02	0.02	0.02	0.02	0.02	0.03	0.02	0.03	0.01	0.02	0.04	-	0.06	0.05	0.07	0.07	0.05	0.03	0.04	0.01
Na2O	0.23	0.17	0.23	0.161	0.16	0.17	0.21	0.21	0.18	0.22	0.233	0.15	0.26	0.23	0.22	0.17	0.17	0.26	0.33	0.2	0.17	0.17	0.1
K2O	-	0.01	0.01	-	-	0.01	0.02	0.02	-	0.02	0.01	0.02	0.01	0.01	0.01	0.01	0.02	0.01	0.02	0.03	0.02	0.02	0.01
Cs2O	0.01	0.02	0.01	0.02	0.05	0.02	0.05	0.05	-	0.03	0.02	0.03	0.06	0.07	0.03	0.03	-	0.08	0.04	0.01	0.04	0.03	0.07
Rb2O	0.05	0.02	0.08	0.06	0.03	0.06	0.07	0.01	0.06	0.06	0.04	0.06	0.04	0.05	0.06	0.07	0.05	0.03	0.04	0.06	0.07	0.09	0.06
BeO	13.62	13.78	13.73	13.8	13.74	13.72	13.64	13.57	13.74	13.74	13.67	13.64	13.72	13.76	13.58	13.82	13.74	13.52	13.58	13.66	13.55	13.58	13.57
Sum	98.25	99.21	99.15	99.5	99.12	98.95	98.56	97.86	98.94	99.21	98.74	98.27	99.18	99.37	97.87	99.56	98.84	97.64	97.97	98.52	97.7	97.92	97.75
NORMALIZED TO 18 OXYGEN																							
Si	6.000	6.004	6.004	6.014	5.997	6.006	5.994	5.991	6.003	6.000	6.000	5.990	6.004	5.999	6.007	5.998	5.995	5.998	6.012	6.002	5.996	5.996	5.994
Al t	1.932	1.944	1.911	1.925	1.945	1.927	1.924	1.946	1.950	1.932	1.914	1.957	1.905	1.927	1.932	1.955	1.962	1.918	1.896	1.926	1.939	1.933	1.963
Fe	0.074	0.057	0.095	0.067	0.068	0.077	0.097	0.071	0.047	0.080	0.101	0.067	0.106	0.082	0.065	0.048	0.042	0.091	0.085	0.077	0.073	0.079	0.053
Mn	0.002	-	-	0.001	0.003	-	0.002	0.002	0.002	-	0.002	-	-	-	-	-	0.002	0.001	-	0.001	0.002	0.001	0.001
Mg	0.003	0.003	0.007	0.003	0.003	0.003	0.003	0.003	0.004	0.003	0.004	0.001	0.003	0.005	-	0.008	0.007	0.009	0.009	0.007	0.004	0.006	0.001
Na	0.041	0.029	0.040	0.028	0.028	0.030	0.037	0.038	0.032	0.038	0.042	0.026	0.046	0.040	0.039	0.029	0.030	0.047	0.059	0.035	0.030	0.030	0.018
K	-	0.001	0.001	-	-	0.001	0.002	0.002	-	0.002	0.001	0.002	0.001	0.001	0.001	0.001	0.002	0.001	0.002	0.003	0.002	0.002	0.001
Cs	-	0.001	-	0.001	0.002	0.001	0.002	0.002	-	0.001	0.001	0.001	0.002	0.003	0.001	0.001	-	0.003	0.002	-	0.002	0.001	0.003
Rb	0.003	0.001	0.005	0.003	0.002	0.004	0.004	0.001	0.003	0.003	0.002	0.004	0.002	0.003	0.004	0.004	0.003	0.002	0.002	0.004	0.004	0.005	0.004
Be	2.999	3.000	3.001	2.998	2.998	3.000	3.001	3.000	2.999	2.999	3.001	3.002	3.001	2.999	3.001	2.998	3.001	3.002	3.003	3.001	3.002	3.003	2.999
Sum (vi)	2.011	2.004	2.013	1.996	2.019	2.007	2.026	2.022	2.003	2.015	2.021	2.025	2.014	2.014	1.997	2.011	2.013	2.019	1.990	2.011	2.018	2.019	2.018

Table 5. Whole rock analyses of beryl rosettes and granites from the Sheeprock Mountains.

	R	R	R	R	R	R	R	U	N	U	M	M	I	D	D	M
Sample No.	HBC1R	HBC2R	HBC2DCP	HBC3R	HBC5R	HBC6R	HBC7R	HBC1M	HBC3M	HBC5M	HBC6M	HBC7M	DHBC1R	HBC3M	SC2D	SC2M
SiO2	70.4	68.0	67.0	68.1	70.6	69.2	70.0	85.0	77.5	78.4	77.3	77.2	74.8	78.1	77.0	77.3
TiO2	0.09	0.08	0.08	0.12	0.07	0.11	0.08	0.07	0.09	0.09	0.06	0.06	0.18	0.17	0.09	0.07
Al2O3	15.7	17.0	18.2	17.4	16.4	16.5	15.3	8.1	13.8	14.0	12.9	12.8	13.6	11.7	12.4	12.5
Fe2O3	1.33	1.38	1.53	1.37	1.29	1.44	1.30	0.49	1.98	2.41	0.92	0.77	1.56	1.28	1.28	0.89
MnO	0.01	0.02	0.01	0.02	0.02	0.02	0.02	0.01	0.05	0.05	0.02	0.02	0.05	0.04	0.05	0.05
MgO	0.00	0.00	0.00	0.00	0.00	0.00	0.00	0.00	0.15	0.00	0.00	0.00	0.36	0.32	0.26	0.02
CaO	0.80	0.70	0.38	0.20	0.19	0.34	0.44	0.38	0.26	0.16	0.13	0.25	0.27	0.54	0.57	0.43
Na2O	3.23	3.15	3.52	3.26	3.61	3.04	3.32	4.24	4.88	3.55	4.94	4.94	3.85	3.09	3.93	4.33
K2O	0.39	0.42	0.18	0.38	0.52	0.34	0.47	0.73	1.23	1.05	3.26	3.32	5.33	2.79	3.29	4.45
P2O5	0.02	0.02	0.00	0.01	0.00	0.01	0.03	0.01	0.03	0.02	0.02	0.02	0.03	0.05	0.02	0.03
BeO*	7.66	9.00	9.33	9.20	6.88	8.60	8.00	0.80	0.06	0.24	0.50	0.69	0.00	2.01	1.50	0.00
Total	99.66	99.74	100.24	100.02	99.56	99.52	98.87	99.84	100.00	100.03	100.03	99.97	100.00	100.06	100.42	100.01
LOI	1.26	2.00	1.30	1.26	1.19	1.21	1.10	0.57	1.11	1.22	0.67	0.57	0.54	1.05	0.67	0.41
Li	568	442	291	476	374	419	333	199	-	663	209	332	-	333	562	43
F	2900	3200	2300	900	2200	1400	1900	1900	-	11000	2400	1900	-	2900	3300	-
Sc	195.0	140.1	137.5	176.0	45.5	161.0	160.7	21.0	9.7	6.5	9.4	13.4	3.1	18.6	15.4	3.1
V	10	13	11	13	14	12	12	8	20	15	9	8	13	16	9	10
Cr	-	-	3	-	3	-	-	-	1	1	2	-	-	3	-	1
Co	2	-	-	2	-	2	-	1	2	-	0	-	-	1	1	-
Ni	7	8	9	8	8	8	10	8	11	10	10	11	10	10	9	12
Cu	7	7	7	11	11	8	8	8	23	32	12	10	4	8	4	8
Zn	35	37	34	39	31	36	34	8	19	43	18	12	30	26	18	13
Ga	48	47	48	48	38	47	47	21	30	23	31	31	23	26	30	27
Rb	214	211	148	212	241	207	201	214	587	418	708	719	956	571	778	920
Sr	13	12	5	12	11	11	10	11	14	12	13	11	54	37	17	22
Y	198	157	69	48	32	82	113	74	79	28	30	48	48	90	88	75
Zr	91	113	98	116	30	86	90	92	119	110	109	98	206	153	139	115
Nb	111	100	81	96	130	88	97	147	144	160	119	112	97	98	122	119
Cs	190	-	-	157	-	189	-	24	16	-	16	-	-	52	40	-
Ba	56	45	47	54	34	46	46	33	34	30	39	36	219	90	51	59
La	73	49	41	42	13	51	62	42	47	23	31	27	45	63	41	21
Ce	166	173	122	76	85	100	157	104	101	93	55	94	141	115	80	65
Nd	57	48	31	26	85	33	49	29	31	16	17	21	46	35	29	24
Sm	11	-	-	5	-	6	-	5	6	-	2	-	-	6	5	-
Eu	0	-	-	1	-	1	-	0	0	-	0	-	-	0	0	-
Tb	2	-	-	-	-	2	-	1	1	-	1	-	-	1	1	-
Yb	25	-	-	6	-	11	-	10	10	-	4	-	-	10	10	-
Lu	4	-	-	1	-	2	-	2	2	-	1	-	-	2	2	-
Hf	12.0	-	-	15.0	-	11.0	-	7.6	8.0	-	7.8	-	-	7.0	12.0	-
Ta	55.0	-	-	42.0	-	40.0	-	64.0	40.0	-	38.0	-	-	21.0	31.0	-
W	29	-	-	32	-	25	-	79	68	-	44	-	-	24	39	-
Th	29	-	-	26	-	24	-	33	41	-	31	-	-	63	49	-
U	7.3	-	-	12.2	-	5.0	-	11.0	8.3	-	12.4	-	-	8.1	11.4	-

R=rosettes, M=granitic host, I=group I granite sample, and D=granite containing disseminated beryl.
INAA values reported for La, Nd, and Sc, where available, otherwise XRF value reported.

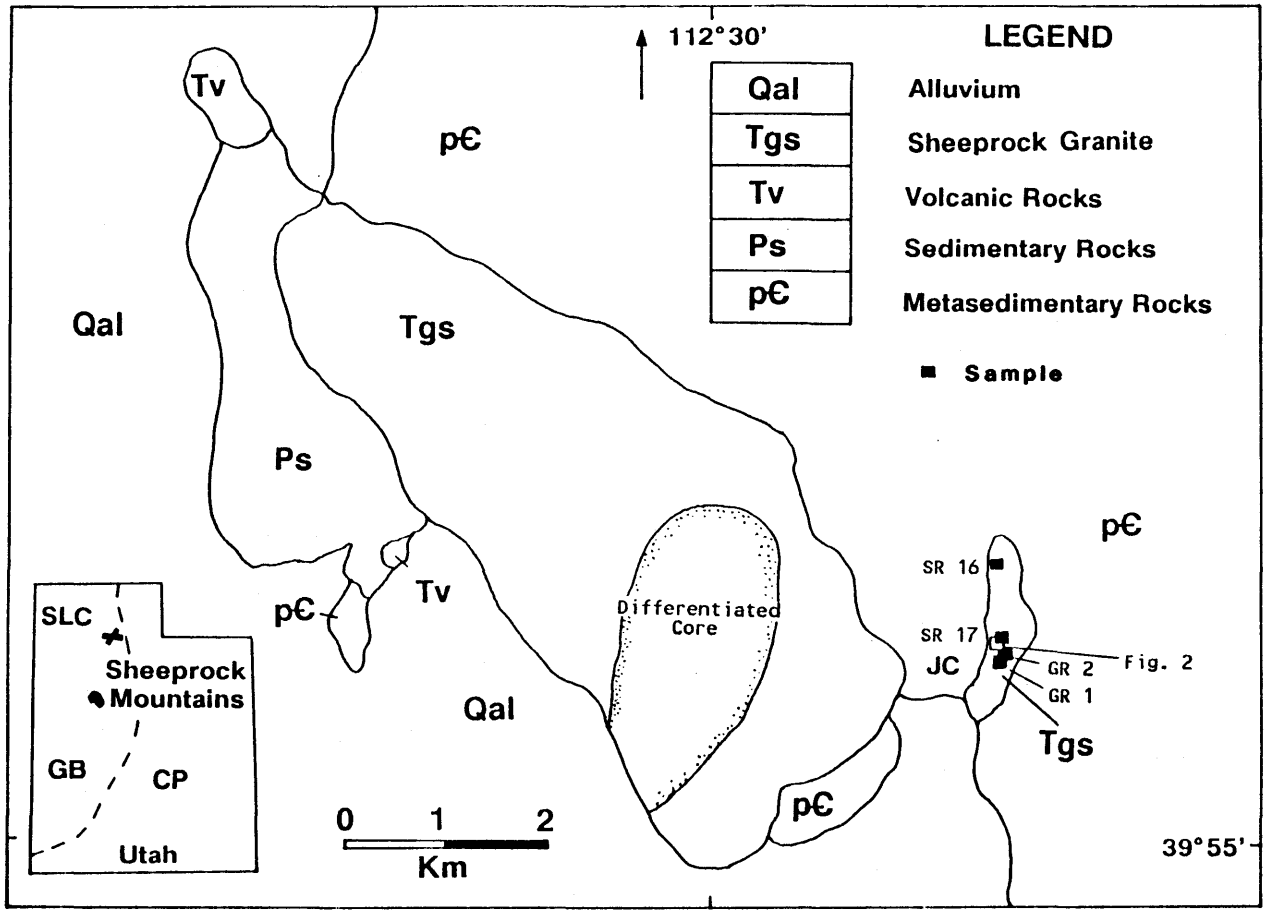
112°30'
LEGEND
Qal
Alluvium
Tgs
Sheeprock Granite
Tv
Volcanic Rocks
Ps
Sedimentary Rocks
pC
Metasedimentary Rocks
Sample
Tv
pC
Qal
Tgs
Ps
pC
Tv
Qal
Differentiated Core
pC
SR 16
SR 17
JC
GR 2
GR 1
Fig. 2
Tgs
pC
SLC
Sheeprock Mountains
GB
CP
Utah
0 1 2
Km
39°55'

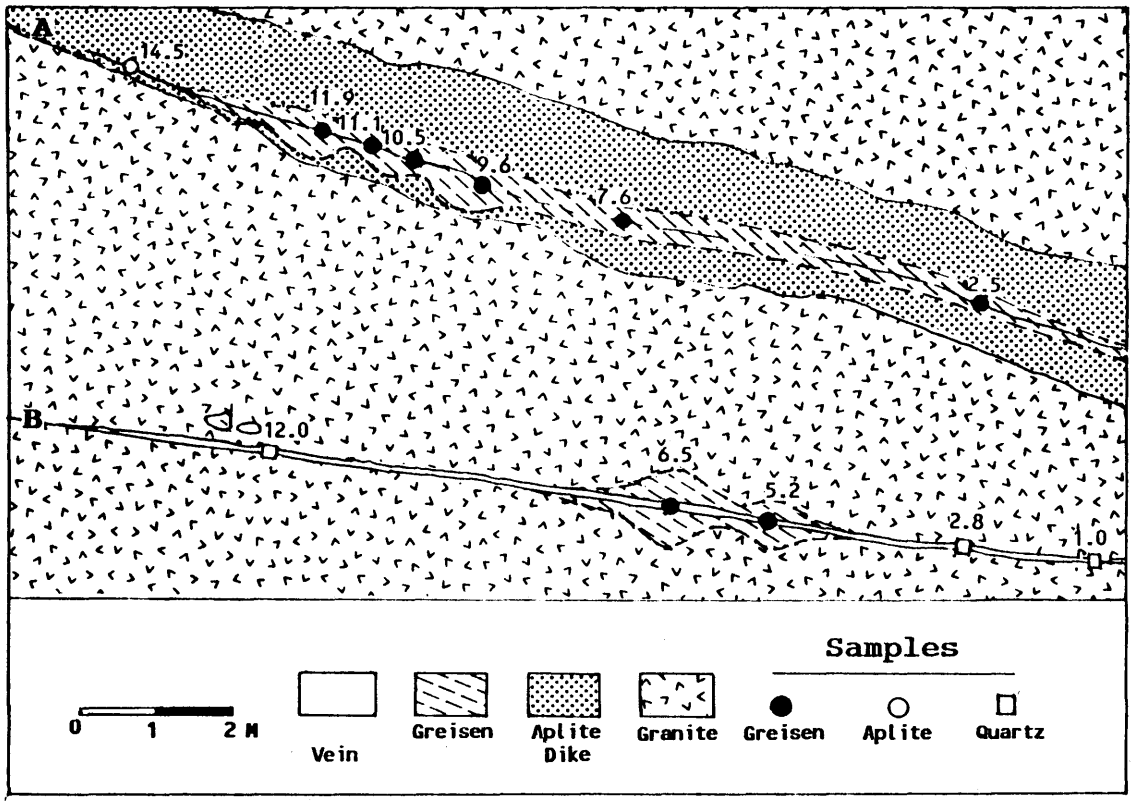
A
14.5
11.9
11.1
10.5
9.6
7.6
2.5
B
12.0
6.5
5.2
2.8
1.0
Samples
0 1 2 M
Vein
Greisen
Aplite Dike
Granite
Greisen
Aplite
Quartz

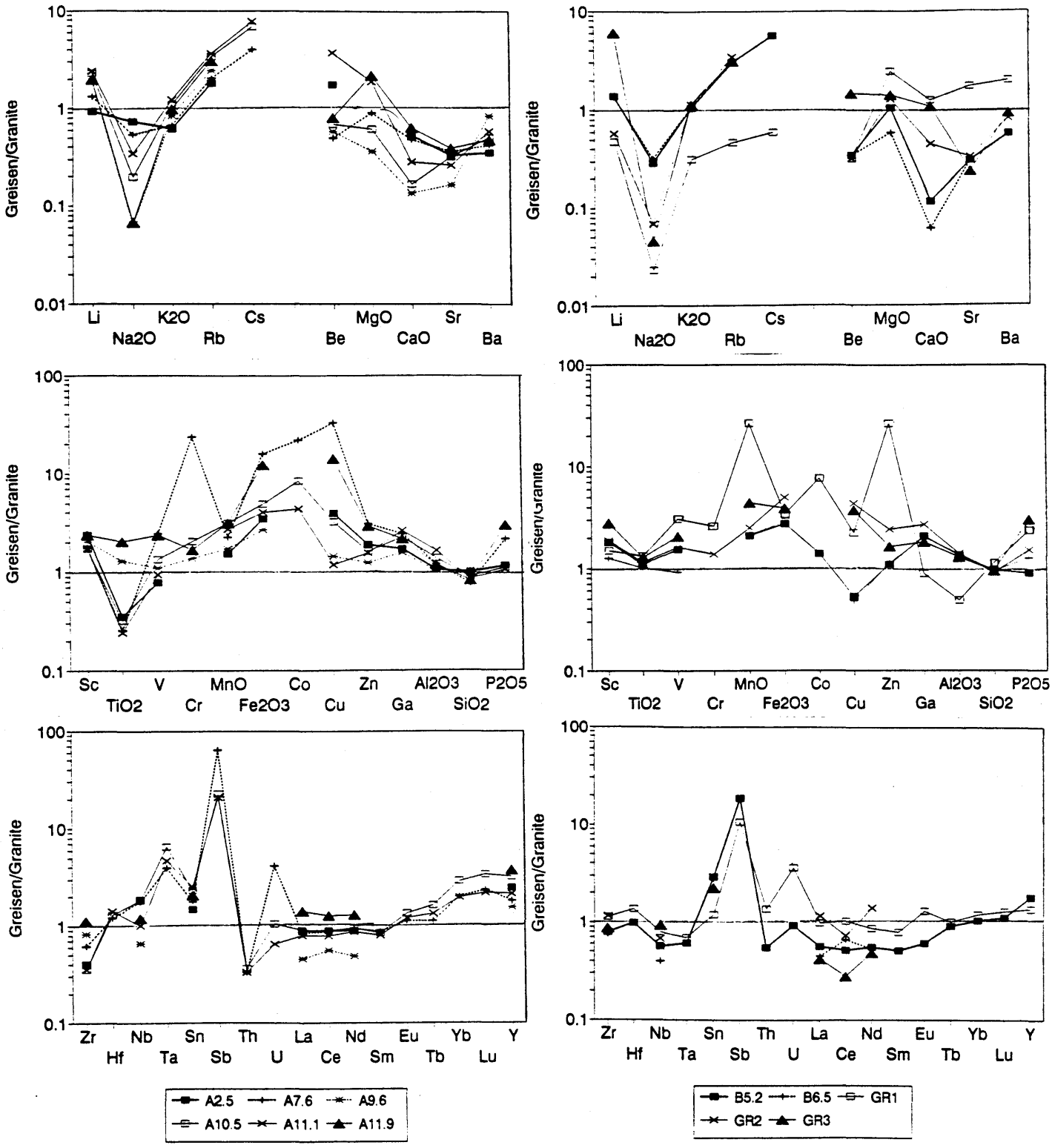
Greisen/Granite
10
1
0.1
0.01
Li
K2O
Cs
MgO
Sr
Na2O
Rb
Be
CaO
Ba
100
Sc
V
MnO
Co
Zn
Al2O3
P2O5
TiO2
Cr
Fe2O3
Cu
Ga
SiO2
Zr
Nb
Sn
Th
La
Nd
Eu
Yb
Y
Hf
Ta
Sb
U
Ce
Sm
Tb
Lu
A2.5
A7.6
A9.6
A10.5
A11.1
A11.9
B5.2
B6.5
GR1
GR2
GR3

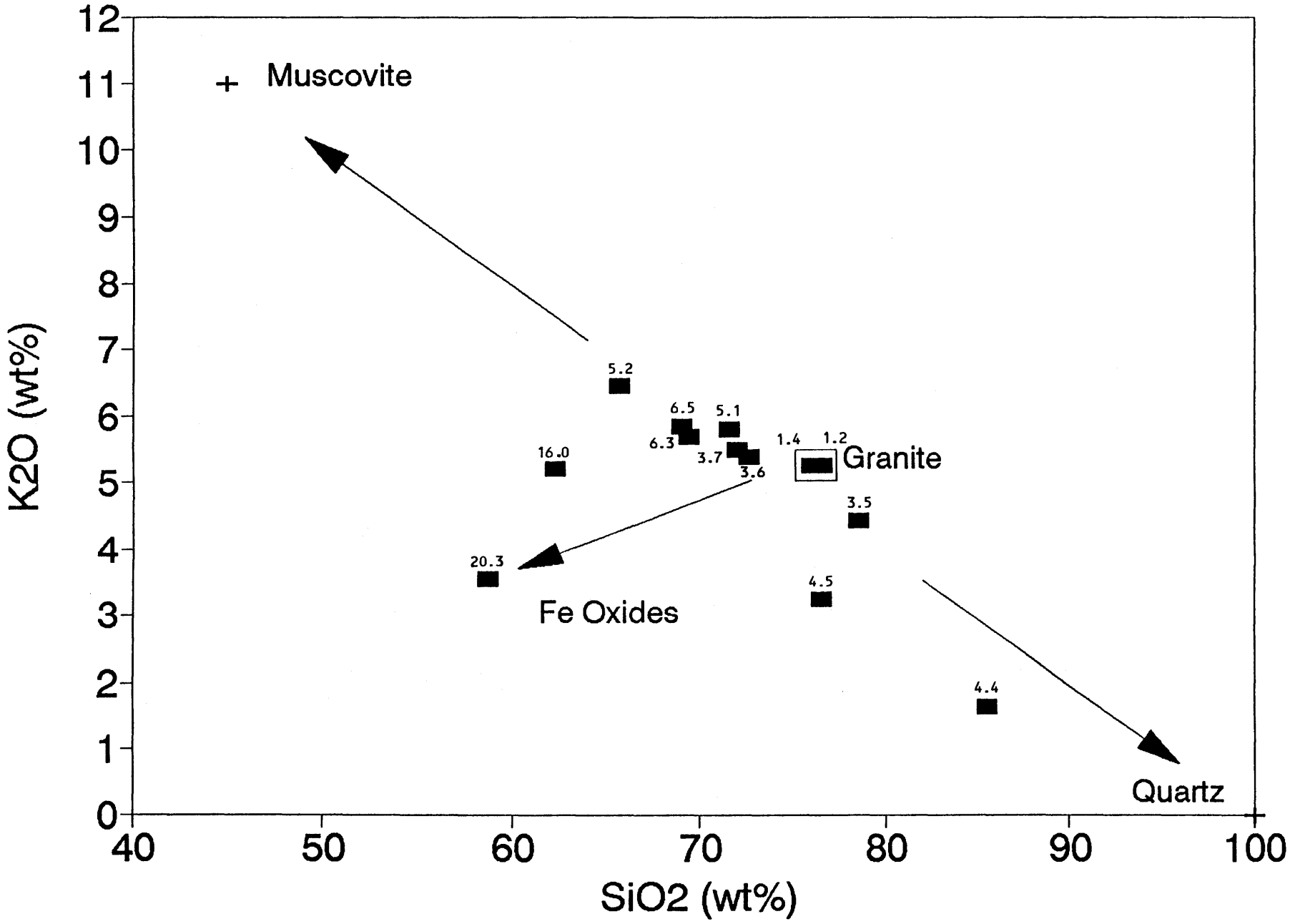
Muscovite
Granite
Fe Oxides
Quartz
5.2
6.5
5.1
6.3
1.4
1.2
16.0
3.7
3.6
3.5
20.3
4.5
4.4
K2O (wt%)
SiO2 (wt%)
0
1
2
3
4
5
6
7
8
9
10
11
12
40
50
60
70
80
90
100

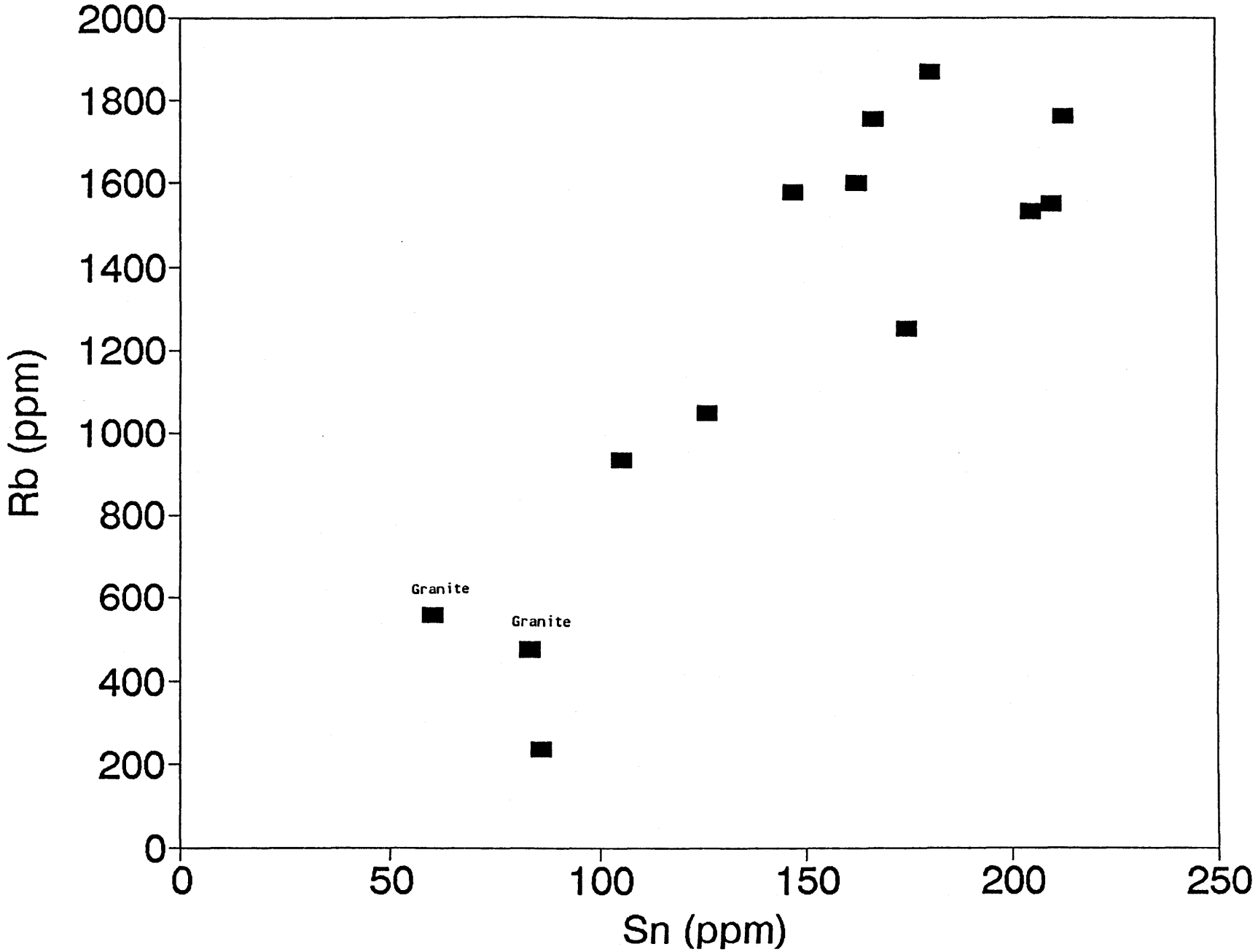
2000
1800
1600
1400
1200
1000
800
600
400
200
0
Rb (ppm)
0
50
100
150
200
250
Sn (ppm)
Granite
Granite

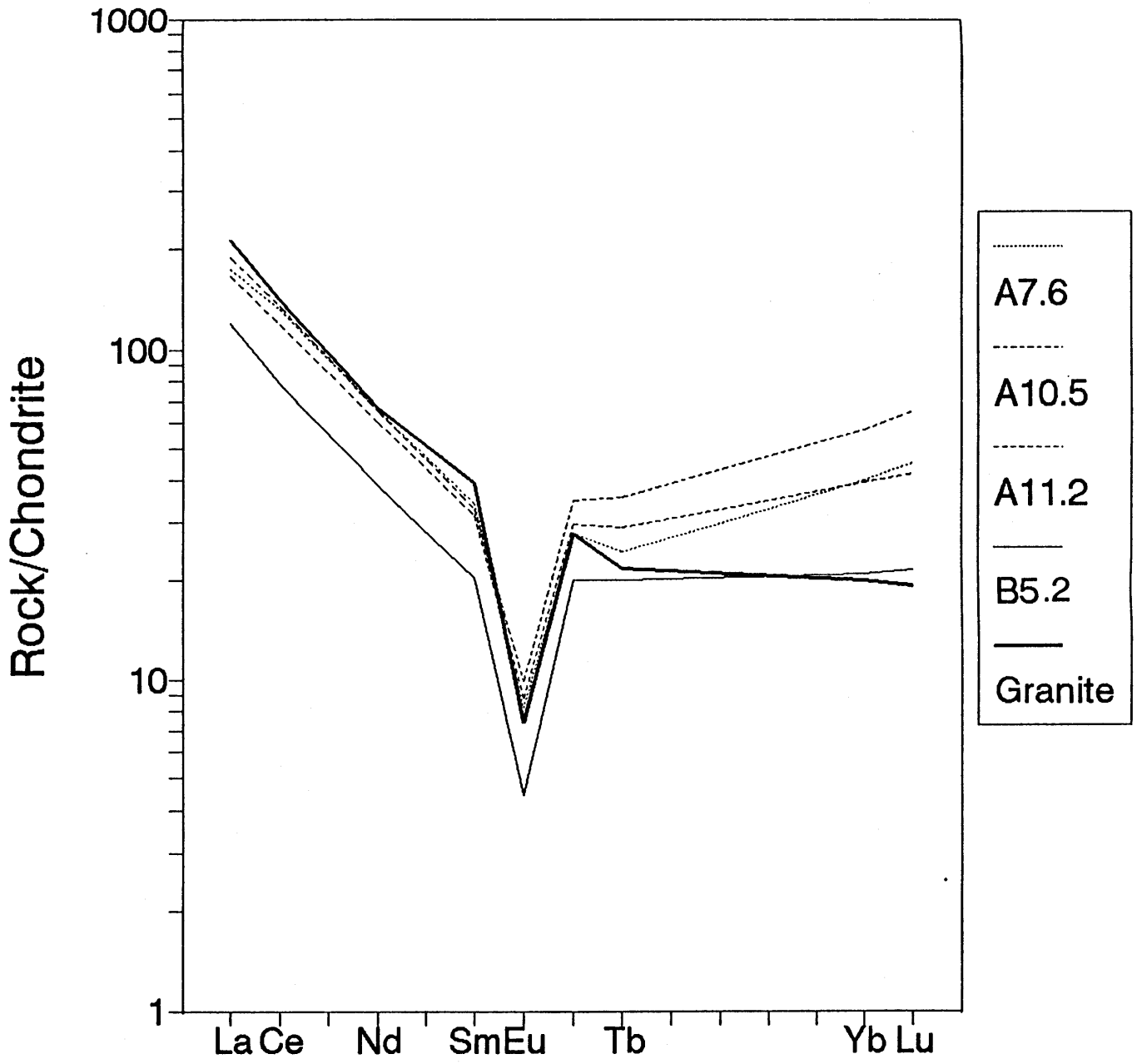
1000
100
10
1
Rock/Chondrite
La
Ce
Nd
Sm
Eu
Tb
Yb
Lu
A7.6
A10.5
A11.2
B5.2
Granite

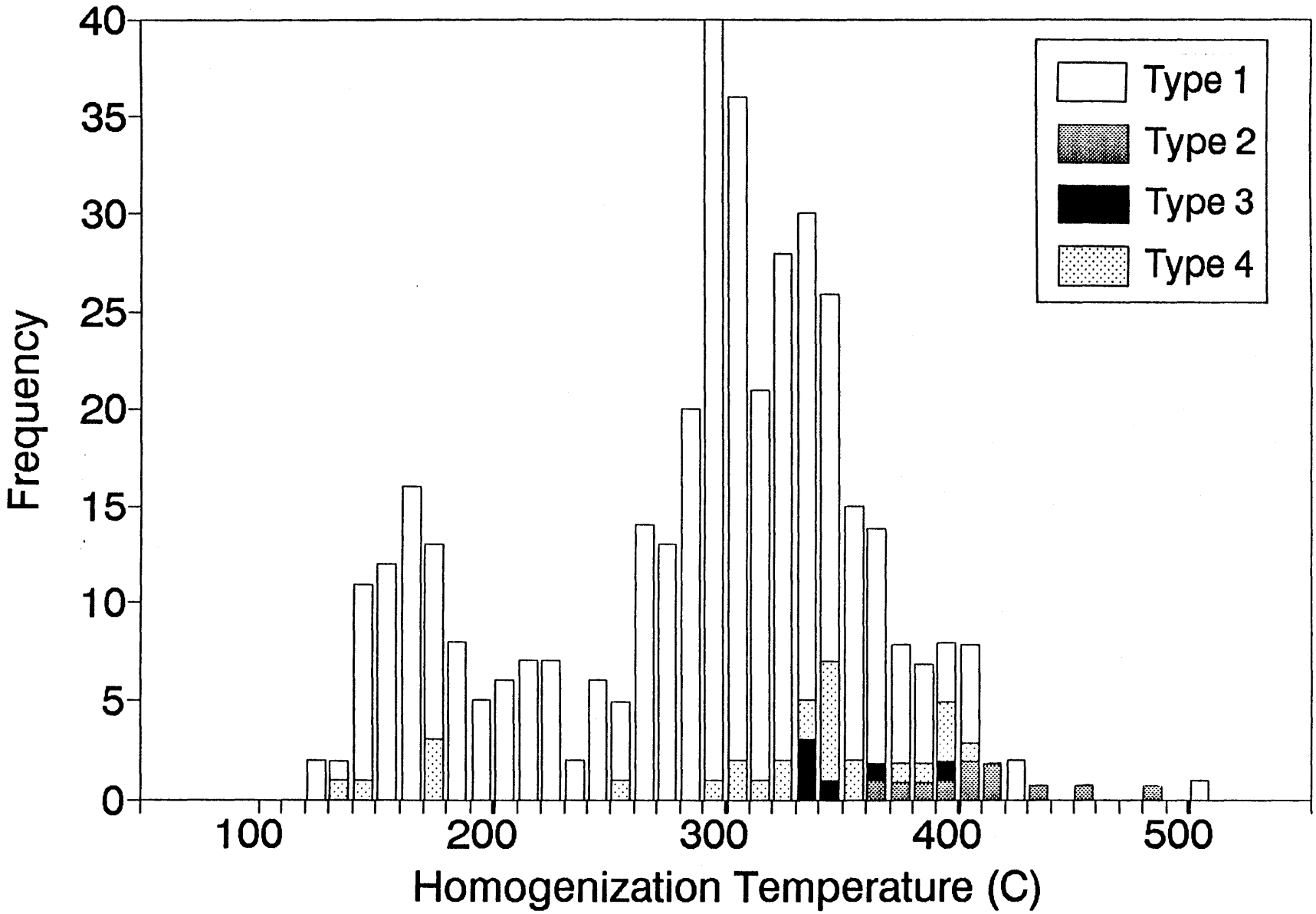
Type 1
Type 2
Type 3
Type 4
Frequency
0
5
10
15
20
25
30
35
40
100
200
300
400
500
Homogenization Temperature (C)

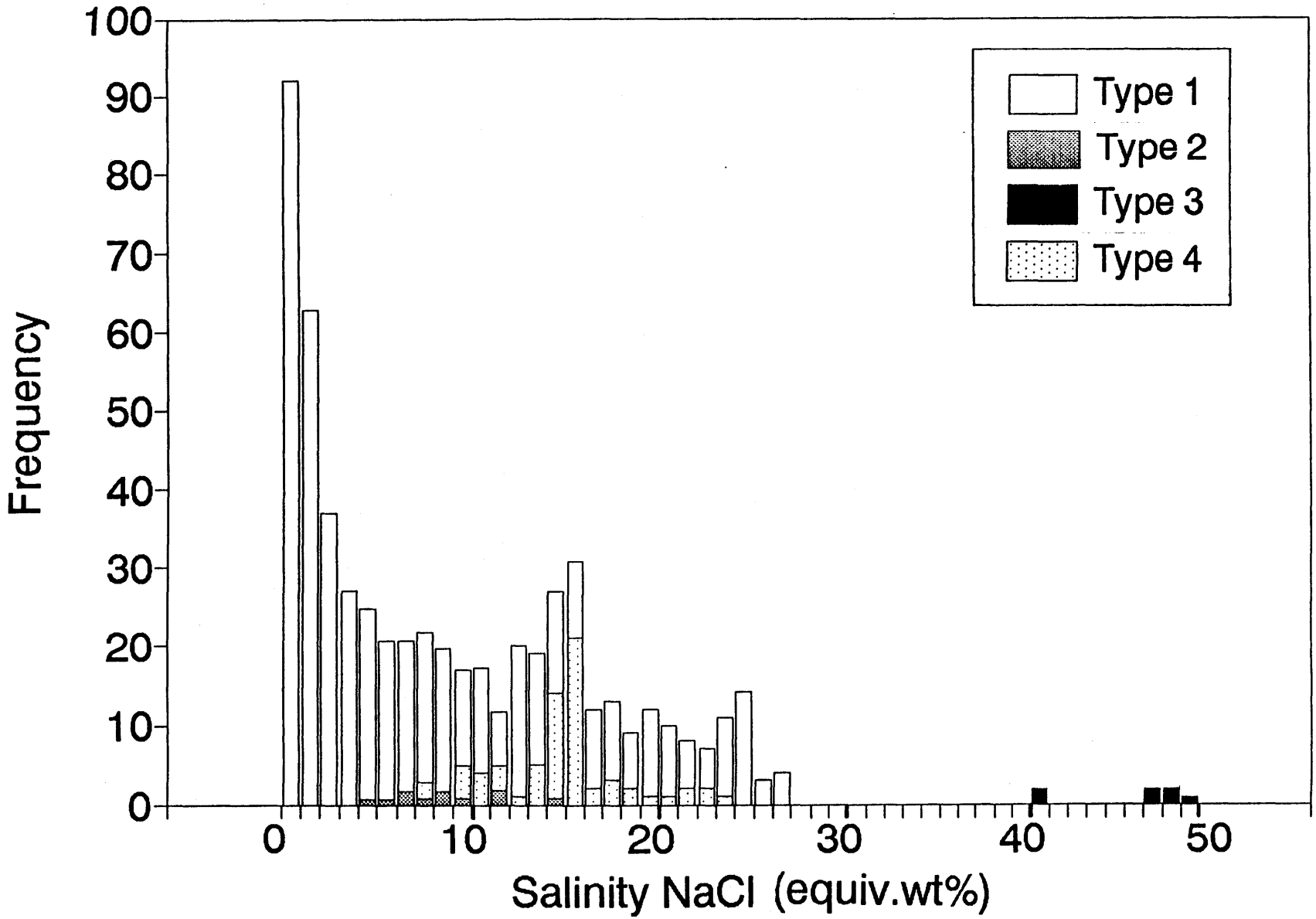
Type 1
Type 2
Type 3
Type 4
Frequency
100
90
80
70
60
50
40
30
20
10
0
0
10
20
30
40
50
Salinity NaCl (equiv.wt%)

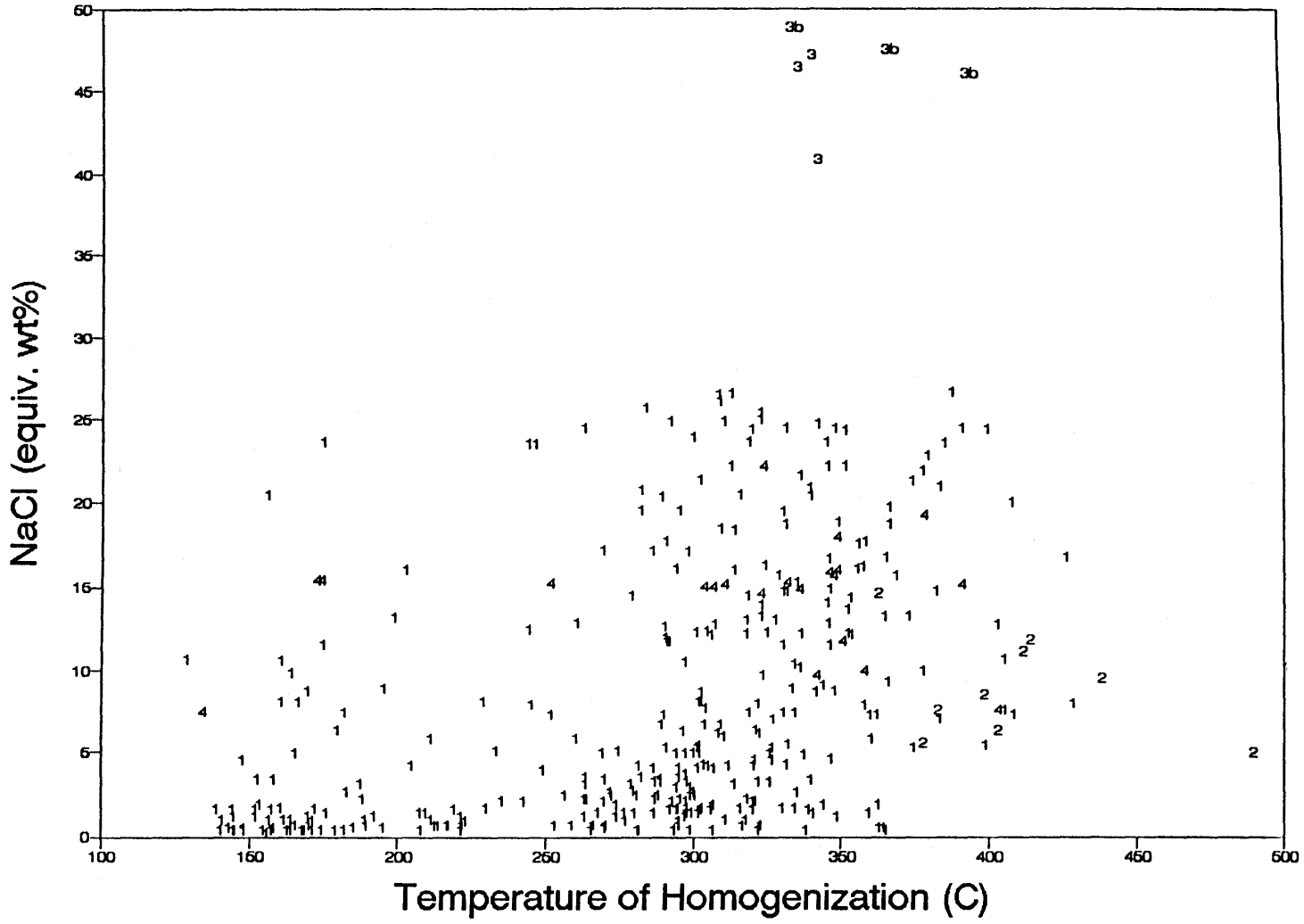
NaCl (equiv. wt%)
Temperature of Homogenization (C)
0
5
10
15
20
25
30
35
40
45
50
100
150
200
250
300
350
400
450
500

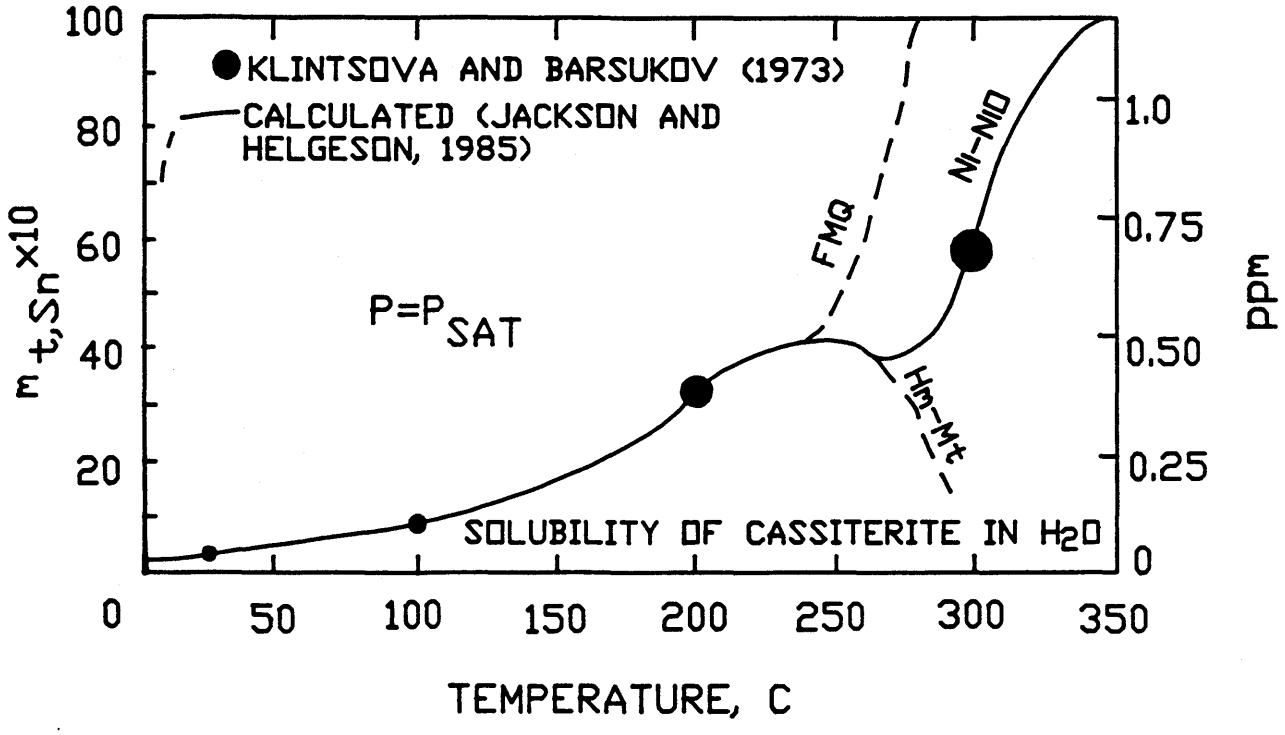
KLINTSOVA AND BARSUKOV (1973)
CALCULATED (JACKSON AND HELGESON, 1985)
P=P SAT
FMQ
Ni-NiO
Hm-Mt
SOLUBILITY OF CASSITERITE IN H2O
m t,Sn x10
ppm
TEMPERATURE, C
0
20
40
60
80
100
0.25
0.50
0.75
1.0
50
150
200
250
300
350

TABLE 1. WHOLE-ROCK CHEMICAL ANALYSES OF GREISENS AND GRANITES FROM THE SHEEPROCK GRANITE

Sample No.	A2.5	A7.6	A9.6	A10.5	A11.1	A11.9	B5.2	B6.5	GR1	GR2	GR3	SR16	SR17
							Weight Percent						
SiO2	76.5	58.8	78.5	69.4	65.7	62.3	72.7	72.1	85.6	69.0	71.7	76.6	76.0
TiO2	0.07	0.05	0.24	0.06	0.05	0.38	0.20	0.19	0.24	0.21	0.24	0.17	0.20
Al2O3	13.3	15.2	12.9	17.6	20.9	15.0	16.9	17.3	6.1	17.6	16.2	12.6	12.6
Fe2O3	4.49	20.33	3.48	6.30	5.22	15.96	3.57	3.71	4.43	6.49	5.07	1.21	1.36
MnO	0.05	0.07	0.05	0.10	0.08	0.10	0.06	0.06	0.80	0.08	0.13	0.03	0.03
MgO	0.00	0.20	0.08	0.14	0.42	0.48	0.23	0.13	0.53	0.28	0.31	0.20	0.24
CaO	0.22	0.20	0.06	0.07	0.12	0.27	0.05	0.03	0.52	0.18	0.45	0.26	0.58
Na2O	2.24	1.63	0.20	0.61	1.05	0.21	0.88	0.97	0.07	0.21	0.14	3.10	3.01
K2O	3.24	3.54	4.45	5.70	6.43	5.21	5.39	5.51	1.64	5.85	5.79	5.26	5.26
P2O5	0.02	0.04	0.02	0.02	0.02	0.06	0.02	0.03	0.05	0.03	0.06	0.02	0.02
Total	100.58	99.93	100.47	100.68	101.24	102.28	100.33	100.48	101.02	101.01	101.49	99.45	99.33
LOI	1.82	3.50	2.03	2.73	3.06	3.18	2.37	2.32	1.57	2.73	2.43	0.69	0.79
							Parts Per Million						
Li	135	194	275	333	348	288	201	196	69	84	882	187	104
Rb	931	1047	1250	1754	1870	1578	1548	1533	236	1761	1597	555	476
Cs		43.4		74.1	84.2		61.3		6.3			13	6.8
Be	63	18	21	25	134	29	12	12	11	11	51	25	47
Sr	21	22	10	20	16	24	18	18	105	20	14	53	69
Ba	67	79	160	96	110	90	104	102	361	148	169	165	209
Sc	5	4	4	4	4	5	4	3	3	4	6	2	2
V	10	32	14	17	12	31	20	12	40	21	27	11	15
Cr	0	31	2	3	0	2	0	0	3	2	0	0	3
Co		22		8.5	4.4		1.4		7.8			0.91	1.1
Ni	10	0	12	10	8	3	9	12	7	9	7	7	7
Cu	33	272	12	27	10	118	4	4	19	36	31	6	10
Zn	57	95	38	49	47	90	33	34	810	74	50	31	30
Ga	36	52	34	48	56	47	45	44	19	58	39	21	21
As		78		10	3		1		17				
Sb		8.9		3.2	2.9		2.6		1.5			0.17	0.11
Br		5.6		3	3.6		3.8		4.4				
Y	104	78	66	136	90	160	76	78	58	91	58	41	44
Zr	67	103	138	60	60	186	132	127	190	193	146	157	177
Hf		7.8		8.4	9.3		6.4		8.9			6.71	6.31
Nb	107	102	38	105	58	69	33	23	46	39	54	59	56
Ta		43		71	51		6.7		7.6			11.2	10.5
Sn	105	126	174	166	180	147	210	205	86	213	162	60	83
W		140		140			22		15				
La	58	55.1	30	59.9	52.7	94	37.9	30	66.6	78	28	70.5	62.9
Ce	109	108	69	110	97	156.9	64	81.5	126	90	34	127	118
Nd	37	39	20	39	36	54	23	22	36	58	20	40.7	41.5
Sm		6.53		6.34	6.01		3.89		6.04			7.62	7.45
Eu		0.59		0.71	0.63		0.32		0.69			0.46	0.59
Tb		1.1		1.6	1.3		0.9		1			0.93	1.03
Yb		8.37		12	8.23		4.35		4.98			3.99	4.3
Lu		1.44		2.08	1.34		0.69		0.8			0.6	0.63
Th		24		26	24		40		100			73.6	71.3
U		32.3		8.1	5		7.3		28.5			6.48	9.05